



LIQUID CRYSTALLINE POLYMERS FOR SMART APPLICATIONS.

Krzysztof Artur Bogdanowicz

Dipòsit Legal: T 1677-2015

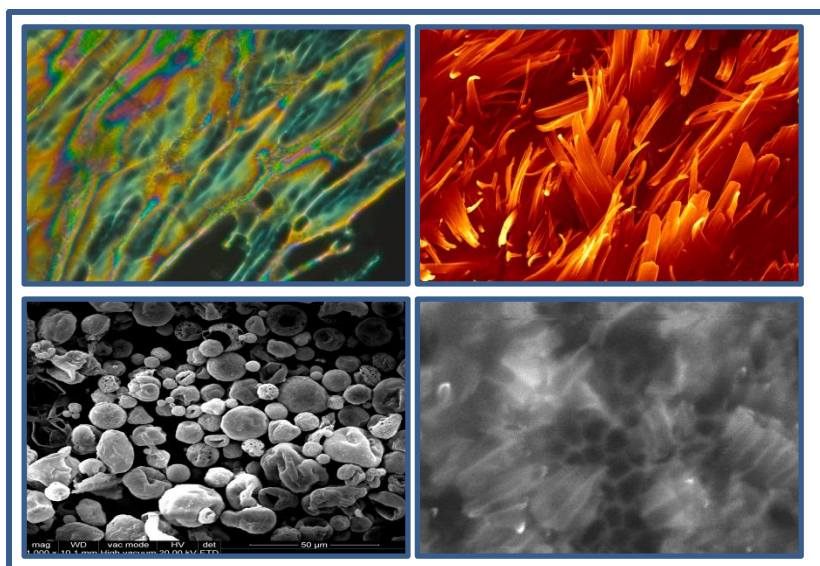
ADVERTIMENT. L'accés als continguts d'aquesta tesi doctoral i la seva utilització ha de respectar els drets de la persona autora. Pot ser utilitzada per a consulta o estudi personal, així com en activitats o materials d'investigació i docència en els termes establerts a l'art. 32 del Text Refós de la Llei de Propietat Intel·lectual (RDL 1/1996). Per altres utilitzacions es requereix l'autorització prèvia i expressa de la persona autora. En qualsevol cas, en la utilització dels seus continguts caldrà indicar de forma clara el nom i cognoms de la persona autora i el títol de la tesi doctoral. No s'autoritza la seva reproducció o altres formes d'explotació efectuades amb finalitats de lucre ni la seva comunicació pública des d'un lloc aliè al servei TDX. Tampoc s'autoritza la presentació del seu contingut en una finestra o marc aliè a TDX (framing). Aquesta reserva de drets afecta tant als continguts de la tesi com als seus resums i índexs.

ADVERTENCIA. El acceso a los contenidos de esta tesis doctoral y su utilización debe respetar los derechos de la persona autora. Puede ser utilizada para consulta o estudio personal, así como en actividades o materiales de investigación y docencia en los términos establecidos en el art. 32 del Texto Refundido de la Ley de Propiedad Intelectual (RDL 1/1996). Para otros usos se requiere la autorización previa y expresa de la persona autora. En cualquier caso, en la utilización de sus contenidos se deberá indicar de forma clara el nombre y apellidos de la persona autora y el título de la tesis doctoral. No se autoriza su reproducción u otras formas de explotación efectuadas con fines lucrativos ni su comunicación pública desde un sitio ajeno al servicio TDR. Tampoco se autoriza la presentación de su contenido en una ventana o marco ajeno a TDR (framing). Esta reserva de derechos afecta tanto al contenido de la tesis como a sus resúmenes e índices.

WARNING. Access to the contents of this doctoral thesis and its use must respect the rights of the author. It can be used for reference or private study, as well as research and learning activities or materials in the terms established by the 32nd article of the Spanish Consolidated Copyright Act (RDL 1/1996). Express and previous authorization of the author is required for any other uses. In any case, when using its content, full name of the author and title of the thesis must be clearly indicated. Reproduction or other forms of for profit use or public communication from outside TDX service is not allowed. Presentation of its content in a window or frame external to TDX (framing) is not authorized either. These rights affect both the content of the thesis and its abstracts and indexes.

Liquid Crystalline Polymers for Smart Applications

Krzysztof Artur Bogdanowicz



UNIVERSITAT
ROVIRA I VIRGILI

2015

Department of Chemical Engineering

Liquid Crystalline Polymers for Smart Applications

By

Krzysztof Artur Bogdanowicz

Doctoral Thesis

Supervisors:

Dr. Marta Giamberini

Dr. José Antonio Reina



UNIVERSITAT ROVIRA I VIRGILI

Tarragona

2015

UNIVERSITAT ROVIRA I VIRGILI
LIQUID CRYSTALLINE POLYMERS FOR SMART APPLICATIONS.
Krzysztof Artur Bogdanowicz
Dipòsit Legal: T 1677-2015



Department d'Enginyeria Química

Campus Sescelades,
Avda. Països Catalans, 26
43007 Tarragona
Tel: 977 55 97 87
Fax: 977 55 96 21

Marta Giamberini, Associate Professor at the University Rovira i Virgili,
Department of Chemical Engineering and José Antonio Reina Lozano,
Associate Professor at the University Rovira i Virgili, Department of
Analytical Chemistry and Organic Chemistry,

We state that the present study, entitled "Liquid Crystalline Polymers for
Smart Applications", presented by Krzysztof Artur Bogdanowicz for the
award of the degree of Doctor, has been carried out under our supervision
at the Chemical Engineering Department at the University Rovira i Virgili,
and that it fulfils all the requirements to be eligible for the Doctor European
Mention.

Tarragona, 01 September 2015

Supervisor of the doctoral thesis

Co-supervisor of the doctoral thesis

Dra. Marta Giamberini

Dr. José Antonio Reina Lozano

UNIVERSITAT ROVIRA I VIRGILI
LIQUID CRYSTALLINE POLYMERS FOR SMART APPLICATIONS.
Krzysztof Artur Bogdanowicz
Dipòsit Legal: T 1677-2015

Acknowledgments

Firstly, I would like to express my deepest sincere gratitude to my incredible advisers Professor Marta Giamberini and Professor José Antonio Reina for the opportunity to join the doctoral programme under their supervision, for the continuous support of my Ph. D study and related research, for their patience, motivation, and immense knowledge. Their guidance helped me in all the time of research and writing of this thesis. I could not have imagined having better and friendlier advisers and mentors for my Ph. D study.

Besides my advisers, I would like to thank all professors of Chemical Engineering Department of Organic Chemistry and Chemical Engineering for their help and word of advice. I am also thankful to technicians of Department of Chemical Engineering (Ana, Josep Maria and Àngel) and Organic Chemistry (Juan Luis and Tere,) and both departmental secretaries. As well, I would like to thank Núria Juanpere, Dolors Màrmol and Merche Maurín for their help in all the administrative issues.

My sincere thanks also goes to all technicians of Servei de Recursos Científics i Tècnics for kindly helping me in my sample analysis, especially Francesc Gispert, Ramón Guerrero, Ernest Arce, Mariana Stefanova, Mercè Moncusí and Rita Marimon.

I am very grateful to Dr. Philippe Sístat for his incredible help and valuable advices during my research stay in IEMM in Montpellier. I would like to thank all the kind people, whom I met in France: Zlatina, Anthony and Mathilde for making my stay pleasant.

I would like to give special thanks to Dr. Nuno A. G. Bandeira, Dr. Alben Lederer and Dr. Veronica Ambroggi for successful collaboration, which has resulted in jointly published articles.

I would like to thank METEOR group, full of extraordinary and smart people. Thank you for your help: Dr. Ricard Garcia Valls, Dr. Tània Gumí, Dr. Bartosz Tyllkowski, Josefa Lázaro, Xavier, Kamila, Adrianna, Cristina Quintas, Rubén, Claude Garcia, Cinta, Diana, Brisa, Hany, Asta, Surya and Albert.

My special appreciation goes to an incredible person Prof. Àngels Serra for her knowledge, hospitality, kindness and interesting conversations.

My stay in Tarragona would not be so fantastic without special people I met on my way. I could never imagine that I would find such a special group of friends. Bartek, you were the first person I met when I arrived first time to Spain. You showed me your kindness and you helped me many times. You are a good person and a good friend.

The Pepa's office was a special place of gathering during mornings and afternoons coffee, where with Pepa, Montse, Tamara, Ana, Esther, Martín, Magda and Susana we shared wonderful time full of interesting conversations and funny moments.

I would not manage anything without irreplaceable Josefa (Pepa); you have helped me with so many administrative things and orders, I could even count. Thank you for never refusing to help me.

I grateful for Xavier, Cristina Acebo, Dailyn, Asta and Surya, my fellow labmates in Organic Chemistry Department, for the stimulating discussions, for the long hours we were working together before deadlines, and for all the fun we have had in the last four years.

Kamila, Ada and Cristina Quintas, thank you for discussions not only about science, but also for sharing ideas, your suggestions and for home-like atmosphere in the laboratory.

My special appreciation goes to my flatmate Martín. Thank you for your support, help in learning Spanish language, advices and for being a great friend, who I could always count on.

Of course, I could not forget to mention you Valentina. From the first moment we met, we became a very close friends. Thank you my Bro for all lovely moments and your friendship.

I would like to thank to student, which worked with me: Anna Trojanowska, Katarzyna Glińska, Griffin Anthony Rapsilber and Nicholas Romanov. You were these people, who gave me an important lesson- how to share my knowledge and how to be a tutor. Each one of you was different and special for me. Thank you for that!

Next, I would like to thank my Master supervisor from Poland, Prof. Violetta Partoniak, who helped me, support me, encourage me to creative thinking and was a catalyst, helping to start my incredible journey.

Thank you does not seem enough for all what we went through together. I would like to thank to Monika Waleśa, Marta Maćkowiak, and many other friends from Faculty of Chemistry in Poland for their support, encouragement, care, understanding and precious friendship.

A special thanks goes to my incredible family. I am truly thankful to my parents and my brothers for support, understanding, help and love. My family encouraged me to follow my heart and my mind in achieving goals I set for me. This would not be possible without my lovely family. I love you!

Finally, financial support from Ministerio de Economía y Competitividad (CTQ2013-46825-R) and the PhD scholarship from Univrsitat Rovira i Virgili are gratefully acknowledged.

Thank you all for your advices, guidance and support!

Krzysztof Artur Bogdanowicz

To people I love

UNIVERSITAT ROVIRA I VIRGILI
LIQUID CRYSTALLINE POLYMERS FOR SMART APPLICATIONS.
Krzysztof Artur Bogdanowicz
Dipòsit Legal: T 1677-2015

Imagination is more important than knowledge.
Knowledge is limited. Imagination encircles the world.

Dr. Albert Einstein

UNIVERSITAT ROVIRA I VIRGILI
LIQUID CRYSTALLINE POLYMERS FOR SMART APPLICATIONS.
Krzysztof Artur Bogdanowicz
Dipòsit Legal: T 1677-2015

LIST OF ABBREVIATIONS

1,2-DCE	1,2-dichloroethane
^1H, ^{13}C NMR	proton and carbon nuclear magnetic resonance
AAO	anodized aluminium oxide
AFM	atomic force microscope
CA	contact angle
DMFC	direct methanol fuel cell
DNA	deoxyribonucleic acid
DP	polymerization degree
DSC	differential scanning calorimetry
ESEM	environmental scanning electron microscope
FC	fuel cell
FTIR	Fourier transform infrared spectroscopy
HSQC	heteronuclear single quantum coherence
LCP	liquid-crystalline polymer
LS	light scattering
MCLCP	main-chain liquid crystalline polymers
P(ECH-co-EO)]	poly(epichlorohydrin-co-ethylene oxide)
PAZE	poly[1-(2-hydroxyethyl)aziridine]
PECH	poly(epichlorohydrin)
PEM	polymer electrolyte membrane
PEMFC	polymer electrolyte membrane fuel cell
PESA	perfluorosulfonic acid membranes
PIP	phase inversion precipitation
POM	polarized optical microscopy
PTFE	polytetrafluoroethylene
RNA	ribonucleic acid
RT	room temperature
SCLCP	side-chain liquid-crystalline polymers

SEC	size exclusion chromatography
SEC-MALLS	size exclusion chromatography coupled to a multi-angle laser light-scattering detector
SEM	scanning electron microscope
T_c	crystallization temperature
T_g	glass transition temperatures
TGA	thermogravimetric analysis
THF	tetrahydrofuran
TLC	thin layer chromatography
T_m	melting temperature
TMV	tobacco mosaic virus
XRD	X-ray diffraction

TABLE OF CONTENTS

General Introduction and Objectives	1
"Smart" Materials	3
Liquid Crystals	3
Calamitic Molecules	7
Discotic Molecules	8
Liquid Crystalline Polymers	9
Strategy for smart materials	10
Objectives	11
References	12
Part 1. Application of Calamitic Liquid Crystalline Polymers	15
Microcapsules	17
Controlled Release	19
References	21
Chapter 1. Synthesis and Characterisation of a New Family of Photoactive Liquid Crystalline Polyesters based on α-methylstilbene	23
1.1.1. Introduction	25
1.1.2. Materials and Methods	27
Materials	27
Polymer Preparation	27
Characterisation	29
1.1.3. Results and Discussion	31
Polymer Synthesis and Characterisation	31
Mesomorphic and Thermal Characterisation	38
Polymer Photoisomerization	42
1.1.4. Conclusions	47
1.1.5. Acknowledgements	48
1.1.6. Supporting Information	48

1.1.7. References	53
Chapter 2. Preparation and Characterisation of Light-Sensitive Microcapsules based on a Liquid Crystalline Polyester	55
1.2.1. Introduction	57
1.2.2. Experimental Section	58
Materials	58
Membrane Preparation	59
Microcapsules Preparation	59
Characterisation	60
1.2.3. Results and Discussion	62
Membrane Preparation and Characterisation	62
Microcapsules Characterisation	66
1.2.4. Conclusions	71
1.2.5. Acknowledgements	72
1.2.6. Supporting Information	72
1.2.7. References	74
Chapter 3. An Atomistic Insight into Light-sensitive Polymers with Methylstilbene Building Blocks	77
1.3.1. Introduction	79
1.3.2. Computational Details	81
1.3.3. Results and Discussion	82
1.3.4. Conclusions	90
1.3.5. Acknowledgements	91
1.3.6. Supporting Information	92
1.3.7. References	93
Part 2. Application of Calamitic Liquid Crystalline Polymers	97
Proton Exchange Membranes	99
Proton Transport	102
References	105

Chapter 4. Applying Nature's Genius to Discotic Liquid-crystal Polymers for Proton Conducting Membrane	107
2.4.1. Introduction	109
2.4.2. Materials and Methods	111
Materials	111
Membrane preparation	112
Characterisation	113
2.4.3. Results and Discussion	117
Membrane Preparation, Characterisation and Permeability	117
Membrane Conductivity	124
2.4.4. Conclusions	126
2.4.5. Acknowledgements	126
2.4.6. Supporting Information	127
1.3.7. References	129
Chapter 5. Liquid Crystalline Polymeric Wires for selective Proton Transport, Part 1: Wires Preparation	131
2.5.1. Introduction	133
2.5.2. Materials and Methods	134
Materials	134
Synthesis of Polymer	134
Characterisation Methods	135
Membrane Preparation	138
Thermal Treatment (baking process)	138
2.5.3. Results and Discussion	138
2.5.4. Conclusions	147
2.5.5. Acknowledgements	147
2.5.6. Supporting Information	148
2.5.7. References	149

Chapter 6. Liquid Crystalline Polymeric Wires for Selective Proton Transport, Part 2: Ion Transport in Solid-state	151
2.6.1. Introduction	153
2.6.2. Materials and Methods	155
Materials	155
Membrane preparation	155
Thermal Treatment (baking process)	155
Characterisation	156
2.6.3. Results and Discussion	159
Conductivity measurements by EIS	159
Ion transport in aqueous solution	164
Methanol Cross-over	168
2.6.4. Conclusions	168
2.6.5. Acknowledgements	169
2.6.6. Supporting Information	169
2.6.7. References	170
General Conclusions	173
Appendixes	177
Appendix A. List of Figures, Tables and Schemes	179
Appendix B. List of publications	185
Appendix C. Congress and contributions	186

General introduction and Objectives

UNIVERSITAT ROVIRA I VIRGILI
LIQUID CRYSTALLINE POLYMERS FOR SMART APPLICATIONS.
Krzysztof Artur Bogdanowicz
Dipòsit Legal: T 1677-2015

General Introduction and Objectives

"Smart" Materials

One of the first reports on the smart materials was published in 1800s, reporting on the phenomena of magnetostrictive. Over a time, the term "smart" have been extending its own meaning and nowadays describes materials with the ability to change physico-chemical appearance, properties and structure under certain impulses in a predictable manner. However, this definition still can apply to a numerous disciplines, having slightly different meaning, depending on the specification of the field¹.

For purpose of this dissertation, the term "smart materials" will be use in context of polymeric compounds with moderated capacity to rearrange their structure under internal or external stimuli. The main objective of this work is to present intelligent materials based on novel liquid crystalline polymers to embark on a new approach of material design, synthesis and system integration.

Liquid Crystals

In the material world different physical states, in which the matter exhibits can be observed. The classification of these states can be based on arrangement of molecules and physical properties, for instance: mechanical, optical, magnetic and electric. In general, three major states: gas, isotropic liquid and three-dimensional solid, can be defined, considering the organisational order of molecules. Among all three of them, the gas state has the least organised structure, where the constituents are moving chaotically within total volume of recipient. At the other extreme is the solid-state with its well defined structure and stable interactions within its own lattice. Differently from others, the isotropic liquid is a state without a structural order but the interactions are great enough to preserve low range forces keeping the elements together².

Apart from presented prior classical three states of matter an intermediate transitional states were also observed and studied. In particular one, liquid crystalline state (Figure 1), gained the interest of the researches, which helped to establish basic studies and development for commercial applications. Liquid crystals (LCs) are materials with the ability to behave like liquids in meaning of partial mobility and like solids by having short-range transitional order.

General Introduction and Objectives

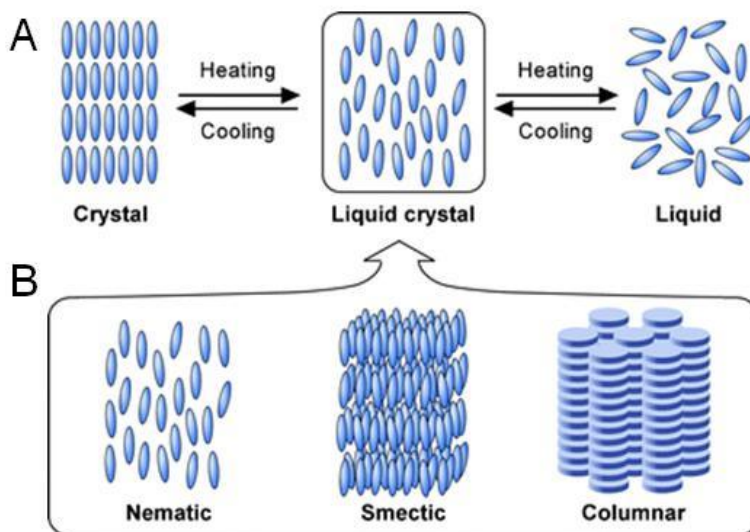


Figure 1. Schematic representation of the molecular arrangement in A-the crystal, liquid crystal and isotropic liquid; B- nematic, smectic and columnar mesophase.

Distinction between thermotropic and lyotropic LCs can be done according to whether the order of its components is determined or changed by temperature or by addition of solvent. Amongst the thermotropic LCs a division can be established into three main types of liquid crystalline phases, which can be observed using polarised optical microscope, during temperature changes:

A. Nematic (N) and cholesteric (N*) phases

The most common and the simplest from all the liquid crystal phases is nematic phase. This phase is characterised by organisational order with randomly aligned molecules, almost as in a liquid, however arranged in the same direction (along director axis). The arrangement of particles in the mesophase can be controlled by electric or magnetic field due to its partial mobility. This fact allows obtaining a material with optical properties of uniaxial crystals. A peculiar kind of nematics is chiral nematic, also called cholesteric from the compound- cholesterol, where the phase was firstly observed. Only chiral molecules (having optical isomers) can create this type of phase; it implies a turning of the molecules relative to each other along an axis perpendicular to them. The angle between neighbouring molecules depends on their grouping in

General Introduction and Objectives

layers, which causes long-range figuring. The chirality induces the azimuth turning from one layer to the next, creating a layer of helically twisted along the director axis (perpendicular to the layers, Figure 2). Perform the chiral layer of 360° around the main axis. Changes in the position of the individual layers to each other can take place under the influence of temperature variations.

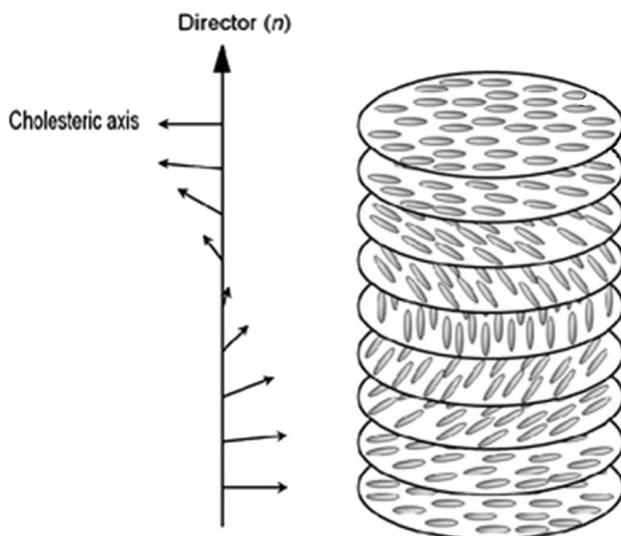


Figure 2. Schematic representation of helically twisted molecular layers among the director axes (n) in cholesteric mesophase.

B. Smectic (S_m) phases

In these phases the molecules are directed along one of the axes and aligned in well-defined layers, what distinguishes them from the nematics. These layers can move relatively between each other and the elements can show a certain distortion angle from the plane of the director axis, causing the existence of various types; for instance, the particles in smectic A are oriented along the axis perpendicular to the plane (z axis), while in the smectic C phase are tilted from this axis. Several smectic phases can be found, which are characterized by varying degrees and type of arrangement of the molecules. Those phases occur at lower temperatures than the nematic phase³.

General Introduction and Objectives

C. Columnar (Col) phases

Columnar phases were discovered in 1977 by Chandrasekhar⁴, in discotically and conically shaped molecules, which are stacked up and form columns. The molecules can be oriented perpendicular to the column axis or have a certain tilt angle. The columns show short-range positional order of elemental units, although in some cases the stacking is very regular: one speaks then of “ordered” phases, as opposed to the so-called “disordered” phases, where the distance between molecules along a column has strong variations. There is no clear-cut distinction between these two kinds of phases that all must be considered as one-dimensional fluids. On the other hand, the columns themselves may be parallel and form a two-dimensional lattice that can be hexagonal, tetragonal, rectangular, or oblique (Figure 3). From this point of view, columnar phases are two-dimensional structures. In the hexagonal phase, which is highly ordered columnar phase, the molecules are not always normal to the column axis. Indeed, hexagonal symmetry is preserved if the molecules are free to rotate about this axis⁵.

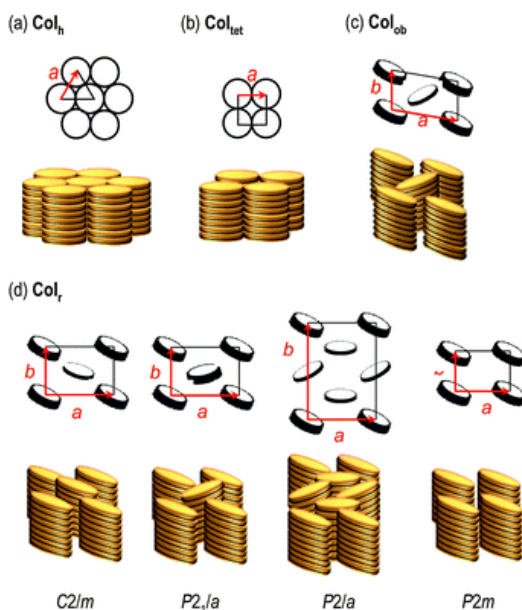


Figure 3. Exemplary packing of disc-like molecules in columnar mesophases: columnar hexagonal (Col_h), columnar tetragonal (Col_{tet}), columnar oblique (Col_{ob}) and columnar rectangular (Col_r).

General Introduction and Objectives

Liquid crystals are organic molecules, which can take the form of discs (discotic) or elongated rods (calamitic) as presented in Figure 4. The structural restriction of dimensions for both geometries is the ratio between the diameter (L) and the thickness (D) or the length (L) and the diameter (D), for discotic or calamitic respectively, and cannot be inferior to 5. This precise limiting value is a result of considering the molecules as a non-spherical; this differentiation provokes positional and possible orientational order. Additionally, the integral part of the design of liquid crystals, apart from the rigid core, which define the geometry, require the presence of one or several tails, guaranteeing the mobility^{6,7}.

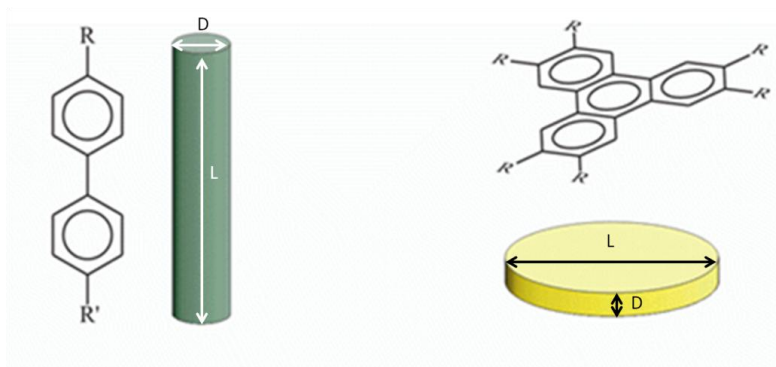


Figure 4. Schematic representation of rod-like and disc-like molecules.

Calamitic Molecules

As previously mentioned, a typical calamitic molecule contains a rigid rod-like core, a flexible tail and polarisable substitutes. In the literature, the scientists are using aromatic moieties, like biphenyl, to ensure elongated stiff base. The Calamitic Liquid Crystals typically exhibit in two phases- nematic and smectic, related to the order degree, where the first one required lower grouping degree than the second. In certain conditions for some LCs the presence of both smectic and nematic phases, on increasing temperature, can be observed^{8,9}. The smectic phase, as a more ordered phase, appears first; because of an increase of the temperature, it loses its order within layers and transitions into nematic, maintaining the positioning among the main axis¹⁰. Various examples of different calamitic molecules are displayed in Figure 5.

General Introduction and Objectives

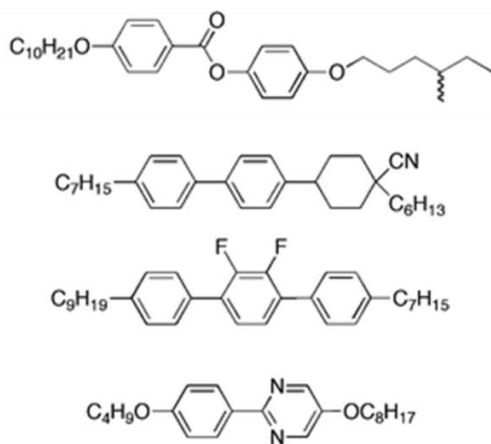


Figure 5. Examples of different calamitic molecules¹¹.

Discotic Molecules

In Figure 6 some examples of organic molecules are demonstrated, which represent different discotic structures; as can be seen, the symmetrical aromatic core is surrounded by aliphatic chains and in some cases form a plane star-shaped structures. The structure of molecules affects its functionality as the ability to form mesophase. Predominantly the Discotic Liquid Crystals tend to array into columnar, discotic nematic and lamellar mesophases; the disc-shaped, form promotes stacking effect, which depends on the degree of organisation and forms the structures, starting from neat piles in nematic mesophase moving to well defined piles with different packing giving lamellar and hexagonal columnar alignment¹².

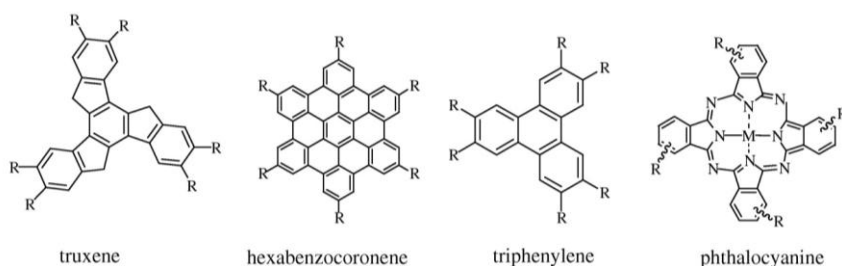


Figure 6. Disc-like molecules with different discotic cores¹³.

General Introduction and Objectives

Liquid Crystalline Polymers

In general, polymers can be described as molecules with high molar mass and made up from several repetitive units (monomers). Polymers, especially those present naturally, play an important role of essential building blocks of nature, showing multitude of functionalities¹⁴.

Upon all different kinds of polymers, the liquid crystalline polymers (LCPs) gained much of an interest in recent years, thanks to their unusual transitional properties. This type of macromolecules preserves the unique liquid-crystalline properties, although their large size, thanks to the presence of mesogens¹⁵. Because of the position of mesogenic group inside the polymer, two types can be distinguished:

- main-chain LCPs: the mesogens are incorporated into backbone and separated by flexible spacers,
- side-chain LCPs: the mesogenic group is attached to the polymeric main-chain as side groups.

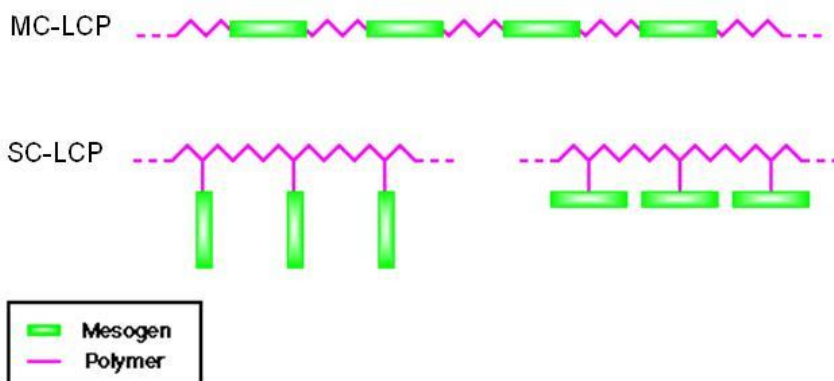


Figure 7. A schematic representation of the MC-LCPc and SC-LCPs.

Apart from the position of mesogenic group in the polymeric structure, also its shape is an important factor, since it determines the liquid crystalline properties. Therefore a distinction between discotic and calamitic polymers can be done, applying the same structural principles of the liquid crystalline moiety^{16, 17}.

General Introduction and Objectives

Strategy for Smart Materials

This thesis is focused on development of two different applications: photosensitive microcapsules and proton conductive membranes. In order to achieve these goals adequate smart materials were prepared and used.

For microcapsule to exhibit photo-response, presence of a photosensitive moiety is needed. For this purpose a new calamitic liquid crystalline polymers were synthesised and we evaluated their applicability for this particular aim.

To obtain a proton conductive membrane, an approach using discotic LCPs was selected, in which the structural design determine polymer self-assembly into columns creating proton pathways.

For clarity reasons, this thesis was divided into two main parts, providing specific introduction for each application and chapters with the experimental results and discussion.

General Introduction and Objectives

Objectives

The objectives of this dissertation can be summarised as follows:

1. Synthesis of liquid crystalline polyesters containing main-chain photosensitive mesogen based on α -methylstilbene, and different spacer groups.
2. Preparation and characterisation of membranes and microcapsules based on liquid crystalline polyesters. To be tested for further application as a shell material in photosensitive microcapsules.
3. Preparation and characterisation of self-assembling columnar side-chain polyamines containing tapered side groups. It is necessary to adopt proper membrane configuration and homotropic alignment of the biomimetic ion channels, to achieve proton transport. For this reason, membrane preparation had to be optimised.
4. Assessment of the potential application of the acquired membranes in direct methanol fuel cells.

The main hypotheses of this work are:

- A) To prepare polyesters with moderately high molecular weight and with photosensitive mesogen will allow the preparation of stable microcapsules.
- B) The presence of α -methylstilbene moiety will help to achieve stable microcapsules, which under UV irradiation will release the core material.
- C) As far as the third objective is concerned: the synthesis of modified polyamine and the selection of suitable path to organise the polymeric material will enable achieving columnar structure of polyamine, perpendicular to membrane surface, necessary to transport ions across the membrane.

General Introduction and Objectives

References

- (1) Schwarz M., Smart Materials, CRC Press by Taylor & Francis Group, 2009, Chapters 2 and 4.
- (2) Blinov L.M., Structure and Properties of Liquid Crystals, Springer Science & Business Media B.V. 2011.
- (3) Demus D., Richter L., Texture of Liquid Crystals, Verlag Chemie, Weinheim-New York 1978.
- (4) Chandrasekhar S., Sadashiva B.K., Suresh K.A., Pramana, 1977, 9, 471-480.
- (5) Oswald P. and Pieranski P., Nematic and Cholesteric Liquid Crystals. Concepts and Physical Properties Illustrated by Experiments, CRC Press, 2005.
- (6) Yang D.-K. and Wu S.-T., Fundamentals of Liquid Crystal Devices, John Wiley and Son, 2006.
- (7) Demus D., Goodby J., Gray G.W., Spiess H.-W., Vill V., ed., Handbook of Liquid Crystals, WILEY-VCH, 1998, p.25-86.
- (8) Singh S., Physics Reports, 2000, 324, 107-269.
- (9) Emelyanenko A.V., Khokhlov A.R., Journal of Chemical Physics, 2015, 142, 204905, 1-12.
- (10) Demus D., Goodby J., Gray G.W., Spiess H.-W., Vill V., ed., Handbook of Liquid Crystals vol. 2A 1998, p.1-46.
- (11) Thompson M.P. and Lemieux R.P., Journal of Material Chemistry, 2007, 17, 5068-5076.
- (12) Demus D., Goodby J., Gray G.W., Spiess H.-W., Vill V., ed., Handbook of liquid crystals vol 2B, 1998, p.491-514
- (13) Cammidge A. N., Philosophical Transactions of the Royal Society A, 2006, 364, 2697-2708.
- (14) Painter P.C., Coleman M. M., Essential of Polymer Science and Engineering, DEStech Publisher, Inc. 2009, p. 1-44.

General Introduction and Objectives

(15) Percec V., Tomazos D., Molecular Engineering of Liquid Crystalline Polymers, Chapter 14 in Comprehensive Polymer Science. Supplement, Vol. 1, ed. Allen G., Bevington C., Pergamon Press, Oxford, 1992.

(16) Kumar S., Chemistry of Discotic Liquid Crystals. From monomers to polymers. CRC Press Taylor & Francis Group, 2011, p. 415-446.

(17) Demus D., Goodby J., Gray G.W., Spiess H.-W., Vill V., ed., Handbook of Liquid Crystals vol. 3 1998, p. 3-66 and p.207-276.

Part 1

Application of Calamitic Liquid Crystalline Polymers

UNIVERSITAT ROVIRA I VIRGILI
LIQUID CRYSTALLINE POLYMERS FOR SMART APPLICATIONS.
Krzysztof Artur Bogdanowicz
Dipòsit Legal: T 1677-2015

This part draws attention to microcapsules, which are able to release the payload under UV irradiation. For this purpose, a family of liquid crystalline polymers was designed and synthesised. The design included incorporation of a calamitic photoisomerisable mesogen- α -methylstilbene, in the polymeric main-chain.

The first chapter describes synthesis and characterisation of photosensitive liquid crystalline polymers and researches their peculiar behaviour as a consequence of an exposure to UV irradiation. The second chapter reports on preparation of microcapsules based on poly(α -methylstilbenesebacate-co- α -methylstilbeneiso-phthlate) and filled with vanillin. A study of the controlled release of the active agent was carried out in aqueous environment. The third chapter discloses structural reasons for photo-induced release based on computational modelling obtained by Dr. Nuno A. G. Bandeira

Microcapsules

Microcapsules are tiny particles that contain active agent or core material surrounded by a coating or shell and can exhibit in various geometries and structures; Figure 1.1 presents three examples of possible capsule structure. The diameters of the microcapsules are usually in the range of 1– 1000 μm . The core materials of the microcapsules can be drugs¹, cells², fragrant oils³, dyes⁴, etc.⁵. The capsule behaviour, as a protective carrier, depends on the mechanical properties and the permeability of the shell, which is influenced by the capsule size, shell thickness, and composition. For handling reasons and needs of specific application encapsulation systems that provide fine control over these parameters, are often desired. Nowadays, capsules can be manufactured from various materials using liquid or solid templates. Pickering or emulsions are suitable liquid templates to produce capsules with polymeric or ceramic shells through interfacial polymerisation, self-assembly, or condensation processes. Besides, the shell composition is sometimes limited to the specific nature of the system⁶.

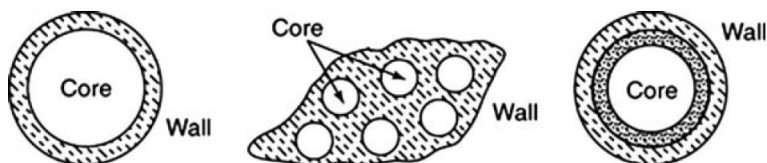


Figure 1.1. Schematic representation of capsules structure: single core is surrounded by continuous one shell (left); multiple cores are suspended in wall matrix (middle); and single core coated by two different wall materials (right)⁷.

Microcapsules can be gained throughout numerous encapsulation processes. For clarity reasons a classification on type A and type B processes will be presented. Type A processes are those where the encapsulation take place in a liquid phase, in example: complex coacervation, polymer-polymer incompatibility and in-liquid drying. On the other hand, as a type B process can be classified process, in which the coating of liquid (also liquid droplets) or solid core occurs via spray or by deposition or solidification in gas phase, for instance spray-drying, fluidised bed, extrusion or spraying into a desolation bath⁷.

Recent studies focus mainly on the capsules preparation for food and biological applications. The main goal is to extend the stability of the payload like polyphenols- obtained from wine waste. For polyphenols a special technique of encapsulations using vibration nozzle method was used, which decreases the possible contaminations. It was proved that these microcapsules allow lowering the degradation rate during 6-month storage at different conditions⁸. Ifeduba et al give another example of food application. Their work was focused on encapsulation of stearidonic acid soybean oil- an important food additive containing plant-originated omega-3 fatty acid. Their finding is promising because of possible use of MD-microcapsules as additive to milk-based yogurt, which enrich its nutritional value⁹. The prolonged stability is also an important factor in biological application for instance in experimental and therapeutic manipulation of cellular activity. A group of Antipina published an article about the intracellular delivery of messenger RNA (mRNA). It is critical to protect mRNA from the inhibitor to strengthen the expression of targeted enzyme. In this article, they used RNA, from HEK293T cells, for *in vitro* studies for future investigation in regenerative medicine¹⁰. In some cases, capsules can be also used to encapsulate microorganisms, for instance

Lactobacillus plantarum strains, to protect them from environmental factors during storage or delivery time¹¹.

Controlled Release

The controlled release of contents from polymeric capsules is of considerable interest in applications such as self-healing materials, nutrient preservation, fragrance release, and drug delivery¹². The functions of capsules are transport and deliver of the beneficial agents “just-in time”. It means the active component is triggered in exact place and time. Triggering is a phenomenon dependent on external stimuli, and the development of suitable initiators plays a key role in the release of capsule contents to provide the desired outcome. Such materials sometimes are named “smart” because of their reaction on a specific way to external stimuli. Various chemical and physical methods have been developed to stimulate upload release.

Core triggering can be performed in different ways:

- Biological triggers are used for drug therapy and vitamin delivery. Even slight changes in pH or the presence of certain chemicals can cause release of their contents in cancer tissue¹³.
- Thermally induced release is applied, for example in agricultural applications, where subtle changes of temperature occur- an increase in soil temperature can initiate delivery of nutrients¹³.
- Magnetically induced release is useful for drug delivery, activating capsules only in tissues subjected to oscillating magnetic fields¹⁴.
- Electric field release is useful in delivering anticorrosive materials only when a metallic surface is compromised¹⁵.

Stimuli-responsive release is still a field, which requires strong investigation to specify new mechanisms and to implement them in new different applications. Several research groups have focused on encapsulating and releasing deliverable materials, in nano- and micro-scale. Photo-responsive release systems are currently investigated according to different approaches, such as remotely triggering of liposome release¹⁶ and light-stimulated in photoresponsive gel droplets¹⁷. Photoisomerization of azobenzene-containing polymers, which have been the object of extensive studies in recent years, establishes a wavelength-dependent steady state between rod-like E-isomer and banana-like Z

isomer¹⁸. In fact, photochromic compounds such as azobenzene derivatives have been used to photo-control membrane properties such as permeability and wettability. Release of β -carotene from microcapsules based on azo-polymer after UV-irradiation, as a result of *E-Z* isomerisation, was reported¹⁹.

In addition, stilbene can be used as a calamitic mesogenic group in photosensitive systems. A vinyl-kind compound under UV irradiation undergoes an isomerisation between *E* and *Z* isomers²⁰. In both cases, isomerisation implies changes in length of mesogenic group- from elongated to contracted form, which has great impact on the entire material (Figure 1.2.). This determines a change in absorbance, as well as in the molecular shape, the polarity and the direction of the transition moment.

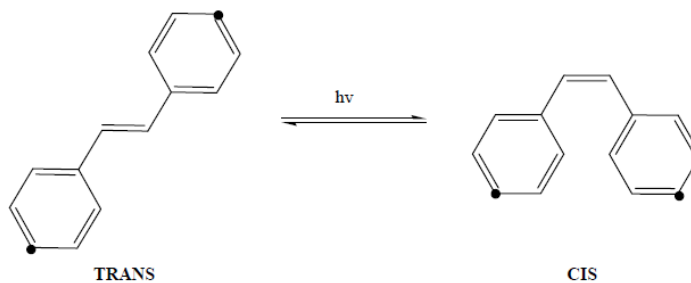


Figure 1.2. Photoisomerization of stilbene.

References

- (1) Zhang, B., *Chemical Engineering Journal* 2015, 275, 235-244.
- (2) Khem, S., *Food Chemistry* 2016, 190, 717-723.
- (3) Fei, X., *Colloids and Surfaces A: Physicochemical and Engineering Aspects* 2015, 469, 300-306.
- (4) Osman, M. Y., *British Journal of Biomedical Science*, 2002, 59, 212-217.
- (5) Wei L., Xing-Xiang Z., Xue-Chen W., Jian-Jin N., *Materials Chemistry and Physics*, 2007, 437.
- (6) Chen P.W., Erb R.M., Studart A.R., *Langmuir*, 2012, 28, 144-152.
- (7) Microencapsulation. *Encyclopedia of Polymer Science and Technology*, John Wiley & Sons 2005.
- (8) Aizpurua-Olaizola O., Navarro P., Vallejo A., Olivares M., Etxebarria N., Usobiaga A., *Food Chemistry* 2016, 190, 614–621.
- (9) Ifeduba, E. A., Akoh C.C., *Food Hydrocolloids* 2015, 51, 136-145.
- (10) Kakran, M., Muratani M., Tng W.J., Liang H., Trushina D.B., Sukhorukov G.B., Ng H.H. and Antipina M.N., *Journal of Materials Chemistry B* 2015, 3, 5842-5848.
- (11) Khem, S., Small D.M., May B.K., *Food Chemistry* 2016, 190, 717-723.
- (12) Esser-Kahn A.P., Odom S.A., Sottos N.R., White S.R., Moore J.S., *Macromolecules*, 2011, 44, 5539–5553.
- (13) Shi X., Tan T., *Biomaterials*, 2002, 23, 4469-4473.
- (14) Hu S.H., Tsai C.H., Liao C.F., Liu D.M., Chen S.Y., *Langmuir*, 2008, 20, 11811-11818.
- (15) Shchukin D.G., Grigoriev D.O, Mohwald H., *Soft Matter*, 2010, 6, 720-725.
- (16) Wu G., Mikhailovski A., Khant H.A., Fu C., Chiu W., Zasadzinski J.A., *Journal of American Chemical Society*, 2008, 8175

- (17) Matsumoto S., Yamaguchi S., Wada A., Matsui T., Ikeda M., Hamachi I., *Chemical Communications*, 2008, 13, 1545-1547.
- (18) Mita I., Horie K., Irao K., *Macromolecules*, 1989, 22, 558-563.
- (19) Tylkowski B., Pregowska M., Jamowska E., Garcia-Valls R., Giamberini M., *European Polymer Journal*, 2009, 45, 1420-1432.
- (20) a) Ding L., Russell T.P., *Macromolecules*, 2006, 39, 6776-6780; b) Riedel D., Cranney M., Martin M., Guillory R., Dujardin G., Dubois M., Sonnet P., *Journal of American Chemical Society*, 2009, 131, 5414-5423.

Chapter 1

Synthesis and Characterization of a New Family of Photoactive Liquid Crystalline Polyesters based on α -methylstilbene

Bartosz Tylkowski, Krzysztof A Bogdanowicz, Veronica Ambrogi,
Albena Lederer, Violetta Patroniak and Marta Giamberini*

*- *Polymer International* **2014**; 63, 315–326

UNIVERSITAT ROVIRA I VIRGILI
LIQUID CRYSTALLINE POLYMERS FOR SMART APPLICATIONS.
Krzysztof Artur Bogdanowicz
Dipòsit Legal: T 1677-2015

Chapter 1

1.2.1. Introduction

Considerable attention has been paid recently to the possibility of controlling mass transfer through membranes using stimuli such as pH, ion concentration or temperature. Systems responsive to such stimuli have been proposed as triggered delivery systems, whose applications lie in several fields such as drug delivery, biosensing, biomaterials, catalysis, etc.¹ Photoirradiation is particularly of great interest since it is a remote stimulus, which can be imparted in a highly selective way without additional structural chemical changes of a system. Polymer conjugates with azobenzene,^{2,3} spirobenzopyran^{4,5} and diarylethenes^{6,7} are among the most investigated photofunctional materials. Reversible changes of polymer polarity or conformation as a result of photoirradiation are caused by photoisomerization of a photochromic unit within the macromolecule.

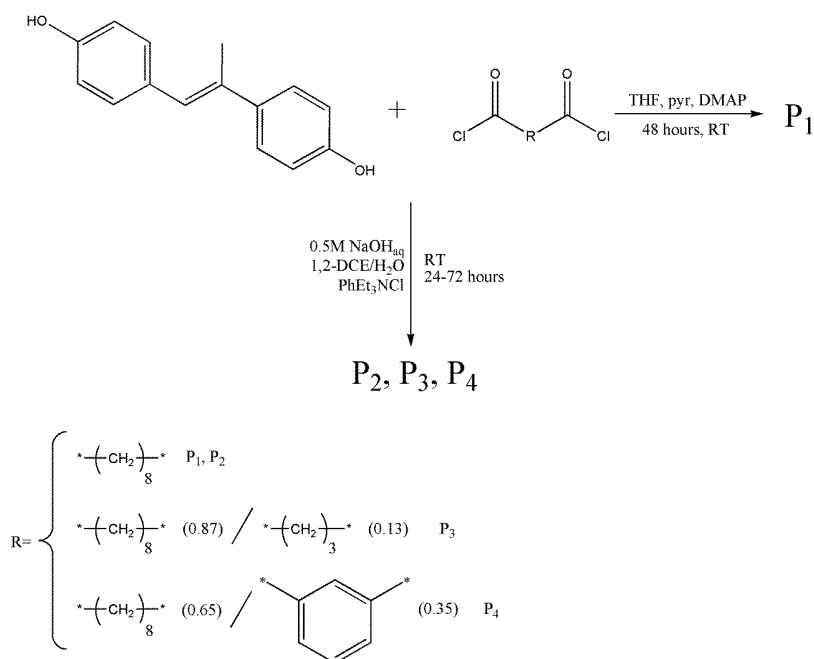
In a previous paper,⁸ we reported the synthesis of a new lightly crosslinked liquid crystalline polyamide, whose state of order could be changed upon application of external stimuli such as temperature and light, and we subsequently prepared microcapsules, based on this polymer as a shell, by interfacial polymerization. The prepared polyamide underwent *E-Z* photoisomerization as a consequence of irradiation with UV light at 364 nm. Release experiments performed in water at 20°C on polyamide microcapsules containing β -carotene showed that release could be triggered by photoisomerization: in the absence of irradiation, release reached a plateau of about 2.5% after a few minutes; in contrast, when the microcapsules were submitted to continuous irradiation with UV light, β -carotene was quickly released and reached 100% release after five minutes.

In the work reported in the present paper, we tackled the preparation of UV-sensitive main-chain liquid crystalline polyesters based on 4,4'-dihydroxy- α -methylstilbene and aliphatic or aromatic acyl dichlorides. 4,4'-dihydroxy- α -methylstilbene is an interesting mesogen which has been widely reported in the preparation of liquid crystalline epoxy resins, elastomers, polyethers and polycarbonates.^{9,10} Moreover, stilbenes are highly photosensitive species, which undergo several photoreactions under light exposure. *E-Z* isomerization is the main photochemical process in low-molecular-weight stilbene derivatives; however, [2+2] photocycloaddition and oxidative cyclization of the *Z*-isomer forming phenanthrene derivatives may also occur.¹¹

In the literature, there are many examples concerning the preparation of photoactive polymer-based films containing stilbene as the

Chapter 1

photoactive unit.¹²⁻¹⁴ Stilbene derivatives in the *E*-state have an extended conformation and are rod-like; in contrast, in the *Z*-state they do not possess the linear form required for liquid crystallinity: as a consequence of such a drastic conformational change, they isothermally become isotropic under UV radiation. For stilbenes, thermal back-reaction has not been reported, since it does not readily take place.¹⁵ For this reason, main-chain polymers based on α -methylstilbene have been reported to exhibit irreversible photochromic properties.¹⁶ In this paper, we report on the synthesis and the full characterization of various liquid crystalline polyesters based on α -methylstilbene to be used in the preparation of UV-sensitive microcapsules. We explored different strategies for the preparation of a liquid crystalline polymer with low or no crystallinity, in order to obtain a system, which could be efficiently photoisomerized. We also investigated the photoisomerization kinetics in chloroform solution. Finally, we prepared a membrane with one of these polymers and found that its water wettability was increased upon photoirradiation.



Scheme 1.1.1. Synthesis route to polymers and copolymers (THF, tetrahydrofuran; pyr, pyridine; DMAP, 4-dimethylaminopyridine; RT, room temperature; 1,2-DCE, 1,2-dichloroethane).

Chapter 1

1.1.2. Materials and Methods

Materials

Sebacoyl dichloride (Fluka, 95%), pyridine (Scharlau, synthesis grade), 4-dimethylaminopyridine (Fluka, 99%), benzyltriethylammonium chloride (Alfa Aesar, 99%), sodium hydroxide (Scharlau, synthesis grade), glutaryl dichloride (Acros Organics, 97%) and isophthaloyl dichloride (Aldrich, 99%) were used as received without any further purification. The solvents were supplied by Scharlau, Aldrich and Fluka and were used as received without previous purification. Aqueous solutions were prepared using Milli-Q water.

Polymer Preparation

4,4'-dihydroxy- α -methylstilbene was synthesized as previously described.⁹ The synthesis route to polymers and copolymers is reported in Scheme 1.1.1.

Polymers and copolymers were prepared according to the following procedures. In the case of poly(α -methylstilbene sebacate) (P1), polymerization was first attempted in homogeneous phase: 4,4'-dihydroxy- α -methylstilbene (1.0 g, 4.4 mmol) and 4-dimethylaminopyridine (0.11 g, 0.9 mmol) were dissolved in 10 mL of dry tetrahydrofuran, and then pyridine (0.70g, 8.8mmol) was added. Afterwards, sebacoyl chloride (1.06 g, 4.4 mmol) was added dropwise. The mixture was kept at room temperature for 48 h under stirring at 900 rpm. The reaction was monitored using thin-layer chromatography on silica plate. Then, solvent was evaporated under reduced pressure. The obtained crude solid was dissolved in 50 mL of chloroform, and precipitated from 100 mL of diethyl ether under moderate stirring. It was then filtered and washed three times using 15 mL of methanol. Purification steps were repeated three times, yielding 286 mg of pure polymer.

Poly(α -methylstilbene sebacate) (P2) and copolymers poly[(α -methylstilbene sebacate)-co-(α -methylstilbene glutarate)] (P3) and poly[(α -methylstilbene sebacate)-co-(α -methylstilbene isophthalate)] (P4) were obtained by conventional liquid-liquid phase-transfer-catalysed interfacial polyesterification, as described by Jegal and Blumstein.¹⁷ The phenol group/chlorine ratio was kept at 1:1 in all the experiments. In a typical preparation of P2, a solution of 4,4'-dihydroxy- α -methylstilbene (1.13 g, 5 mmol, in 20mL of 0.5 mol L⁻¹ aqueous sodium hydroxide solution) was added into a blender that contained 31 mL of ice-cold water,

Chapter 1

47 mL of 1,2-dichloroethane and benzyltriethylammonium chloride (0.35 g, 1.6 mmol) as a phase-transfer catalyst. After 10 min, a solution of sebacoyl chloride (1.20 g, 5 mmol, in 31 mL of 1,2-dichloroethane) was added dropwise. The reaction was performed at room temperature at 400 rpm for 67 h and was monitored using thin-layer chromatography on silica plate. The resulting polymer was precipitated from ethanol (200 mL), filtered and washed three times using a large amount of ethanol. It was purified by repeated dissolution in chloroform (50 mL) and precipitation in ethanol (three times). The product was finally vacuum-dried, yielding 1.58 g of pure polymer.

In the case of copolymers P3 and P4, a slight modification of the previously described phase-transfer-catalysed interfacial polyesterification was used, in which a mixture of sebacoyl chloride with glutaryl chloride (for P3) or isophthaloyl chloride (for P4) was employed. For the synthesis of P3, 0.56 g (2.5 mmol) of 4,4'-dihydroxy- α -methylstilbene was reacted for 24 h with a solution of sebacoyl chloride (0.42 g, 1.75 mmol) and glutaryl dichloride (0.13 g, 0.75 mmol) in 15.5 mL of 1,2-dichloroethane (molar ratio sebacoyl/glutaryl 70/30). An amount of 0.62 g of pure polymer was obtained. In the case of P4, 0.56 g (2.5 mmol) of 4,4'-dihydroxy- α -methylstilbene was reacted for 72 h with a solution of sebacoyl chloride (0.42 g, 1.75 mmol) and isophthaloyl chloride (0.15 g, 0.75 mmol) in 16 mL of 1,2-dichloroethane (molar ratio sebacoyl/isophthaloyl 70/30). An amount of 0.74 g of pure polymer was obtained. All the polymers were fully characterized using ^1H NMR and ^{13}C NMR spectroscopy, as described in the following section. The characteristics of the polymers are reported in Table 1.1.1.

Table 1.1.1. Characteristics of the obtained polymers and copolymers

Polymer	Yield (%)	M_n ($\times 10^{-3}$ g mol $^{-1}$) ^a	M_n ($\times 10^{-3}$ g mol $^{-1}$) ^b	M_w ($\times 10^{-3}$ g mol $^{-1}$) ^b	M_w/M_n^b	X_n^c
P1	14	—	3.1	3.8	1.3	7.9
P2	68	10.2	16.6	41.4	2.5	42
P3	56	20	26.8	66.0	2.5	70
P4	65	16.9	14.6	30.0	2.1	38

^a From ^1H NMR.

^b From SEC-LS.

^c Degree of polymerization from SEC-LS.

Photosensitive P2 flat membranes were prepared by solvent evaporation. Casting solution was prepared by dissolving 2.5 wt% of P2 in

Chapter 1

chloroform and stirring for 24 h in the dark. The solution was drawn using a casting knife of 20 μm in thickness on a flat and dry glass plate. Then the cast film was placed immediately in a dark place in order to protect the photosensitive membrane from light. After 24 h of solvent evaporation at room temperature (20 ± 2 $^{\circ}\text{C}$), the dried film was carefully peeled off from the glass surface and stored in a dark box.

Characterization

Polymers were characterized with ^1H NMR and ^{13}C NMR spectroscopy, using deuterated chloroform (CDCl_3) as a solvent with a Varian Gemini 400 MHz spectrometer (^1H – 400 MHz, tetramethylsilane; ^{13}C – 100 MHz, tetramethylsilane) at room temperature with proton noise decoupling for ^{13}C NMR and using a pulse delay time of 5 s for ^1H NMR. Measurements were carried out at room temperature on 10–15% (w/v) sample solutions. Homonuclear correlation of resonances *via* through-bond J coupling (correlated spectroscopy, COSY) and heteronuclear single quantum correlation (gHSQC) experiments were performed according to standard procedures. A study of the kinetics of isomerization for α -methylstilbene moieties of polymers P2, P3 and P4 was performed by recording ^1H NMR spectra every 2 min during a period of 22 min with a delay time of 5 s and 32 scans.

Calorimetric studies were performed at a heating rate of 10 $^{\circ}\text{C}$ min^{-1} using about 5 mg of sample with a Mettler DSC822e thermal analyser using nitrogen as a purge gas (100 mL min^{-1}) and liquid nitrogen for system cooling. Equipment was previously calibrated with indium (156.6 $^{\circ}\text{C}$) and zinc (419.58 $^{\circ}\text{C}$) pearls using aluminium standard 40 μL crucibles with pin ME-27331.

Molecular weights of polymers were determined using a SEC instrument coupled to a light scattering detector (SEC-LS). SEC measurements were performed using a PL-GPC-50 system with LS and refractive index detection (Agilent Technologies, USA) with PL MIXED-B-LS column (300 \times 7.5 mm) and 10 μm PSgel (Agilent Technologies). The eluent was chloroform at a flow rate of 1.0 mL min^{-1} . The dn/dc values were calculated from the measurements as 0.107 dL g^{-1} for P2. Fitting of the molecular weight/elution volume dependence or sample specific calibration¹⁸ were used to estimate the molecular weight distribution of the lower molecular weight samples. The samples were measured at room temperature.

Chapter 1

TGA was carried out with a Mettler TGA/SDTA 851e thermobalance. Cured samples with an approximate weight of 10 mg were degraded between 30 and 600 °C at a heating rate of 10 °C min⁻¹ in nitrogen (100 mL min⁻¹) measured under normal conditions. The liquid crystalline textures were characterized using optical microscopy between crossed polars (POM), by means of an Axiolab Zeiss optical microscope equipped with a Linkam TP92 hot stage.

XRD experiments at variable temperature were performed with a Siemens D5000 diffractometer in the $\theta - \theta$ configuration, fitted with an Anton Paar TTK temperature chamber. Cu K α radiation was used and graphite was the second monochromator. The Bragg angle step was 0.05° and the time per step was 3 s.

Fourier transform infrared (FTIR) spectra of polymer powders were obtained at room temperature with a FTIR spectrophotometer (680 Plus from Jasco) with a resolution of 4 cm⁻¹ and scanning speed of 2 mm s⁻¹, in transmittance mode. An attenuated total reflection (ATR) accessory with thermal control and a diamond crystal (a Golden Gate heated single-reflection diamond ATR from Specac-Teknokroma) was used to obtain FTIR spectra. The spectra were also collected at higher temperature (200 °C) using a high-stability temperature controller with RS232 control 300 Series® from Specac. Spectra were elaborated by means of Spectra Manager, v. 1.53.04 (Jasco Corp.), and normalized with respect to the aromatic stretching peak at 1505 cm⁻¹.

Photoisomerization was investigated by irradiating samples with UV light at 364 nm using a Vilber Lourmat VL-4 LC-230 V UV lamp for the desired time. The distance between lamp and sample was 1 cm. UV-visible spectra were recorded at room temperature (20 °C) with a UV-visible spectrophotometer (Dinko 8500). First, polymers were dissolved in chloroform to give a concentration in the range 0.9–1.3 g L⁻¹. Then, the spectra were obtained in the wavelength range 190–600 nm using diluted samples (dilution ratio of 1:10).

P2 insoluble fraction after thermal treatment was determined according to the following procedure. P2 powder (200 mg) was placed on a flat ceramic disc covered by a conical funnel in an oven at 200 °C for 15 min. The polymer was then placed on a cellulose filter in Soxhlet apparatus with 200 mL of boiling chloroform. The extraction was performed for 3 h. After the extraction, the filter was dried in an oven at 40 °C for 14 h and finally weighed. This process was repeated until the dry

Chapter 1

insoluble fraction reached constant weight. Finally 12% (24 mg) insoluble fraction was obtained.

Surface and cross-sectional morphologies of P2 membranes were observed at 15 kV with low-vacuum ESEM FEI Quanta 600 apparatus, without sputter coating. Membrane cross-sections were prepared by fracturing in liquid nitrogen. The details of this method have been previously reported.¹⁹ The real sizes of cross-sections of the membranes (10 measurements) were calculated using Image-ProPlus 5® software from ESEM micrographs.

Static contact angles with water on a membrane surface were measured with a Kruss contact angle instrument (Hamburg, Germany) equipped with a motorized pipette (Matrix Technology, Nashua, NH) and deionized water as the probe liquid. The contact angle was measured immediately after placing the water drop (3 μm) on the membrane surface. Measurements were repeated using different areas of the film: for each test reported, at least three drops of water were used.

Dipole moments were calculated with a GAUSSIAN 03 program (ground state DFT and B3LYP/Set lanL2DZ level).²⁰ Structures pre-optimized semi-empirically with HYPERCHEM-7.52 (PM3 Hamiltonian) were used as starting points.

1.1.3. Results and Discussion

Polymer Synthesis and Characterization

The aim of this work was the preparation of liquid crystalline polymers, containing a photoisomerizable moiety, to be used as starting materials for microcapsules, whose release properties can be triggered by UV light. The reaction is shown in Scheme 1. The characteristics of all the polymers and copolymers obtained are reported in Table 1.

The synthesis of esters and copolyesters based on 4,4'-dihydroxy- α -methylstilbene by interfacial polymerization was reported by Jegal and Blumstein.¹⁷ In our case, we first explored the synthesis of poly(α -methylstilbene sebacate) by polymerization in homogeneous phase (preparation of P1). Using this procedure, only oligomers can be obtained, as shown by SEC-LS analysis (Table 1.1.1): as a matter of fact, no light scattering signal is observed for this sample and the degree of polymerization is as low as 7.9. Moreover, the reaction yield is low (14%). ¹H NMR and ¹³C NMR spectra of P1 are reported in the supporting information (Figs S1.1.1 and S1.1.2, respectively). ¹H NMR and ¹³C NMR

Chapter 1

assignments for P1 are the same as for P2, a detailed discussion of the NMR results for which is reported below.

Since polymerization in homogeneous phase does not lead to the desired polymer, we tried liquid–liquid phase-transfercatalysed interfacial polyesterification. Table 1.1.1 shows that this procedure is successful, since it gives poly(α -methylstilbene sebacate) with a quite high yield and satisfactory degree of polymerization. As a matter of fact, SEC-LS shows that, in this case, the weight-average molecular weight (M_w) of the resulting polymer is about 41 000 g mol⁻¹ and the degree of polymerization about 42.

¹H NMR and ¹³C NMR spectra of polymer P2 are shown in Figs 1.1.1 and 1.1.2. The NMR assignments are reported in Table 1.1.2. In the ¹H NMR spectrum, the signals corresponding to the vinyl proton g and to the methylic protons f appear as singles at 6.8 and 2.25 ppm, respectively (Table 1.1.2 and Figure 1.1.1, top). They are attributed to the α -methylstilbene moiety in the *E*-form. Moreover, two singles at higher field, i.e. at 6.4 and 2.2 ppm, respectively, are seen. These are attributed to the vinyl proton and to the methylic protons of the α -methylstilbene moiety in the *Z*-form. From the comparison of the integrated areas of the peaks at 2.18 and 2.25 ppm, and at 6.4 and 6.8 ppm, respectively, we calculate that the amount of the as-synthesized P2 in *Z*-form is about 3%. It must be pointed out that the ¹H NMR spectrum of 4,4'-dihydroxy- α -methylstilbene monomer (supporting information, Fig. S1.1.3) already shows the presence of 6% *Z*-form.

Chapter 1

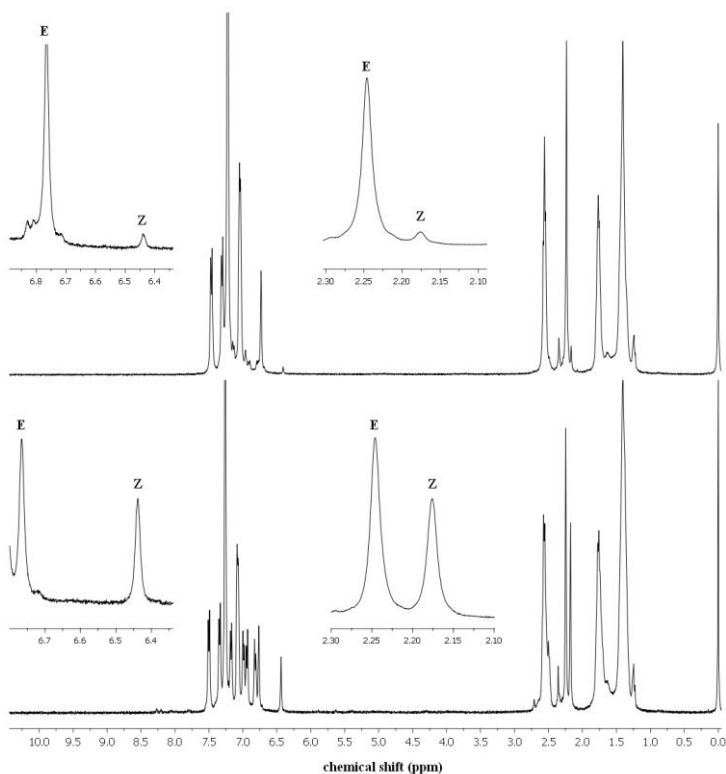


Figure 1.1.1. ^1H NMR spectra in CDCl_3 of P2 before (top) and after (bottom) irradiation for 20 min. The insets show magnifications of vinyl (6.3–6.9 ppm) and methylene (2.10–2.30 ppm) proton regions.

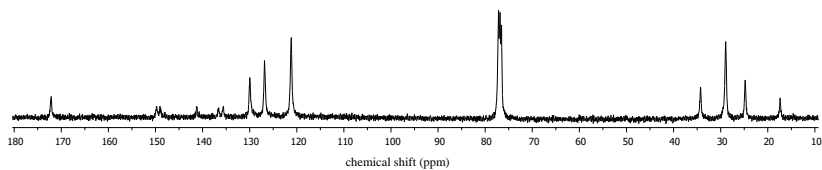


Figure 1.1.2. ^{13}C NMR spectrum in CDCl_3 of P2 before photoirradiation.

Chapter 1

Table 1.1.2. NMR assignments for polymer P2

¹ H NMR		¹³ C NMR	
Chemical shift (ppm)	Assignment ^a	Chemical shift (ppm)	Assignment
1.24	c	17.7	10
1.76	b	25.1	4
2.18	f _Z	29.2	3
2.25	f _E	34.6	2
2.57	a	121.5	6
5.59	Terminal phenolic	127.2	11
6.44	g _Z	130.3	7
6.77	g _E	135.9, 136.9	8 ^o , 8
7.07	d	141.5	9
7.33	e	149.4, 150.1	5 ^o , 5
7.49	e ^o	172.5	1
11.13	Terminal carboxylic		

^a Subscripts Z and E correspond to atoms in Z- and E-form, respectively.

On irradiating P2 at 364 nm for 20 min, its ¹H NMR spectrum is markedly changed (Fig. 1.1.1, bottom) and the intensities of the peaks at 6.4 and 2.2 ppm are considerably increased, as discussed later in the article. The analysis of the ¹H NMR spectrum after UV irradiation also allows us to exclude the presence of detectable amounts of products deriving from [2+2] photocycloaddition and oxidative cyclization reactions as a consequence of UV irradiation in the previously described conditions. As far as the ¹³C NMR spectrum is concerned (Fig. 1.1.2), no variations are found after irradiating P2 at 364 nm for 20 min.

In the ¹H NMR spectrum before irradiation, two very small peaks are also found at 5.6 and 11.1 ppm: they are attributed to the protons from the terminal phenolic and carboxylic groups, respectively. From the comparison of the integrated areas of these peaks with those of the signals of the vinyl protons, we can estimate a number-average molecular weight (M_n) of about $10.2 \times 10^3 \text{ g mol}^{-1}$. This value is lower than that obtained using SEC-LS (16.4×10^3 ; Table 1.1.1). This is not surprising, since it refers to the number-average molecular weight; also, the integration of the peaks at 5.6 and 11.1 ppm is probably affected by a considerable error.

We also prepared copolymers based on the α -methylstilbene moiety, in which the introduction of some amount of different spacers was expected to lead to a less regular polymeric structure, to decrease the glass transition temperature (T_g), possibly to inhibit crystallization and to modify the nature and stability of the liquid crystalline phase. For this

Chapter 1

reason, we first reacted 4,4'-dihydroxy- α -methylstilbene with a mixture of acyl chlorides, namely sebacoyl and glutaryl chloride, in the theoretical molar ratio 70:30, in order to have a mixture of shorter and longer flexible spacers in the final polyester P3. This copolymer was obtained in good yield (56%) and has M_w about $66 \times 10^3 \text{ g mol}^{-1}$.

^1H NMR and ^{13}C NMR assignments for this copolymer are shown in Table 1.1.3. The spectra are reported in the supporting information (Figs S1.1.4 and S1.1.5). In this case, the signals relating to the methylenic protons in position α and β to the carbonyl of the sebacoyl unit appear overlapped with the signals of methylenic protons from the glutaryl unit. However, by comparing the integrated areas relating to the vinylic proton of α -methylstilbene unit at 6.8 ppm with the integrated areas of γ -methylenic protons of the sebacoyl unit at 1.4 ppm, we can calculate that the actual ratio of sebacoyl and glutaryl units in the final polymer is 87:13. In the case of P3, no signal is observed at 6.4 ppm, corresponding to the vinyl proton of the α -methylstilbene in the *Z*-form; however, a signal at 2.18 ppm, corresponding to the methyl proton of the same unit in the *Z*-form, can be detected. Therefore, from the comparison of the integrated areas of the peaks at 2.18 and 2.25 ppm, we calculate that the amount of the as-synthesized P3 in *Z*-form is about 6%. Detectable amounts of products deriving from [2+2] photocycloaddition and oxidative cyclization reactions are not found in the ^1H NMR spectrum after irradiation.

In the ^1H NMR spectrum of P3 (Fig. S1.1.4) we also detect signals at 4.9 and 9.9 ppm, which correspond to protons from phenolic and carboxylic end groups, respectively. From the comparison of the integrated areas of these peaks with the area of the vinyl proton at 6.8 ppm, we can estimate the degree of polymerization as 53, corresponding to M_n of approximately $20 \times 10^3 \text{ g mol}^{-1}$. These values are in a good agreement with the results from SEC-LS, which gives M_n of about $27 \times 10^3 \text{ g mol}^{-1}$ and a degree of polymerization of 70 (Table 1.1.1), if we take into account the different sensitivity of the two techniques.

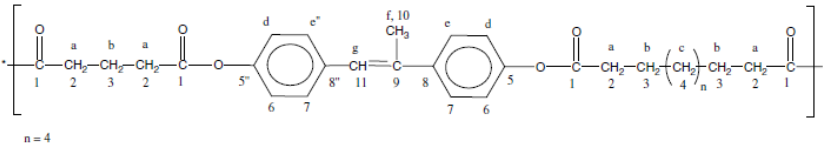
In a second preparation, we reacted 4,4'-dihydroxy- α -methylstilbene with a mixture of sebacoyl chloride and isophthaloyl chloride in the theoretical molar ratio 70:30. The presence of the isophthalic unit should, in our hypothesis, force the polymeric chains to bend and could therefore increase the polymer free volume, thus reducing T_g ; the introduction of such irregularities in the structure should also prevent the polymer from organizing into a crystalline structure. The ^1H NMR spectrum of the resulting copolymer, P4, is shown in Fig. 1.1.3,

Chapter 1

while the NMR assignments are reported in Table 1.1.4. The ^{13}C NMR spectrum of P4 is reported in the supporting information (Fig. S1.1.6).

As expected, the ^1H NMR spectrum shows, apart from the signals relating to α -methylstilbene and sebacoyl units, three signals at 7.7, 8.5 and 9.0 ppm, which can be attributed to the protons of the isophthaloyl unit. Moreover, the signals relating to the vinyl proton and to the methyl protons, as well as those relating to the aromatic protons of the α -methylstilbene unit, appear split into three peaks of different intensities. This is attributed to the fact that each α -methylstilbene moiety can be bound to a sebacoyl group (S) or to an isophthaloyl group (I). This gives rise to the existence of four possible dyads, S-S, I-S, S-I, I-I, which, in principle, correspond to different values of the chemical shift in the ^1H NMR spectrum. It is reasonable to assume that, in our case, the chemical shifts of I-S and S-I dyads are very close and give overlapped signals in the spectrum: for this reason, only three signals are observed. According to the ^1H NMR spectrum of poly(α -methylstilbene sebacate), the peak at 6.78 ppm is attributed to the S-S dyad, while the peaks located at lower fields in P4 spectrum are attributed to the I-S plus S-I dyad (6.81 ppm) and to the I-I dyad (6.86 ppm).

Table 1.1.3. NMR assignments for polymer P3



^1H NMR		^{13}C NMR	
Chemical shift (ppm)	Assignment ^a	Chemical shift (ppm)	Assignment
1.41	c	17.5	10
1.78	b	24.9	4
2.18	f_Z	29.1	3
2.25	f_E	34.4	2
2.58	a	115.1	6 terminal
4.92	Terminal phenolic	121.4	6
6.77	g_E	127.0	11
7.09	d	130.1	7
7.33	e	153.8, 136.8	8 ^z , 8
7.49	e^E	141.4	9
9.89	Terminal carboxylic	149.2, 150.0	5 ^z , 5
		172.3	1
		172.3	1

^a Subscripts Z and E correspond to atoms in Z- and E-form, respectively.

Chapter 1

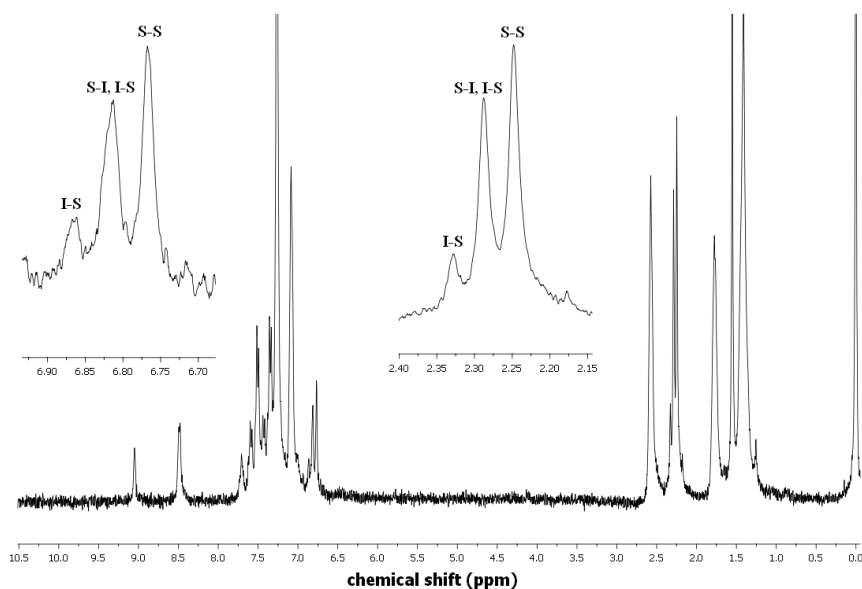


Figure 1.1.3. ^1H NMR spectrum in CDCl_3 of P4. The insets show magnifications of vinyl (6.7–6.9 ppm) and methylic (2.15–2.40 ppm) proton regions.

Similar to P2, in the case of P4 equivalent signals at higher fields corresponding to the α -methylstilbene moiety in the *Z*-form are also found. In this case, for instance, a triplet between 6.44 and 6.53 ppm attributed to the vinyl proton is also detected: this signal is split into a triplet due to the existence of different dyads, as explained before. From the comparison of the integrated areas of the triplets corresponding to the vinyl proton in the *E*-form (centred around 6.8 ppm, as previously explained) and to the vinyl proton in the *Z*-form, we can calculate that the amount of α -methylstilbene moieties in *Z*-form is about 3% in the as-synthesized P4. The analysis of the spectrum recorded after irradiation allows us to exclude also in the case of P4 the presence of products deriving from [2+2] photocycloaddition and oxidative cyclization reactions.

The actual sebacoyl/isophthaloyl ratio in P4 is calculated from the integrated areas of the peaks corresponding to the isophthaloyl group and of the whole group of signals corresponding to the vinyl proton, and a value of 65:35 is obtained.

The integrated areas of the peaks located at 6.77, 6.81 and 6.86 ppm (Fig. 1.1.3) allow us to confirm that the distribution of the two sebacic (S) and isophthalic (I) comonomers is Bernoullian, with a random

Chapter 1

placement along the copolymer chain. As a matter of fact, if we make this assumption, given that the experimental amount of S versus I is 65 to 35, then the probability PS-S of finding a dyad S-S is

$$PS-S = (0.65)^2 = 0.42 \quad (1)$$

while the total probability PI-S of finding a dyad I-S or S-I is

$$2 \times PI-S = 2 \times PS-I = 2 (0.65 \times 0.35) = 0.46 \quad (2)$$

and finally the probability PI-I of an I-I dyad is

$$PI-I = (0.35)^2 = 0.12 \quad (3)$$

Therefore, the integrated areas of the signals corresponding to the S-S, I-S+S-I and I-I dyads should be in the ratio 0.42:0.46:0.12. The experimental result is in good agreement with this hypothesis, since the ratio between the areas of the peaks at 6.77, 6.81 and 6.86 ppm is 0.39:0.44:0.17.

As can be seen in the ^1H NMR spectrum of P4 in Fig. 1.1.3, there are two signals at 4.89 and 10.20 ppm that correspond to the phenolic and carboxylic protons of end groups, respectively. From the comparison of the integrated areas of these peaks and the whole set of signals relating to the vinyl protons between 6.9 and 6.4 ppm, we can give an estimation of the degree of polymerization of P4, which is about 44. This corresponds to an approximate molecular weight of $16.9 \times 10^3 \text{ g mol}^{-1}$, which is in agreement with $M_n = 14.6 \times 10^3 \text{ g mol}^{-1}$ as determined from SEC-LS.

Mesomorphic and Thermal Characterization

All the synthesized polymers were characterized using POM, DSC and XRD. DSC thermograms of P1–P4 and XRD patterns of some selected samples are reported in the supporting information (Figs S1.1.7 and S1.1.8).

In the case of P1, only oligomers corresponding to a degree of polymerization of 8 are obtained. The oligomers exhibit a liquid crystalline behaviour between 111 and 190 °C, as evident from DSC, POM and XRD analyses. From POM observations, the typical Schlieren texture, characteristic of nematic phase, is seen (Fig. 1.1.4(a)), while XRD performed at 140 °C shows evidence of a halo centred at 2θ about 20°. The calorimetric features of P1 are reported in Table 1.1.5. The

Chapter 1

calorimetric analysis of P2 shows two endothermic peaks, one located at 175 °C and the other at 226 °C (Table 1.1.5). Birefringent texture of P2 at 185 °C is shown in Fig. 1.1.4(b). According to POM observations and XRD analysis, the two endotherms are attributed to the polymer melting to a nematic phase and to its clearing, respectively. However, from POM observation, a progressive increase of polymer viscosity is also observed. Furthermore, DSC second heating scan performed on a sample previously heated above 200 °C shows a slightly higher T_g value and lower values of clearing temperature and enthalpy. This suggests that, on heating above 200 °C, reactions that involve the central double bond of the α -methylstilbene moiety can occur to some extent; these reactions thus destroy the mesogenic core and lead to a partially crosslinked material.

Figure 1.1.5 shows the FTIR spectra at room temperature of P2 powder before and after heating for 15 min at 200 °C. These spectra seem to confirm our hypothesis, since the intensities of the bands at 845 and 1290 cm^{-1} (which can both be attributed to the phenyl ring + C–H deformation in (*E*)- α -methylstilbene) and 1604 cm^{-1} (assigned to the phenyl out-of-plane vibration of (*E*)- α -methylstilbene¹⁴) are strongly reduced as a consequence of heating. Furthermore, thermal treatment of P2 at 200 °C for 15 min, followed by Soxhlet extraction with chloroform, leads to 12 wt% insoluble fraction, thus confirming that crosslinking of the double bond of the α -methylstilbene moiety takes place to some extent under those conditions. Similar behaviour upon heating above 200 °C is found also in the case of P3 and P4.

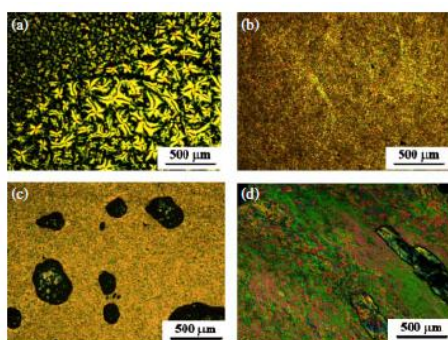


Figure 1.1.4. POM micrographs: (a) P1, 182 °C, on cooling from the isotropic phase; (b) P2, 185 °C, first heating; (c) P3, 161 °C, second heating; (d) P4, 194 °C, first heating. Heating or cooling rates: 10 °C min^{-1} .

Chapter 1

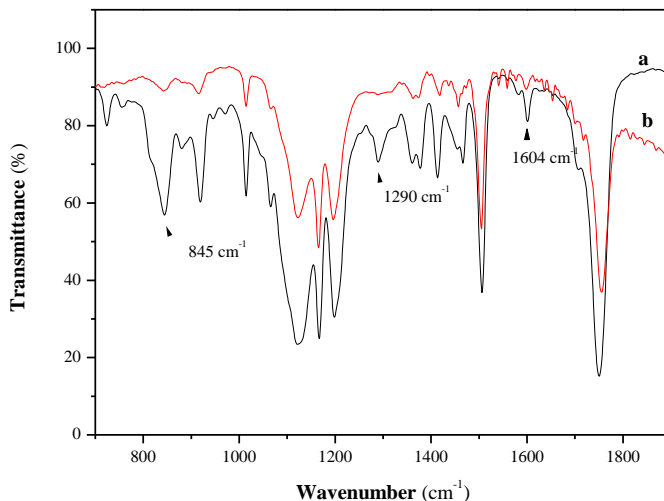


Figure 1.1.5. Normalized FTIR spectra at room temperature of P2 powder (a) before and (b) after heating for 15 min at 200 °C.

The thermal features of P3 are reported in Table 1.1.5, which shows that this polymer exhibits a considerably lower T_g with respect to poly(α -methylstilbene sebacate), though its value is still quite high, i.e. 78 °C. Moreover, P3 is still partially crystalline, though the extent of crystallinity is reduced, as can be inferred from the melting enthalpy and entropy reported in Table 1.1.5. Upon melting at 158 °C, P3 exhibits a nematic phase up to 187 °C, as evident from POM and XRD results. The nematic texture of P3 is shown in Fig. 1.1.4(c).

The introduction of about 30 mol% isophthaloyl moiety is successful in lowering T_g and inhibiting crystallization in the final polymer: DSC analysis performed on P4 shows T_g at 45 °C and no melting endotherm; moreover, no crystalline phase is detected using XRD. DSC shows an endotherm centred at 238 °C corresponding to 2.4 kJ mol⁻¹. POM observation shows a nematic thread-like texture (Fig. 1.1.4(d)); the clearing point is detected at about 240 °C. XRD shows evidence of a broad halo corresponding to approximately 4 Å, typical of the nematic phase, in the whole temperature range under examination.

The thermal stability of polymers P1–P4 was investigated using TGA under nitrogen atmosphere (Table 1.1.6; supporting information, Fig.

Chapter 1

S1.1.9). As far as P1 and P2 are concerned, thermal stability increases with increasing molecular weight, as expected, and the temperatures corresponding to 5% weight loss are 292 and 398 °C, respectively; T50% and the weight residue for P2 are also higher than in the case of P1. As far as P2 and P4 are concerned, single-step decomposition is found, starting at about 370 °C, while in the case of P3 another decomposition step appears, with an onset at about 300 °C; T5% and T50% are lower for P3 than for P2 and P4. On the other hand, P3, which contains 13 mol% glutaryl spacer, shows higher residue, followed by P4, which contains 35 mol% aromatic spacer, and finally by P2, which has a fully aliphatic quite long spacer. In the case of main-chain liquid crystalline polyurethanes based on α -methylstilbene, it was reported that the spacer length and nature significantly influence the decomposition behaviour.²¹ In the case of P2, P3 and P4, one should also take into account that heating leads not only to thermal decomposition, but also to reactions of the α -methylstilbene moiety, which give rise to partially crosslinked products. Thermal decomposition of these products is not easy to predict, since it can depend, for example, on the tightness of the obtained network.

Table 1.1.4. NMR assignments for polymer P4

¹ H NMR		¹³ C NMR	
Chemical shift (ppm)	Assignment ^a	Chemical shift (ppm)	Assignment
1.41	c	17.5	10
1.78	b	24.9	4
2.18	f _Z	29.0	3
2.29, 2.33, 2.38	f _E	34.4	2
2.57	a	121.3	6
4.89	Terminal phenolic	127.0	11
6.44, 6.48	g _Z	127.1	16
6.77, 6.81, 6.86	g _E	130.1	7
7.07	d	130.3	13, 14
7.33, 7.38	e	135.0	15, 8
7.49, 7.59	e''	141.4	9
7.71	i	149.9	5
8.48	h	157.9	5 terminal
8.98	j	164.3	12
10.20	Terminal carboxylic	172.3	1

^a Subscripts Z and E correspond to atoms in Z- and E-form, respectively.

Chapter 1

Table 1.1.5. Calorimetric features of polymers from first heating scan

Polymer	T_g (°C) ^a	T_m (°C) ^b	T_c (°C) ^c	ΔH_m (kJ/mol) ^d	ΔS_m (J/mol K) ^d	ΔH_c (kJ/mol) ^d	ΔS_c (J/mol K) ^d	Mesophase ^e
P1	71	111	190	9.71	25.3	5.56	12.0	N
P2	135	175	226	6.71	15.0	5.57	11.2	N
P3	78	158	187	2.30	5.3	1.90	4.1	N
P4	45	-	238	-	-	2.43	4.7	N

^a Glass transition.

^b Melting temperature.

^c Clearing temperature.

^d Per mole of repeat unit.

^e N:nematic.

Table 1.1.6. Results of TGA of polymers

Polymer	$T_{5\%}$ (°C) ^a	$T_{50\%}$ (°C) ^b	Residue (%)
P1	292	442	3.1
P2	398	455	8.5
P3	307	441	25.3
P4	406	460	18.5

^a Temperature corresponding to 5 wt% loss.

^b Temperature corresponding to 50 wt% loss.

Polymer Photoisomerization

As already stated, stilbene derivatives in the *E*-state possess a rod-like conformation which is required for liquid crystallinity, while in the *Z*-state they have a bent conformation; therefore, they isothermally become isotropic as a consequence of *E*-*Z* photoisomerization. Such a marked conformational change should be accompanied by a notable change in transport properties, i.e. on changing the state of order from liquid crystalline to isotropic, barrier properties should become less significant.

Thermal *Z*-*E* isomerization has not been reported in the case of stilbene derivatives, but 254 nm UV light can be used to investigate the *Z*-*E* photoisomerization of stilbene based compounds.²² Therefore, on

Chapter 1

irradiating first with 364 nm and subsequently with 254 nm UV light, we should be able to induce first *E*-*Z* photoisomerization, followed by *Z*-*E* photoisomerization. This, in turn, should correspond to isothermal isotropization followed by anisotropization of the polymer under investigation. In order to verify this phenomenon, we irradiated a P4 film under POM observation, and used the liquid crystalline texture exhibited by this sample as a probe to monitor sample isotropization/anisotropization.

Figure 1.1.6 shows the POM micrographs of P4 at 180 °C. It can be noticed that the liquid crystalline texture of P4 progressively disappears on irradiating at 364 nm, while it is restored after irradiation at 254 nm. These isotropization/anisotropization cycles could be repeated several times.

Figure 1.1.7 shows the UV absorption spectra of P2 in chloroform before and after 45minUVirradiation at 364 nm. Before irradiation, a peak located at 305 nm, with a shoulder at about 296 nm, is evident. It has been reported that, at 366 nm, the *E*-form of stilbene absorbs to a greater extent than the *Z*-form; as a result, the population of the *Z*-form increases. The resulting decrease in the population of the *E*-form leads to a decrease in the absorption band obtained from the system in the wavelength region used in isomerization.²³ In the case of thin films of polyimides containing stilbene moieties in the backbone, it was shown that, on UV irradiation, the absorption maximum at 330 nm, characteristic of stilbene units in the *E*-configuration, gradually decreases; at the same time, a band gradually appears at about 280 nm, corresponding to (*Z*)-stilbene units.²⁴ In the case of P2 in chloroform solution, after irradiation, the maximum of the absorption peak at 302 nm, which can be attributed to the α -methylstilbene moieties in the *E*-form, is displaced to 290 nm. This confirms that P2 undergoes photoisomerization under these conditions. UV absorption spectra of P3 and P4 in chloroform, before and after 45 min UV irradiation at 364 nm, exhibit the same features already discussed for P2. We therefore conclude that all the synthesized polymers undergo photoisomerization under the reported conditions.

Chapter 1

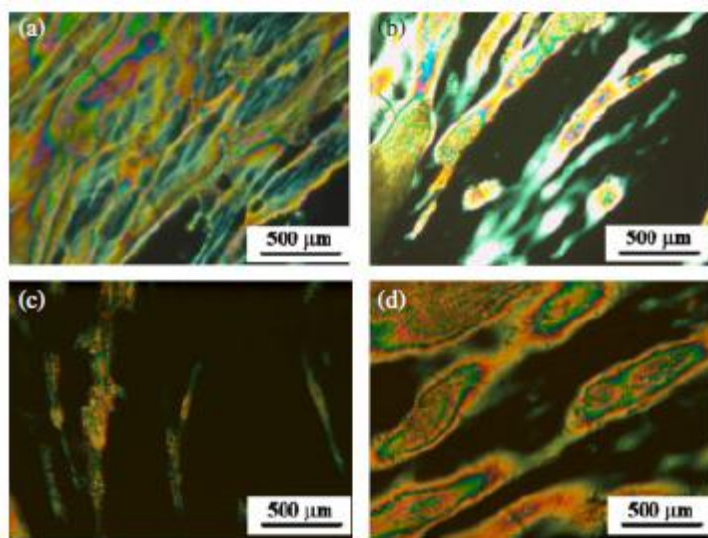


Figure 1.1.6. POM micrographs of P4 film at 180 °C: (a) before photoirradiation; (b) after 10 min photoirradiation at 364 nm; (c) after 20 min photoirradiation at 364 nm; (d) after 20 min photoirradiation at 364 nm followed by 10 min photoirradiation at 254 nm.

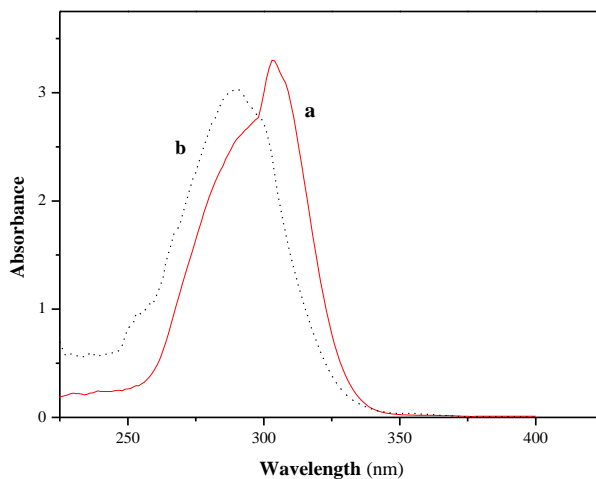


Figure 1.1.7. UV absorption spectra of P2 in chloroform (a) before and (b) after 45 min UV irradiation at 364 nm.

Chapter 1

Table 1.1.7. Kinetic data for *E*–*Z* photoisomerization in CDCl₃ of polymers at 20 °C.

Polymer	k ($\times 10^4$ s ⁻¹)	$\tau_{1/2}$ ($\times 10^{-3}$ s)
P2	4.8 ± 0.2	1.4
P3	3.66 ± 0.06	1.9
P4	1.64 ± 0.01	4.2

Triggering *E*–*Z* isomerization can perturb the chemical environments of protons, which lie in close proximity to the vinyl bond of α -methylstilbene, and this effect can be quite extended when this moiety is located within a polymer backbone. For cases when these perturbations are sufficiently great, ¹H NMR spectroscopy can be successfully used to detect the isomerisation process. Figure 1.1.1(b) shows the ¹H NMR spectrum of P2 in CDCl₃ after 20 min irradiation at 364 nm. Comparing with the spectrum obtained before photoirradiation (Fig. 1.1.1(a)), it can be noticed that all the peaks relative to the protons of α -methylstilbene units are clearly duplicated, since signals of similar intensities, with the same multiplicity and upfield shift, appear. These peaks are attributed to the *Z*-form of the mesogenic unit. The chemical shifts of *Z*- and *E*-forms are sufficiently far from each other and their peak area provides a good scale for following quantitatively the progress of photoisomerization with respect to kinetic aspects. As a matter of fact, comparison of the integrated areas of the vinyl proton signals at 6.8 and 6.4 ppm, and of the methylic proton signals at 2.25 and 2.2 ppm, allows us to calculate the amount of each form after photoirradiation. The same procedure can also be applied in the case of the ¹H NMR spectra of P3 and P4 in CDCl₃.

The relative amount of *E*-form at different irradiation times is calculated according to the following equation:

$$\pi(t) = \frac{A_E}{A_E + A_Z} \quad (4)$$

where $\pi(t)$ is the amount of *E*-form after irradiation time t , A_E is the peak area of the *E*-form and A_Z is the peak area of the *Z*-form. A plot of $\ln[\pi]t/[\pi]_0$ with respect to irradiation time gives a straight line, the slope of which is equal to $-k$, thus confirming that the photoisomerization process follows a first-order rate law, as reported.²⁵ However, in the case of an optically active copolymer of (–)-menthyl acrylate with *trans*-4-

Chapter 1

vinylstilbene, it was also reported that *E-Z* photoisomerization does not obey first-order kinetics, in accordance with the restricted mobility of stilbene chromophores attached to a polymer chain.¹² Table 1.1.7 reports rate constants and half-life values calculated at 20 °C for the *E-Z* photoisomerization process of polymers P2, P3 and P4 in CDCl₃. The values of kinetic constants are all in the same range, i.e. ca 10⁻⁴ s⁻¹; P4 is found to exhibit the lowest value.

For low-molecular-weight species, it has been reported that, on increasing the viscosity of the medium, the activation energy involved in the *E-Z* transformation can increase, thus slowing down the process.²⁶ In the case of photoisomerizable species introduced into a polymer host without chemical linking, it was found that the rigidity of the host matrix largely influences the process rate. In the case of systems where the active moiety is covalently attached to the polymer, photoisomerization rate can decrease even further and the activation energy shows a temperature dependence.²⁷ Therefore, in order to perform a first check for the occurrence of photoisomerization also in the bulk state in our systems, we prepared a membrane based on one of the synthesized polymers, namely P2, which exhibits the fastest isomerization kinetics in chloroform solution, and investigated its wetting properties upon UV irradiation.

Figure 1.1.8(a) shows an ESEM image of P2 membrane surface while Fig. 1.1.8(b) shows the cross-sectional morphology. As is typically expected for membranes prepared by solvent evaporation, the P2 film exhibits a dense and non-porous structure.²⁸ Membrane thickness calculated using Image-ProPlus 5® software from the ESEM micrographs is 6.2±0.3 μm.

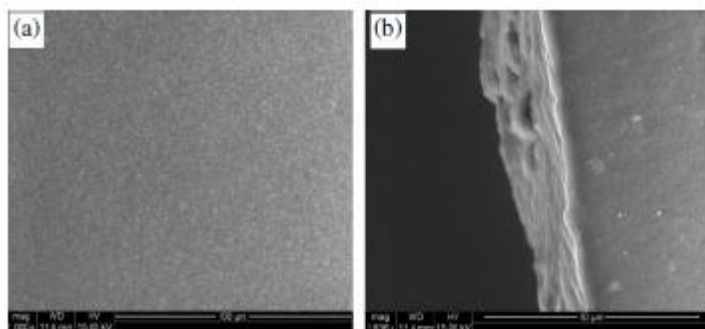


Figure 1.1.8. ESEM micrographs of (a) the surface and (b) cross-section of P2 membrane.

Chapter 1

The wettability of the P2 membrane before and after UV irradiation was investigated by measuring the static contact angle (CA) with water, which is shown in Fig. 1.1.9. The value of the CA with water for a flat P2 membrane before irradiation (Fig. 1.1.9(a)) is $95\pm 2^\circ$. After exposure to UV light (365 nm) for 30 min the CA is $85\pm 2^\circ$ (Fig. 1.1.9(b)), that is, it is decreased by about $10\pm 2^\circ$. This change can be reasonably ascribed to *E-Z* photoisomerization of α -methylstilbene moieties on the membrane surface. In fact, according to our calculations, in the *E*-state, α -methylstilbene moieties have a smaller dipole moment (0.27 D), while *E-Z* isomerization induced by UV light irradiation leads to a large increase in the dipole moment (0.56 D). Moreover, the enhanced wettability can be also related to a change in surface roughness on photoisomerization.²⁹

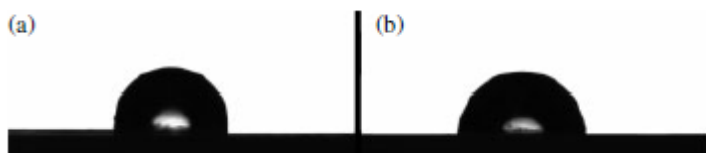


Figure 1.1.9. Static contact angles with water for a P2 membrane: (a) before irradiation; (b) after UV irradiation at 365 nm. The contact angle decreases, revealing that the membrane is more hydrophilic after irradiation.

The change in wettability of the P2 membrane is just a first clue as to the possibility of triggering the properties of a membrane and microcapsules based on the synthesized polymers. A forthcoming paper will deal with the preparation and characterization of membranes and microcapsules from P2, P3 and P4, as well as with the change of their properties (such as morphology, roughness and permeability) upon photoirradiation.

1.1.4. Conclusions

We have reported on the synthesis and characterization of three nematic liquid crystal polyesters containing α -methylstilbene moieties in the main chains and aliphatic or aromatic spacers. Their structure and molecular weights were characterized by means of NMR spectroscopy and SEC-LS. XRD, POM and DSC analyses showed that admixtures of various chlorides had a significant impact on the behaviour of the polymers, reducing their crystallinity, or even suppressing it completely, and decreasing the values of T_g . In all cases we observed some changes in polymer structure around 200 °C, which seemed to be due to

Chapter 1

crosslinking of the vinyl bond, as shown by FTIR spectroscopy. These polymers exhibit E–Z photoisomerization, as evident from UV and NMR spectra obtained after UV irradiation at 364 nm. Photoisomerization kinetics was also studied at 20 °C in CDCl₃ using ¹H NMR analysis and it was found to be of first order, with constants of the order of 10⁻⁴ s⁻¹. A dense membrane based on polymer P2 was also prepared by casting and it showed an increase of wettability upon photoirradiation. These polymers could therefore be candidates to constitute the shell of photoactive microcapsules for light-triggered release.

1.1.5. Acknowledgements

Financial support from MAT2008-00456/MAT (Ministerio de Ciencia e Innovación) is gratefully acknowledged. The authors are also grateful to LLP/ERASMUS Program between Universitat Rovira i Virgili and Adam Mickiewicz University. The authors are also grateful to Dr Renata Jastrzab for her help in calculations of dipole moments.

1.1.6. Supporting Information

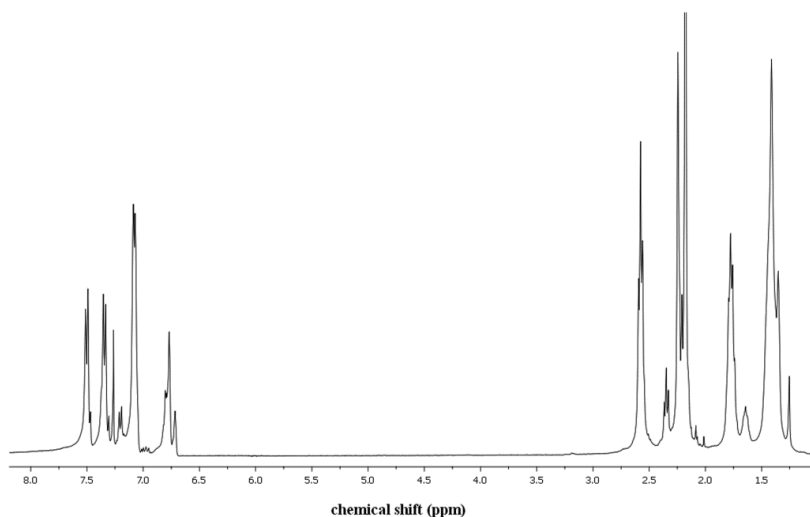


Figure S1.1.1. ¹H NMR spectrum in CDCl₃ of P1

Chapter 1

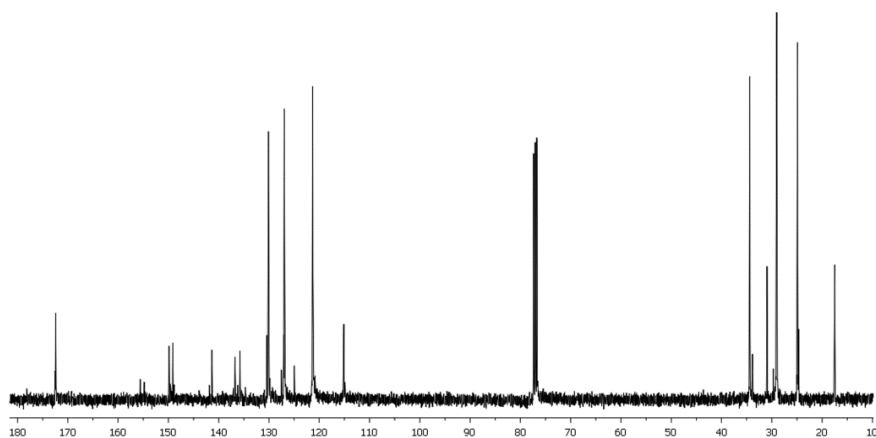


Figure S1.1.2. ^{13}C NMR spectrum in CDCl_3 of P1.

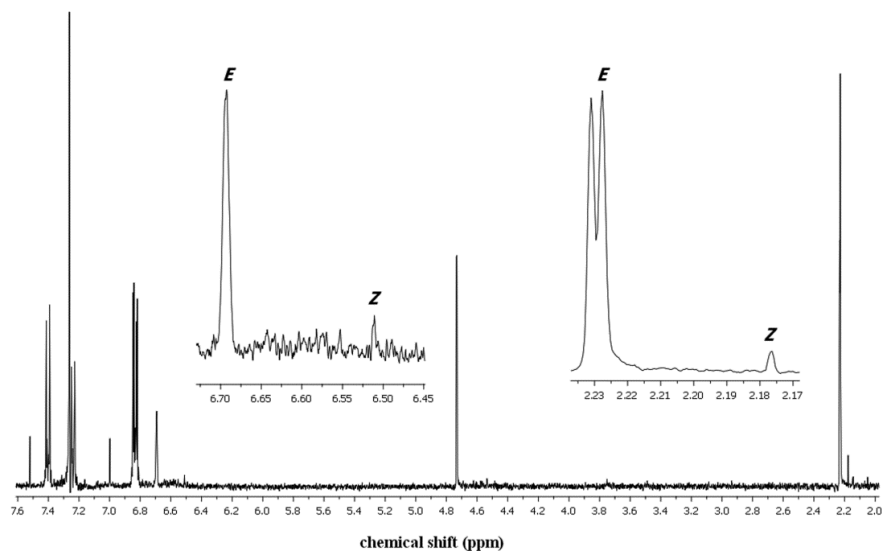


Figure S1.1.3 ^1H NMR spectrum in CDCl_3 of α -methylstilbene. The insets show a magnification of vinyl (6.45- 6.75 ppm) and methylic (2.17-2.24 ppm) protons regions.

Chapter 1

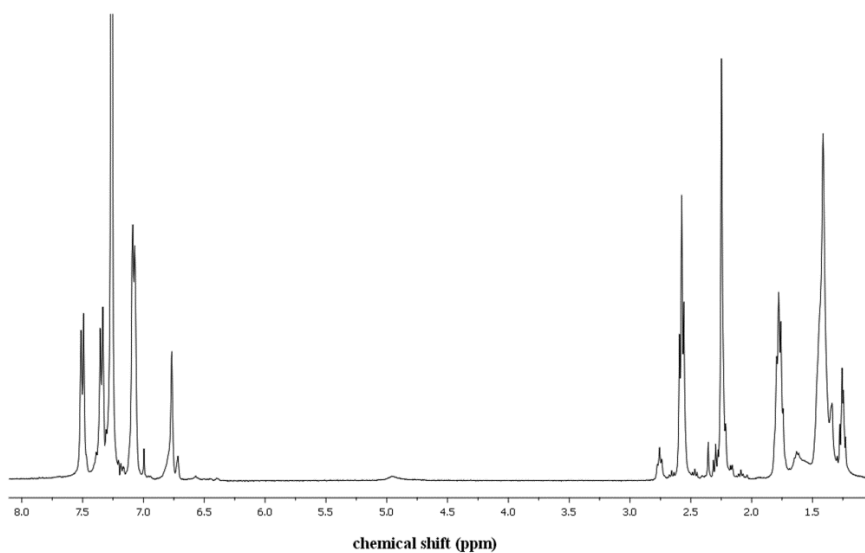


Figure S1.1.4. ^1H NMR spectrum in CDCl_3 of P3.

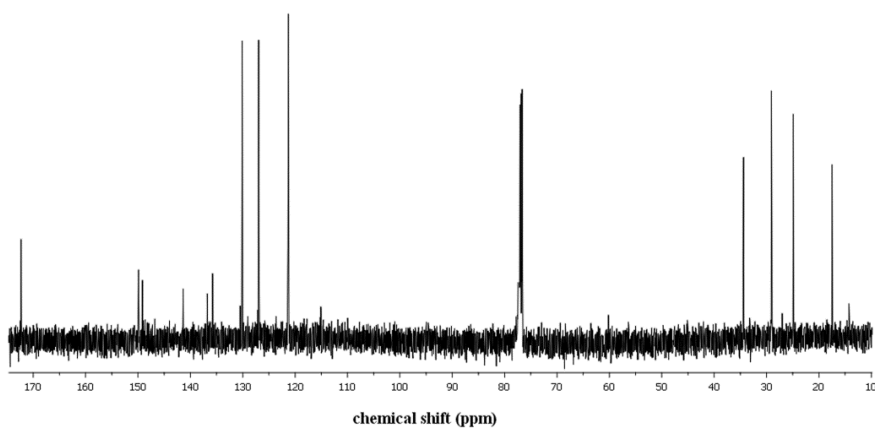


Figure S1.1.5. ^{13}C NMR spectrum in CDCl_3 of P3.

Chapter 1

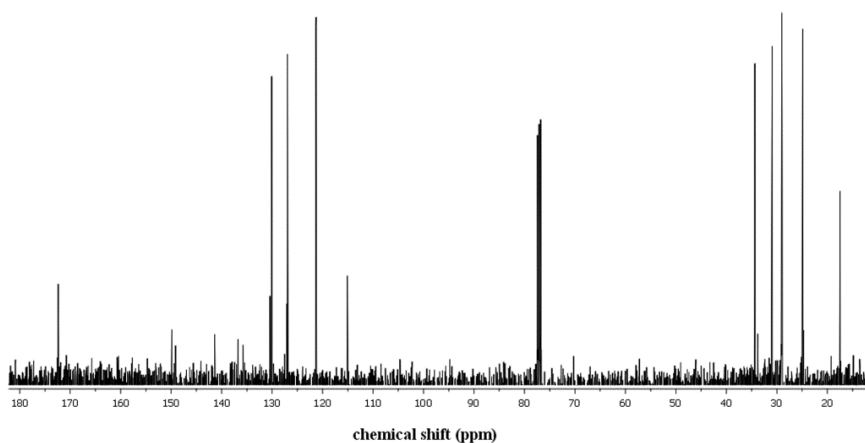


Figure S1.1.6. ^{13}C NMR spectrum in CDCl_3 of P4.

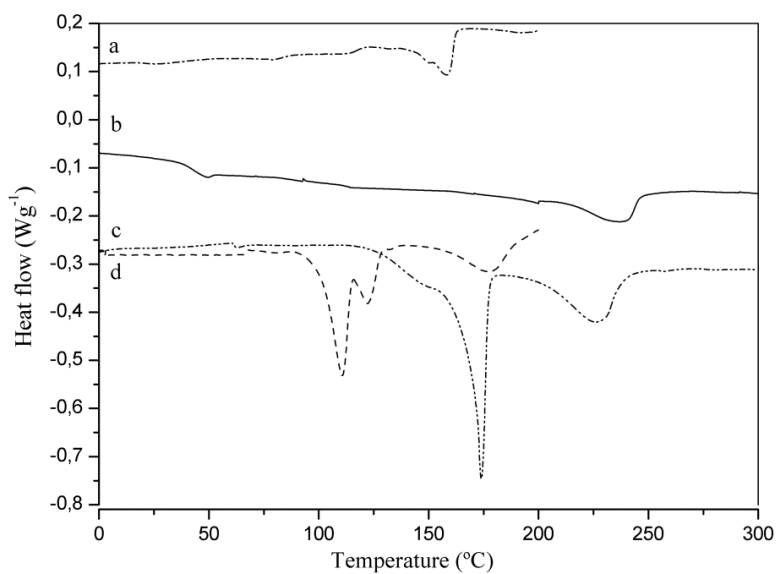


Figure S1.1.7. DSC thermograms of: (a) P3, second heating scan; (b) P4, first heating scan; (c) P2, first heating scan; (d) P1, second heating scan. Scan rate: $10^\circ\text{C}/\text{min}$.

Chapter 1

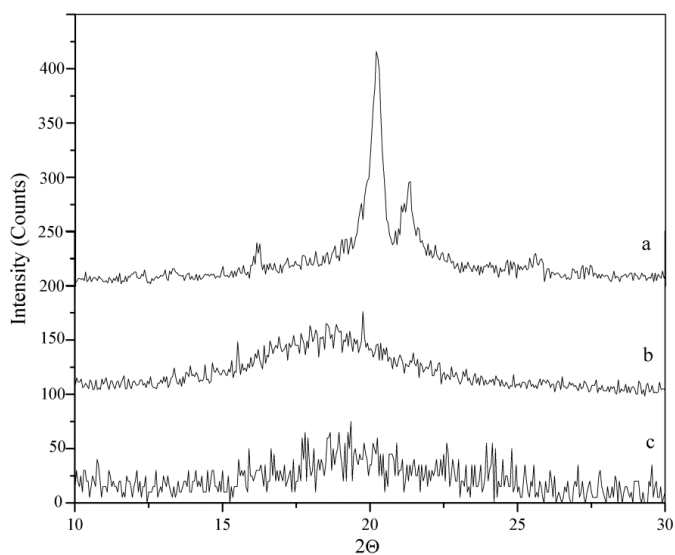


Figure S1.1.8. XRD pattern of: (a) P2, 30°C; (b) P2, 180°C; (c) P4, 30°C.

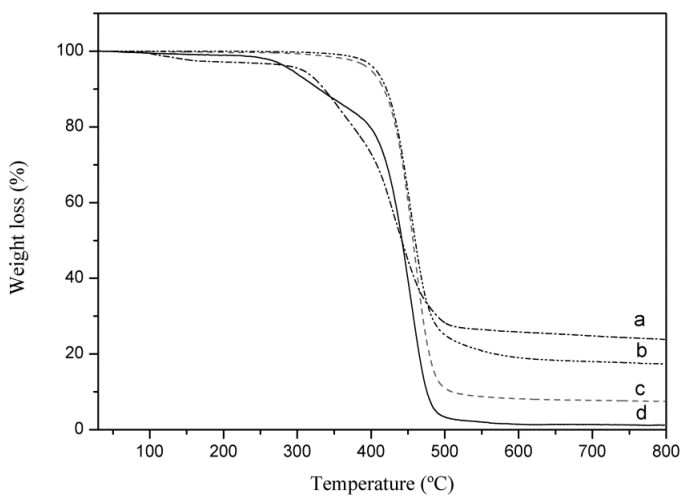


Figure S1.1.9. Thermogravimetric analysis in nitrogen of: (a) P3; (b) P4; (c) P2; (d) P1.

Chapter 1

1.1.7. References

- (1) Esser-Kahn A.P., Odom S.A., Sottos N.R., White S.R., Moore J.S., *Macromolecules*, 2011, 44, 5539-5553.
- (2) Li C., Cheng F., Lv J., Zhao Y., Liu M., Jiang L., Yu Y., *Soft Matter*, 2012, 8, 3730–3733.
- (3) Li L., Xing X., Liu Z., *Journal of Applied Polymer Science*, 2012, 124, 1128–1136.
- (4) Joseph G., Pichardo J., Chen G., *Analyst*, 2010, 135, 2303–2308.
- (5) Nakahara Y., Okazaki Y., Kimura K., *Soft Matter*, 2012, 8, 3192–3199.
- (6) Nishi H., Namari T., Kobatake S., *Journal of Material Chemistry*, 2011, 21, 17249–17258.
- (7) Yagai S., Ohta K., Gushiken M., Iwai K., Asano A., Seki S. Kikkawa ikkawa ., Morimoto M., Kitamura A., Karatsu T., *Chemistry- a European Journal*, 2012, 18, 2244–2253.
- (8) Tylkowski B., Pregowska M., Jamowska E., Garcia-Valls R., Giamberini M., *European Polymer Journal*, 2009, 45, 1420–1432.
- (9) Giamberini M., Amendola E., Carfagna C., *Macromolecular Rapid Communications*, 1995, 16, 97–105.
- (10) Carfagna C, Amendola E and Giamberini M, *Prog Polym Sci* 22:1607–1647 (1997).
- (11) Malkin A., Wood J., Ross D.L., Blanc J., In *Photochromism Techniques of Chemistry*, ed. by Brown G.H., Wiley-Interscience, 1971, p. 471.
- (12) Altomare A., Carlini C., Ciardelli F., Panattoni M., Solaro R., Houben J.L., *Macromolecules* 1985, 18, 729–734.
- (13) Giménez R., Piñol M., Serrano J.L., Viñuales A.I., Rosenhauer R., Stumpe J., *Polymer*, 2006, 47, 5707–5714.
- (14) Ding L., Russell T.P., *Macromolecules*, 2006, 39, 6776–6780.
- (15) Lowry T.H., Richardson K.S., *Mechanism and Theory in Organic Chemistry*. Harper and Row, 1987.

Chapter 1

- (16) Rameshbabu K., Kannan P., *Polymer International*, 2006, 55, 151–157.
- (17) Jegal J., Blumstein A., *Journal of Applied Polymer Science*, 1998, 68, 387–393.
- (18) Lederer A., Voigt D., Appelhans D., Voit B., *Polymer Bulletin*, 2006, 57, 329–340.
- (19) Tylkowski B., Trusheva B., Bankova V., Giamberini M., Peev G., Nikolova A., *Journal of Membrane Science*, 2010, 348, 124–130.
- (20) Jastrzab R., *Journal of Coordination Chemistry*, 2013, 66, 98–113.
- (21) Lin C.-K., Kuo J.-F., Chen C.-Y., *European Polymer Journal*, 2001, 37, 303–313.
- (22) Ogasawara S., Saito I., Maeda M., *Tetrahedron Letters*, 2008, 49, 2479–2482.
- (23) Hikmet R.A.M., Zwerver B.H., Lub J., *Macromolecules*, 1994, 27, 6722–6727.
- (24) Hahn S.K., Lee S.W., Lee T.J., Cho S.A., Chae B., Jung Y.M., et al. *Journal of Physical Chemistry*, 2008, 112, 4900–4912.
- (25) Hunter D.H., Cram D.J., *Journal of American Chemical Society*, 1964, 86, 5478–5490.
- (26) Gegiou D., Muszkat K.A., Fischer E., *Journal of American Chemical Society*, 1968, 90, 12–18.
- (27) Eisenbach C.D., *Polymer Bulletin*, 1980, 2, 169–176.
- (28) Klaysom C., Moon S.-H., Ladewig B.P., Lu G.Q.M., Wang L., *Journal of Membrane Science*, 2011, 371, 37–44.
- (29) Ryan B.J., Poduska K.M., *American Journal of Physics*, 2008, 76, 1074–1077.

Chapter 2

Preparation and Characterization of Light-Sensitive Microcapsules based on a Liquid Crystalline Polyester

Krzysztof Artur Bogdanowicz, Bartosz Tylkowski and Marta Giamberini*

*- *Langmuir* **2013**, 29, 1601–1608

UNIVERSITAT ROVIRA I VIRGILI
LIQUID CRYSTALLINE POLYMERS FOR SMART APPLICATIONS.
Krzysztof Artur Bogdanowicz
Dipòsit Legal: T 1677-2015

Chapter 2

1. Introduction

Stilbene and azobenzene are typical photochromic molecules that have been used by many researchers to introduce photoresponsive properties into materials: their *E-Z* photoisomerization produces a variety of changes in physicochemical properties of the materials, such as molecular length and polarity. The introduction of stilbene or azobenzene groups to polymers leads to fascinating photoresponsive systems.¹⁻⁵

Microencapsulation was first introduced in the 1950s by Green and Schleicher.⁶ Microcapsules can encapsulate various kind of substances, such as gases, liquids, and solids; coating substances can also be selected from a wide variety of natural or synthetic polymers, depending on the substance to be coated and on the desired characteristics of the final microcapsules. By properly selecting the core material and the membrane, which constitutes the shell, it is possible to prepare microcapsules with a variety of functions. Many core materials have been encapsulated, including adhesives and coatings,⁷ food additives,⁸ catalysts,⁹ dyes,¹⁰ and drugs.¹¹ Microcapsules can release their contents in response to a stimulus such as mechanical damage¹² or temperature, pH, ionic strength, electric field, and magnetic flux.¹³ Nowadays microencapsulation technology is promising for new applications in the fields of intelligent microstructures and microsystems, as well as in the field of phase-change materials and in self-healing composites. In order to develop new and versatile applications of microcapsules, their synthesis and characterization has been researched extensively. The possibility of triggering release by light irradiation has been of particular interest: for application in agricultural and cosmetic field, UV and visible light-sensitive microcapsules are desirable, while near-IR absorbing capsules are more adequate for applications related to biological systems. In general, microcapsules can be made sensitive to light by incorporation of light-sensitive polymers, functional dyes, and metal nanoparticles.^{14,15} Quite recently, nanoengineered polymeric capsules were modified by the incorporation of Bacteriorhodopsin into their shell: these molecules acted as a light-driven proton pump, which in turn determined a pH change which could open the pores and modify shell permeability.¹⁶

In a previous paper,¹⁷ we synthesized by interfacial polymerization microcapsules based on a liquid crystalline polyamide, whose state of order could be changed upon the application of external stimuli such as temperature and light. Release experiments performed in water at 20 °C on polyamide microcapsules containing β -carotene,

Chapter 2

showed that release could be triggered by photoisomerization: in the absence of irradiation, release reached a plateau value of about 2.5% after a few minutes, while, when microcapsules were submitted to continuous irradiation with UV light, β -carotene was quickly released and reached 100% release after five minutes.

In the present work, our aim was to obtain microcapsules whose properties could be modulated by means of external stimuli such as light. We make the hypothesis that phototriggered release from such microcapsules occurs as a consequence of *E-Z* photoisomerization of α -methylstilbene moieties in the polymer backbone, which forms a microcapsule shell during UV irradiation. Photoresponsive microcapsules were prepared using poly(α -methylstilbenesebacate-co- α -methylstilbeneisophthalate) (P4). P4 is a novel nematic liquid-crystalline polymer of our synthesis with a glass transition of 45 °C and clearing point of 238 °C. This polymer possesses an amorphous structure and a reasonably low glass transition value thanks to the incorporation of isophthaloyl moieties in the polymer backbone. Before preparing and characterizing microcapsules, we performed an exhaustive characterization of a membrane based on the P4 polymer obtained by using conditions as similar as possible to microcapsule preparation. In this way, we tried to simulate the morphology and the behaviour of the microcapsule shell under UV irradiation.

1.2.2. Experimental Section

Materials

Vanillin (ACROS, 99%) was used as received without any further purification. All the solvents were supplied by Scharlau and used without previous purification as received. Poly(α -methylstilbenesebacate-co- α -methylstilbeneisophthalate) (P4) was synthesized in our laboratory, as described in the Supporting Information. Its structure is reported in Figure 1.2.1.

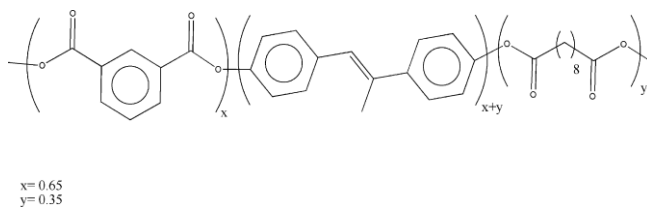


Figure 1.2.1. Structure of poly(α -methylstilbenesebacate-co- α -methylstilbeneisophthalate).

Chapter 2

Membrane Preparation

Membranes were prepared by a phase-inversion precipitation (PIP) process, in which a homogeneous polymer solution is cast on a suitable support and immersed in a coagulation bath containing a nonsolvent. Precipitation occurs due to exchange of solvent and nonsolvent molecules in contact with the polymer. In order to prepare photoresponsive membranes, the P4 polymer was dissolved in chloroform by stirring for several hours to obtain a 2.5 wt % homogeneous solution. Next, the solution was cast on a glass plate by means of a custom-made casting knife (gap 60 μm). Then, the cast films were coagulated in a bath containing methanol as a nonsolvent for at least 1 h. Afterward, the films were released themselves from the glass plates, dried, and kept in a dark box.

Microcapsules Preparation

Microcapsules based on poly(α -methylstilbenesebacate-co- α -methylstilbeneisophthalate), containing chloroform or chloroform/vanillin as a filler, respectively, were prepared by a PIP process like the P4 membranes. P4 and P4/vanillin microcapsules were obtained by using a nozzle device working in a semicontinuous process with a nozzle size of 70 μm (Spraying Systems Company, dispersion combination type SUF1). The apparatus was developed and adjusted specifically for the production of microcapsules. A similar apparatus with a nozzle size of 80 μm was used by Peña et al.¹⁸ for polysulfone/vanillin microcapsules preparation. With the nozzle device used in this investigation, it is possible to obtain a high production of microdroplets in one-step. The nozzle was connected to a compressed air supply valve that offered the energy required to break up the polymeric solution into microdroplets. When the air valve was opened, the device dispersed the polymeric solution by shearing action provided by a high-velocity air stream (around 500 l/h). The nozzle was located 25 cm (distance to methanol surface) over a container with methanol. The outlet flow was positioned perpendicular to the surface of the coagulation bath. Thus, the microdroplets impacted directly on the methanol surface. Figure 1.2.2 shows a scheme of the dispersion setup. The polymeric solutions (2.5 wt % of P4 in chloroform or 2.5 wt % of P4 in chloroform containing 10 wt % of vanillin) were first prepared in dark bottles to ensure that the α -methylstilbene moieties were in *E*-configuration and then poured into the nozzle bulk just before the capsules production, in order to avoid contact with the atmospheric air that can induce solvent evaporation. As the precipitation of the polymer in contact with the methanol is very fast, the coagulation bath was stirred to

Chapter 2

prevent microcapsule aggregation (magnetic stirrer set up at 100 rpm). After precipitation, the microcapsules were decanted, dried in a desiccator, and stored in a dark bottle.

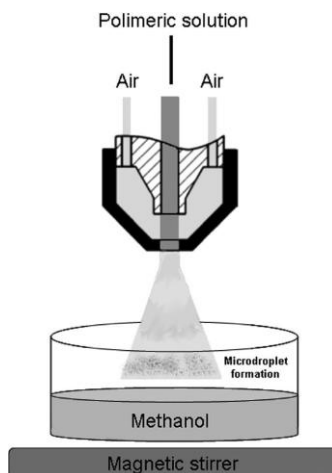


Figure 1.2.2. Schematic diagram of the atomization setup.

Characterization

Sample irradiation was carried out with a VI- 4.LC UV Vilber Lourmat lamp (230 V, 8 W) at 365 nm. The temperature of the membranes during UV irradiation was monitored at three different points by means of a type-K thermocouple.

Surface and cross-section morphology of membranes and microcapsules were investigated by means of a high vacuum ESEM FEI Quanta 600 apparatus, after previous gold metallization. Membrane cross sections were prepared by fracturing in liquid nitrogen. In order to obtain microcapsules cross-section micrographs without modifying their structure, they were cryogenically cut.¹⁹ For this procedure, a cryostat Leica CM 1850 was used. First microcapsules were attached over a specimen disc with a freezing medium. An embedding medium for frozen tissue specimens was used (Tissue-Tek, OCT Compound, Sakura Tissue). Once the capsules were fixed over the specimen disc, the disc was immersed into a liquid nitrogen bath in order to freeze the sample. Next, the specimen disc was located in the cryochamber. Then, the sample was cut with thickness intervals of 1 μm at $-20\text{ }^{\circ}\text{C}$ and deposited

Chapter 2

over a glass. Finally, the cross sections were analyzed by high-vacuum ESEM.

The membrane thickness was measured during ESEM analysis by xT microscope control connected with an ESEM FEI Quanta 600 apparatus. The average thickness of the membrane (10 measures) was calculated from cross-section ESEM micrographs with Image-ProPlus 5 software (Media Cybernetics Inc.).^{20,21}

Membrane and microcapsules cross-section porosities were calculated by means of IFME software²² from cross-section ESEM micrographs.

Microcapsules average size was calculated by analyzing the ESEM micrographs by Image-ProPlus 5 software. The sizes of 245 microcapsules containing chloroform as a core and 167 microcapsules containing a concentrated solution of vanillin, respectively, were measured and were considered as 100%. In order to graphically present the microcapsules characteristic size distribution, microcapsules sizes were grouped in 11 intervals with a 5 mm width.

The changes in membrane surface morphology before and after UV irradiation were detected by atomic force microscopy (AFM). The AFM images were recorded with an Agilent 5500 Environmental Atomic Force Microscope (Agilent Technology) equipped with an extender electronics module, which enables phase imaging in Tapping Mode. All the images were recorded in tapping mode using Multi 75 (BudgetSensors) silicon cantilevers (length = 225 μm , width = 28 μm , and thickness = 3 μm) with a force constant of 3 N/m and a resonance frequency of 75 kHz. The scan rate was typically 0.7–2 Hz. All images (10 \times 10 μm) were measured at room temperature, in air without filtering. The microscope was placed on an active vibration isolation chamber (Agilent Technology), which was further placed on a massive table to eliminate external vibration noise. The Nanotec WSxM 5.0 Develop 4.0 Image Browser Scanning Probe Microscopy²³ was used for the roughness analysis of the images.

Contact angles of water drops on a membrane surface were measured with a Kruss contact angle instrument (Hamburg, Germany) equipped with a motorized pipet (Matrix Technology, Nashua, NH) and deionized water as the probe liquid. The contact angle was measured immediately after putting the water drop (3 μm) on the membrane surface. Measurements were repeated using different areas of the film. For each test reported, at least three drops of water were used.

Chapter 2

Dipole moments were calculated with GAUSSIAN 03 (Ground State DFT and B3LYP/Set lanL2DZ level).²⁴ Structures, preoptimized semiempirically with HYPERCHEM-7.52 (PM3 Hamiltonian) were used as starting points. Molecular lengths of E- and Z- α -methylstilbene were estimated from the molecular model created using CS Chem3D Ultra 8.0 (Cambridge-soft, Cambridge, MA).¹³

Release experiments of vanillin from microcapsules were performed in 100 mL milli-Q water medium with and without UV irradiation. The same amount of microcapsules (4.2 mg) was immersed into two separated conical flasks, A and B, which were stirred at a constant temperature of 20 °C. In the case of flask A, 3mL samples were collected periodically every 5 min for 30 min and filtered by a Nitrocelulose Millipore Corporation's filter (pore size, 0.22 μ m). In the case of flask B, the microcapsule suspension was continuously irradiated with UV light at 364 nm and samples (3 mL) were collected periodically and filtered as previously described. The collected samples were transferred back into the conical flasks after the analysis. The vanillin amount was determined by measuring the absorbance of the samples at 316 nm by means of a Dinko instrument 8500 spectrophotometer; the concentration of vanillin was obtained by interpolation of a calibration curve, according to the Lambert-Beer law. Chloroform was also irradiated with UV light at 364 nm, in order to confirm that the peak at 316 nm is not altered as a consequence of chloroform irradiation and can be used to determine vanillin content also in the presence of this solvent. Release was calculated as A_t/A_∞ , where A_t is the absorbance at 316 nm at time t , and A_∞ is the highest value of absorbance, corresponding to the release curve plateau.

1.2.3. Results and discussion

Membrane Preparation and Characterization

As already stated before, our aim was to obtain photoactive microcapsules based on poly(α -methylstilbenesebacoate-co- α -methylstilbeneisophthalate). In order to establish whether the microcapsule shell morphology and behaviour could be altered as an effect of photoirradiation, we decided to perform first an exhaustive characterization of a flat membrane based on the P4 polymer, prepared by phase inversion as described in Experimental Section. This methodology is quite similar to the one used for microcapsules. Therefore, similar morphology to the microcapsule shell can be expected.

Chapter 2

Environmental scanning electron microscopy (ESEM) was used to observe the morphology both of P4 membranes and microcapsules.

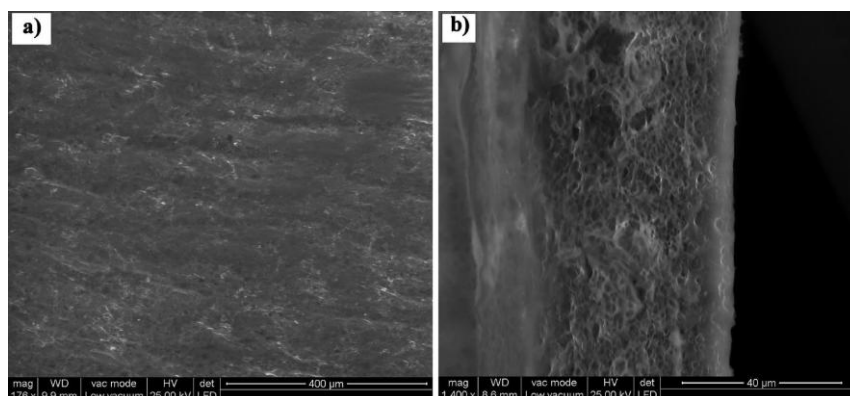


Figure 1.2.3. ESEM micrographs of the (a) surface and (b) cross-section of the P4 membrane.

Figure 1.2.3a shows the results of ESEM observation of the P4 membrane surface, while Figure 1.2.3b shows its cross-section morphology. This membrane is asymmetric since it consists of a dense skin layer and a spongylike porous support sublayer structure. Membrane thickness calculated by Image-ProPlus 5 software and ESEM micrographs gave the value of $56 \pm 2 \mu\text{m}$. The pore mean size of the membrane, as well as its asymmetry, yielded values of $0.46 \pm 0.03 \mu\text{m}$ and 12%, respectively. It is well-known that, in a phase separation process, liquid–liquid demixing and polymer–liquid demixing in a polymer/solvent/ nonsolvent system play very important roles in determining the membrane structure.²⁵ Niwa et al.²⁶ reported that the liquid–liquid exchange rate between the solvent and the nonsolvent has a great influence on the skin layer thickness and the membrane structure. Asymmetric membranes formed by delayed demixing possess a dense skin layer supported by a sponge-type structure, while the membranes formed by instantaneous demixing exhibit an ultrathin top skin layer supported by a finger-type structure. The delay time is on the order of one second or less for rapid demixing conditions, while for delayed demixing the precipitation time is on the order of seconds to minutes.²⁷ By using a similar chloroform/methanol system and polylactides (PLLA), quite similar spongylike membranes morphologies were observed by van de Witte et al.²⁸ In accordance with the authors, casting solutions with low PLLA concentrations gave membranes with a cellular morphology due to

Chapter 2

liquid–liquid demixing, followed by nucleation and growth of a polymer-poor phase. In our case, the formation of membranes consisting of a dense skin layer supported by a sponge-type structure indicates a liquid–liquid demixing process during PIP.

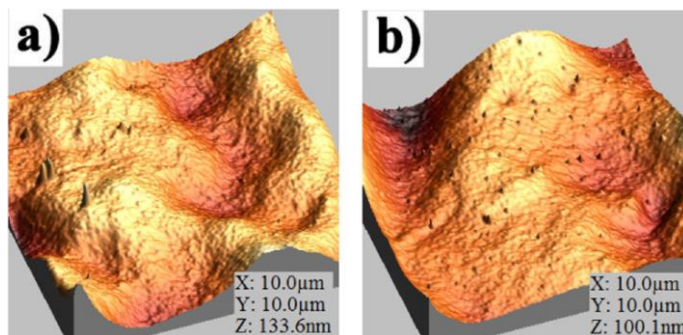


Figure 1.2.4. AFM images of P4 membrane (a) before and (b) after 30 min of irradiation with UV light at 365 nm.

Morphological changes of the P4 membrane caused by its exposure to UV light were investigated by atomic force microscopy (AFM). Figure 1.2.4 shows a three-dimensional topographical AFM image of a P4 film, before and after 30 min of irradiation with a UV lamp at 365 nm at room temperature. It can be observed that before irradiation (Figure 1.2.4a), there was a number of valleys on the membrane surface; when the film was irradiated with UV light, the morphology changed drastically, as it is shown in Figure 1.2.4b since the film surface looked less rough. The membrane temperature was monitored during the photoirradiation experiment, and it was found to vary as much as 1 ± 0.1 °C.

Table 1.2.1. Values of Standardized Roughness Parameters for P4 Membrane from AFM Analysis

Symbol	Name	Before photoirradiation with UV light (nm)	After photoirradiation with UV light (nm)
rms	roughness	16.49±0.25	12.51±0.18
S _{sk}	surface skewness	-0.130±0.0002	0.250±0.003
S _{ku}	surface kurtosis	2.79±0.031	4.40±0.05

Chapter 2

A quantitative characterization of P4 surface properties was performed by means of a set of standardized roughness parameters,²⁹ which are listed in Table 1.2.1. These values are averages calculated from several images acquired in different regions of the membrane. From Table 1.2.1, one can observe that the root mean square (rms) roughness, considered as a standard deviation of height, decreased about 24% after photoirradiation. The surface skewness (S_{sk}), which depicts the asymmetry of the height distribution, changed from a negative value, before UV irradiation, to a positive one, after UV irradiation. The former value refers to a surface-porous sample in which the valleys dominate over the peak regimes,^{29,30} while the latter indicates lack of surface porosity.³¹ Furthermore, surface kurtosis (S_{ku}), whose value illustrates the sharpness of the surface height distribution, turned from about 2.8 to 4.4 upon photoirradiation. S_{ku} values smaller than 3.0 generally indicate a broad (heterogeneous) height distribution, whereas values much larger than 3.0 refer to a surface with almost quantized height values. The average height of the film was found as 133.6 nm before and 100.1 nm after UV irradiation (see Figure 1.2.4). Therefore, AFM results confirmed smoothing of the membrane surface after UV irradiation.

The smoothing of the P4 film surface can be related to α -methylstilbene moieties photoisomerisation. As it is illustrated in Figure 1.2.5, before UV irradiation, α -methylstilbene moieties in the film are in the *E* form with a molecular length of 9.1 Å, according to our calculations; after UV irradiation, they convert into *Z* isomers and their length is reduced to 6.8 Å. We suggest that this ca. 25% decrease of the α -methylstilbene moiety lengths leads to substantial modification and smoothing of film morphology, in response to the contraction of the polymer main chain.

We also investigated whether the wetting properties of the P4 membrane could be changed upon UV irradiation by measuring the contact angles (CA, Figure 1.2.6). CA with water of a flat P4 film resulted $120 \pm 2^\circ$. After exposure to UV light (365 nm) for 30 min, the CA was found to be $95 \pm 2^\circ$, that is, it was decreased about 25° . The enhanced wettability can be related to the decrease of the surface roughness on photoisomerisation. As a matter of fact, it was shown³² that the value of CA for a droplet on a surface with a negative wetting tendency, such as the hydrophobic P4 membrane under investigation, decreases on decreasing surface roughness: if a smooth surface is water-repelling, the roughened surface will be more strongly so. Moreover, according to our calculations, in the *E* state, α -methylstilbene moieties have a smaller

Chapter 2

dipole moment (0.27 D), while *E*-to-*Z* isomerisation induced by UV-light irradiation leads to a large increase in the dipole moment of this molecule (0.56 D).

Thermal back isomerisation does not readily occur for stilbenes,³³ however, UV light at 254 nm was used to induce *Z*-*E* photoisomerisation of stilbene-based compounds.³⁴ Hikmet et al.³⁵ also investigated the stability of *E* and *Z* forms of stilbene moieties incorporated in anisotropic networks: according to them, the *Z* form is stable at room temperature over 3 months. Therefore, we tried to induce back-photoisomerisation of the irradiated P4 membrane by additional exposure to UV light at 254 nm at room temperature for 1 h. Actually, after this treatment, the CA value was not restored to its initial value, as shown in Figure 1.2.6. This suggests nonreversibility of *E*-*Z* photoisomerization of the P4 α -methylstilbene moieties in solid state at room temperature for the short times investigated.

Microcapsule Characterization

Figure 1.2.7a shows the ESEM image of microcapsules prepared by the previously described phase-inversion process, with pure chloroform as a filler, deposited on a Teflon filter and dried at room temperature. Microcapsules appear separated, well-formed, and globe-shaped. Figure 1.2.7b shows the ESEM micrograph

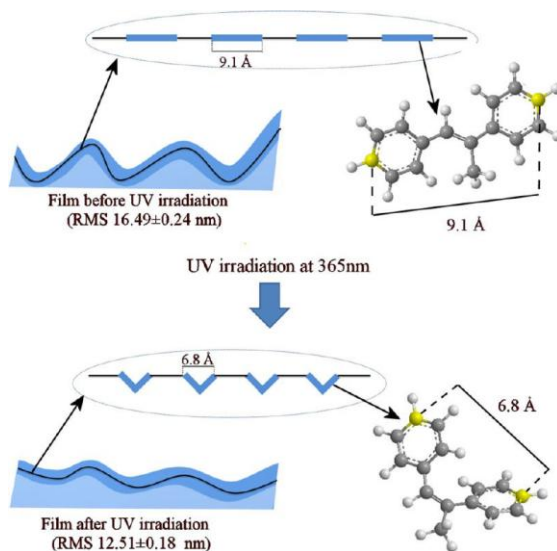


Figure 1.2.5. Model of the structural change of the P4 film, containing α -methylstilbene moieties in the main chain, induced by photoisomerization.

Chapter 2



Figure 1.2.6. Wettability changes of the P4 membrane (a) before irradiation, (b) after UV irradiation at 365 nm, and (c) after UV irradiation at 365 nm followed by additional irradiation at 245 nm.

of one of the microcapsules after cryogenically cutting, while Figure 1.2.7c shows the detail of the fractured cross section. Despite the slight differences in film and microcapsule preparations, which could induce different morphologies, the outer microcapsule surface appears smooth and dense, while the cross-section morphology possesses a spongylike structure with 12% asymmetry, similar to the P4 film. Pore mean size were calculated by means of IFME software and yielded values of $0.02 \pm 0.01 \mu\text{m}$.

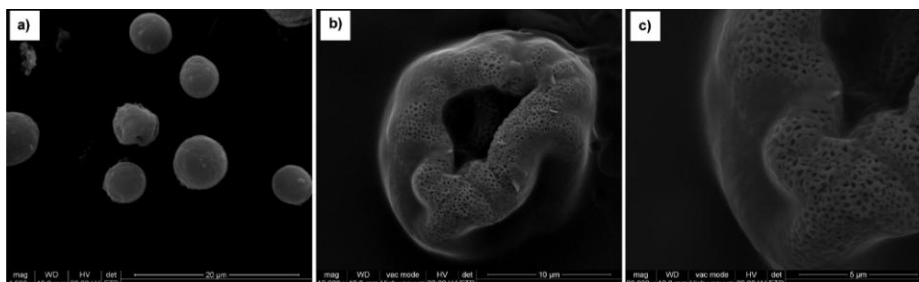


Figure 1.2.7. ESEM micrographs of (a) microcapsules containing chloroform as a filler, (b) a single microcapsule after cryogenically cutting, and (c) details of the fractured cross section.

Chapter 2

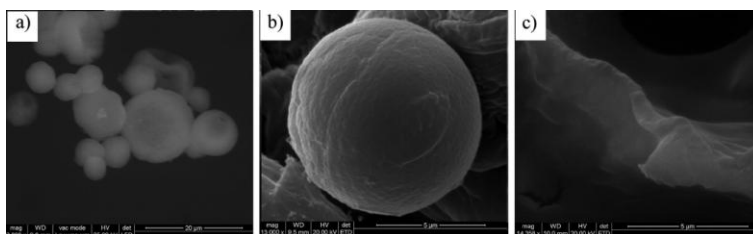


Figure 1.2.8. ESEM micrographs of (a) microcapsules containing vanillin in chloroform as filler, (b) a single microcapsule, and (c) detail of the fractured cross section after cryogenically cutting.

By means of Image-ProPlus 5, we could analyze ESEM micrographs and obtain the characteristic distribution of the capsule diameter, which is shown in Figure S1.2.1 of the Supporting Information. This showed that the P4/chloroform microcapsules had diameters in the range of $3\text{--}55 \pm 2 \mu\text{m}$; the mean diameter was $12 \pm 2 \mu\text{m}$, and 90% of the capsules diameters lay in the range of $3\text{--}25 \pm 2 \mu\text{m}$. Wall thickness was measured from images of 5 fractured microcapsules and gave a value of about $1.80 \pm 0.17 \mu\text{m}$. It is noteworthy that the ratio wall thickness/pore mean size both of P4 membranes and microcapsules gave approximately the same value (i.e., 1%).

In order to check whether the release could be triggered by photoirradiation, we also prepared microcapsules containing vanillin, by using a concentrated solution of vanillin (167 g/L) in chloroform and the same precipitation conditions described in the experimental part. Vanillin is widely used as a flavouring additive and as a preservative in the food industry, due to its antioxidant and antimicrobial properties; moreover, it is used as a fragrance constituent in the cosmetics and textile industries.^{36,37} Its amount can be determined in a relatively simple way (e.g., by UV-vis spectroscopy).

Figure 1.2.8 shows the ESEM image of (a) microcapsules containing vanillin dissolved in chloroform, (b) a single microcapsule, and (c) details of the fractured surface after cryogenically cutting. In this case, the microcapsule outer surface morphology looked very similar to the one obtained with pure chloroform as filler. However, the shell thickness measured from ESEM resulted in $0.19 \pm 0.06 \mu\text{m}$, and it was approximately 10 times lower than one of the capsules without vanillin; moreover, their cross-section morphology appeared smooth and dense, and it was completely different from the capsules containing pure chloroform. This evidence can be related to the presence of vanillin in

Chapter 2

chloroform, which is a solvent in the phase-inversion method. Peña et al. prepared (via the PIP technique) and characterized both polysulfone (PSf)/vanillin microcapsules³⁸ and PSf/vanillin films.³⁹ These authors found that PSf/vanillin systems exhibit less pores than neat PSf-based ones. By NMR techniques, they could also establish that vanillin has a high tendency to be trapped in the microcapsule polymeric shell, probably during capsule formation. On the basis of their studies, the authors concluded that the original morphology of the shell is altered as a consequence of vanillin inclusion in polysulfone. Inclusion of vanillin in the P4-based shell could be the reason for the morphological differences found also in our case.

In this case, the characteristic distribution of the capsule diameters, which is shown in Figure S1.2.2 of the Supporting Information, gave the same mean diameter of $12 \pm 2 \mu\text{m}$ as the microcapsules containing pure chloroform, with 90% of capsule diameters ranging between 3 and $20 \pm 2 \mu\text{m}$. Figure 1.1.9 shows the release of vanillin from P4 microcapsules in water at 20 °C, in the time range of 0–35 min, in the absence (■) and presence (◆) of continuous irradiation with UV light at 365 nm, measured as described in Experimental Section. The difference between the two curves is straightforward: in the absence of irradiation, release was practically negligible and the plateau value of about 8–10%, reached immediately after the UV lamp was switched on, remained constant, even after 1 h of observation. Differently, when microcapsules were submitted to continuous irradiation with UV light, after an induction period of about 20 min, vanillin was quickly released. It is important to stress that the initial time corresponds to the UV lamp switched to the on position. The 8% vanillin release during the first few seconds can be attributed to the amount of vanillin adsorbed on the outer surface of the microcapsule shell.

On the basis of the kinetic data for *E*–*Z* photoisomerization of the P4 polymer in CDCl_3 ,⁴⁰ it was calculated that in chloroform solution, just 18% of the *Z* form of P4 was achieved after ca. 20 min of UV irradiation. However, one should take into account that the mobility of P4 is expected to be considerably different when it is in the form of a microcapsule shell; moreover, one should consider that other factors, such as cooperative rearrangements of the polymeric chains induced by α -methylstilbene photoisomerisation, could be responsible for the overall change in the shell permeability. Once the polymer has changed its conformation and shell wettability has increased as a consequence of photoirradiation, water can easily penetrate the capsules and drive vanillin out.

Chapter 2

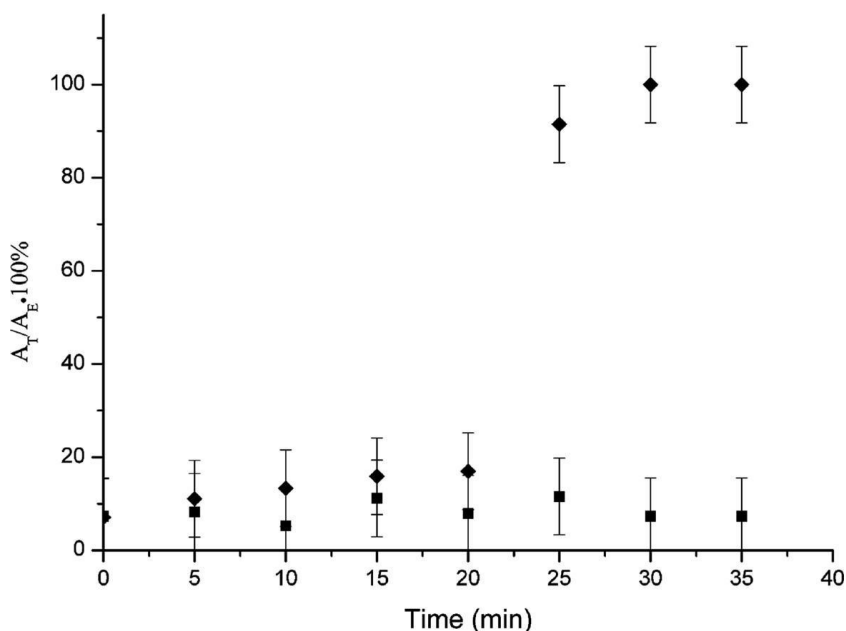


Figure 1.2.9. Vanillin release from P4 microcapsules in water at 20 °C, in the time range of 0–35 min, in the absence (■) and presence (◆) of continuous irradiation with UV light at 365 nm.

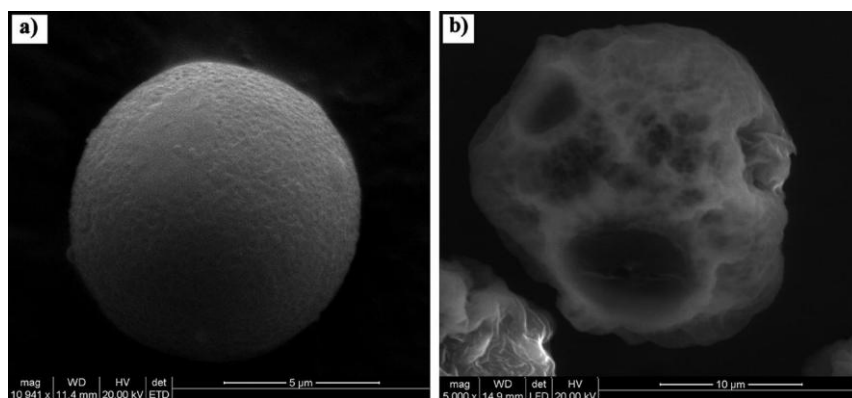


Figure 1.2.10. ESEM micrographs of a single microcapsule containing chloroform/vanillin after 30 min of release experiments at room temperature (a) without UV light and (b) accompanied by UV irradiation at 365 nm.

Chapter 2

Morphological changes of the P4 microcapsule shells, caused during release experiments by UV irradiation, were investigated by ESEM microscopy. Figure 1.2.10 shows the comparison of the morphology between microcapsules recovered after 30 min of vanillin release experiment in the absence (Figure 1.2.10a) and presence of UV irradiation at 365 nm (Figure 1.2.10b). Drastic differences between the images were encountered. Surface morphology of the unirradiated microcapsules looked very similar to the morphology of the microcapsule before release experiment, as shown in Figure 1.2.8b, while it changed drastically in the case of irradiated microcapsules, since they did not look well-formed and globe-shaped any more but concaved and riddled. These data suggest that phototriggered release from microcapsules occurred due to the P4 polymer backbone conformational changes.

1.2.4. Conclusions

Encapsulation technology is currently the best solution available on the market for the delivery of dedicated components/materials in different applications, such as food ingredients, perfumes, drugs, biomolecules, catalytically active molecules, dyes, or adhesives. The main aim of our research is to foster the discovery of breakthrough technologies for the controlled delivery of actives, in order to optimize and control their delivery and impact via determined release points, while minimizing the quantity of materials used for the expected purpose. So, we focused on the development and testing of new photocontrol release microcapsules.

In this paper, we prepared photoresponsive microcapsules, based on poly(α -methylstilbenesebacate-co- α -methylstilbeneisophthalate) (P4), containing different core materials, by using a phase-inversion precipitation process. In order to establish whether microcapsule shell morphology and behaviour could be altered as a consequence of photoirradiation, a complete characterization of a flat membrane based on P4 polymer was first carried out.

ESEM studies showed that P4 membrane and microcapsules containing chloroform as filler possessed very similar asymmetric cross-sectional morphologies. The presence of vanillin in chloroform during PIP process had an influence on the cross-sectional structure of microcapsules containing this perfume. However, the outer surface morphologies of all prepared microcapsules appeared like a dense film. On the basis of AFM investigations, it was seen that the P4 film morphology changed drastically as a consequence of its exposure to UV irradiation at 365 nm (i.e., its surface became much smoother and surface

Chapter 2

roughness was decreased ca. 24%). This reasonably induced about a 21% decrease of the water contact angle value.

Release experiments showed that vanillin release from microcapsules in water at room temperature was strongly influenced by UV irradiation: in the absence of irradiation, release was negligible, while, when microcapsules were submitted to continuous irradiation with UV light for 35 min, vanillin was quickly released after an induction time of about 20 min.

All the results obtained from exhaustive characterization of a flat membrane, as well as ESEM observation of microcapsule morphological changes during vanillin release under UV irradiation, suggest that phototriggered release occurs as a consequence of the P4 polymer backbone conformational changes induced by α -methylstilbene moiety *E-Z* isomerization.

The next step of our investigation will be focused on the design of new photoresponsive materials and microcapsules, whose properties could be modulated not only by UV light but also by means of visible light.

1.2.5. Acknowledgment

Financial support from MAT2008-00456/MAT (Ministerio de Ciencia e Innovación) is gratefully acknowledged. The authors are also grateful to Dr. Renata Jastrzab for her help in dipole moment calculation and to Mr. Alemayehu Paulos Washe for his help with contact-angle measurement.

1.2.6. Supporting Information

Synthesis of P4

Poly(α -methylstilbenesebacate-co- α -methylstilbeneisophthalate) (P4) was obtained by the conventional liquid-liquid phase transfer-catalyzed interfacial polyesterification. The ratio phenol group/chlorine was kept 1:1. In a typical preparation a solution of 4,4'-dihydroxy- α -methylstilbene (0.56 g, 2.5 mmol, in 10 mL of 0.5 M aqueous sodium hydroxide solution) were reacted for 72 hours with a solution of sebacyl chloride (0.42 g, 1.75 mmol) and isophthaloyl chloride (0.15 g, 0.75 mmol) in 16 mL 1,2-dichloroethane (molar ratio sebacyl/isophthaloyl 70/30) into a blender that contained 15.5 mL of ice-cold water, and benzyltriethyl ammonium chloride (0.18 g, 0.8 mmol) as a phase transfer catalyst. 0.74 g of pure

Chapter 2

polymer was obtained, which corresponded to 65% yield. The polymer was fully characterized by ^1H and ^{13}C NMR, as described in Tylkowski et al.⁴⁰ Size-Exclusion Chromatography-Laser Scattering gave the following results: $M_n=14.6 \times 10^3\text{g/mol}$; $M_w = 30.0 \times 10^3 \text{g/mol}$.

Calorimetric characterization by DSC: G 45 N 238 I

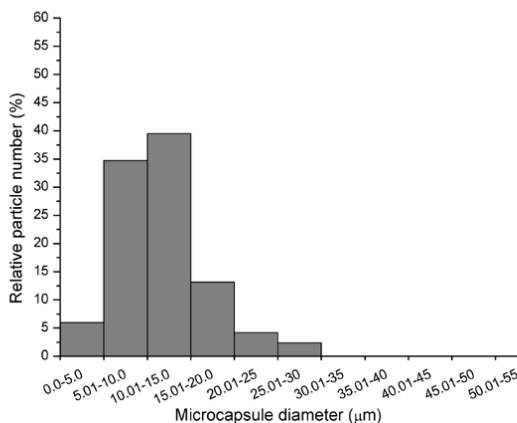


Figure S1.2.1. Characteristic size distribution, as measured on 245 microcapsules, of P4 capsules containing chloroform as a core.

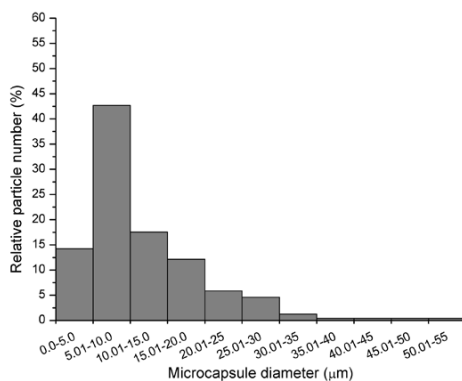


Figure S1.2.2. Characteristic size distribution, as measured on 167 microcapsules, of P4 capsules containing vanillin as a core.

Chapter 2

1.2.7. Reference

- (1) Tzeli D., Theodorakopoulos G., Petsalakis I.D., Ajami D.; Rebek, J., *Journal of American Chemical Society*, 2012, 134 (9), 4346–4354.
- (2) Ikeda, T., Mamiya, J.-I., Yu, Y., *Angewandte. Chemie, International Edition*, 2007, 46, 506–528.
- (3) Kinoshita T., *Journal of Photochemistry and Photobiology, B* 1998, 42, 12–19.
- (4) Kuad P., Miyawaki A., Takashima Y., Yamaguchi H., Harada A., *Journal of American Chemical Society*, 2007, 129, 12630–12631.
- (5) Wu W., Yao L., Yang T., Yin R., Li F., Yu Y., *Journal of American Chemical Society*, 2011, 133, 15810– 15813.
- (6) Humblet-Hua N.-P.K., van der Linden E., Sagis L.M.C., *Journal of Agricultural and Food Chemistry*, 2012, 60, 9502–9511.
- (7) Giraud S., Bourbigot S., Rochery M., Vroman I., Tighzert L., Delobel R., Poutch F., *Polymer Degradation and Stability*, 2005, 88, 106–113.
- (8) Polavarapu S., Oliver C.M., Ajlouni S., Augustin M.A., *Journal of Agricultural and Food Chemistry*, 2012, 60, 444–450.
- (9) Fickert J., Makowski M., Kappl M., Landfester K., Crespy D., *Macromolecules* 2012, 45, 6324–6332.
- (10) Pedone A., Bloino J., Barone V., *Journal of Physical Chemistry C*, 2012, 116, 17807–17818.
- (11) Rawat S., Kohli N., Suri C.R., Sahoo D.K., *Molecular Pharmaceutics*, 2012, 9, 2403–2414.
- (12) Blaiszik B.J., Caruso M.M., McIlroy D.A., Moore J.S., White S.R., Sottos N.R., *Polymer*, 2009, 50, 990–997.
- (13) Wang X., Yang Y., Liao Y., Yang Z., Jiang M., Xie X., *European Polymer Journal*, 2012, 48, 41–48.
- (14) Bédard M.F., Geest B.G.D., Skirtach A.G., Möhwald H., Sukhorukov G.B., *Advances in Colloid and Interface Science*, 2010, 158, 2–14.
- (15) Esser-Kahn A.P., Odom S. A., Sottos N.R., White S.R., Moore J.S., *Macromolecules*, 2011, 44, 5539–5553.

Chapter 2

- (16) Erokhina S., Benassi L., Bianchini P., Diaspro A., Erokhin V., Fontana M.P., *Journal of American Chemical Society*, 2009, 131, 9800–9804.
- (17) Tylkowski B., Pregowska M., Jamowska E., Garcia-Valls R., Giamberini M., *European Polymer Journal*, 2009, 45, 1420–1432.
- (18) Peña B., Panisello C., Aresté G., Garcia-Valls R., Gumí T., *Chemical Engineering Journal*, 2012, 179, 394–403.
- (19) Torras C., Pitol-Filho L., Garcia-Valls R., *Journal of Membrane Science* 2007, 305, 1–4.
- (20) Ao Q., Wang A., Cao W., Zhang L., Kong, L., He Q., Gong Y., Zhang X., *Journal of Biomedical Materials Research, Part A*, 2006, 77A, 11–18.
- (21) Tylkowski B., Trusheva B., Bankova V., Giamberini M., Peev G., Nikolova A., *Journal of Membrane Science*, 2010, 348, 124–130.
- (22) Torras C., Garcia-Valls R., *Journal of Membrane Science*, 2004, 233, 119–127.
- (23) Horcas R.F., Gómez-Rodríguez J.M., Colchero J., Gómez-Herrero J., *Review of Scientific Instruments*, 2007, 78, 013705–1–013705–8.
- (24) Jastrzab R., *Journal of Coordination Chemistry*, 2012, 66, 98–113.
- (25) Chen S.-H., Liou R.-M., Lai J.-Y., Lai C.-L., *European Polymer Journal*, 2007, 43, 3997–4007.
- (26) Niwa M., Kawakami H., Kanamori T., Shinbo T., Kaito A., Nagaoka S., *Macromolecules* 2001, 34, 9039–9044.
- (27) Barton B.F., Reeve J.L., McHugh A.J., *Journal of Polymer Science, Part B: Polymer Physics*, 1997, 35, 569–585.
- (28) van de Witte, P.; Esselbrugge, H.; Dijkstra, P. J.; van den Berg, J. W. A.; Feijen, J., *Journal of Membrane Science*, 1996, 113, 223–236.
- (29) Peltonen J., Järn M., Areva S., Linden M., Rosenholm J.B., *Langmuir*, 2004, 20, 9428–9431.
- (30) Gizli N., *Chemistry & Chemical Technology*, 2011, 5, 327–331.
- (31) Raulio M., Järn M., Ahola J., Peltonen J., Rosenholm J., Tervakangas S., Kolehmainen J., Ruokolainen T., Narko P., Salkinoja-

Chapter 2

Salonen M., *Journal of Industrial Microbiology and Biotechnology*, 2008, 35, 751–760.

(32) Ryan B.J., Poduska K.M., *American Journal of Physics*, 2008, 76, 1074–1077.

(33) Lowry T.H., Richardson K.S., *Mechanism and Theory in Organic Chemistry*, Harper and Row, 1987.

(34) Ogasawara S., Saito I., Maeda M., *Tetrahedron Letters*, 2008, 49, 2479–2482.

(35) Hikmet R.A.M., Zwerver B.H., Lub J., *Macromolecules* 1994, 27, 6722–6727.

(36) Taran F., Renard P.Y., Bernard H., Mioskowski C., Frobert Y., Pradelles P., Grassi J., *Journal of American Chemical Society*, 1998, 120, 3332–3339.

(37) Kayaci F., Uyar T., *Journal of Agricultural and Food Chemistry*, 2011, 59, 11772–11778.

(38) Peña B., de Ménorval L.-C., Garcia-Valls R., Gumí T., *ACS Applied Materials and Interfaces*, 2011, 3, 4420–4430.

(39) Peña B., Ferré L., Garcia-Valls R., Ferrando F., Gumí T., *Industrial and Engineering Chemistry Research*, 2011, 50, 2073–2079.

(40) Tylkowski B., Bogdanowicz K.A., Ambrogi V., Lederer A., Patroniak V., Giamberini M., *Polymer International*, 2014, 63, 315–326.

Chapter 3

An Atomistic Insight into Light-sensitive Polymers with Methylstilbene Building Blocks

Nuno A. G. Bandeira, Bartosz Tylkowski, Krzysztof Artur Bogdanowicz,

Marta Giamberini and Carles Bo*

*- *Polymer International* **2015**; 64, 935–941

UNIVERSITAT ROVIRA I VIRGILI
LIQUID CRYSTALLINE POLYMERS FOR SMART APPLICATIONS.
Krzysztof Artur Bogdanowicz
Dipòsit Legal: T 1677-2015

Chapter 3

1.3.1. Introduction

Stilbenes are among the most extensively investigated compounds with regard to their unique photochemistry.¹ They are highly photosensitive species, which undergo several photoreactions when exposed to light. Trans–cis isomerisation is the main photochemical process in low-molecular-weight stilbene derivatives; however, [2+2] photocycloaddition and oxidative cyclization of the cis isomer forming phenanthrene derivatives may also occur.² Stilbene derivatives in the trans state have an extended conformation and are rod-like; in contrast, in the cis state they do not possess the linear form required for liquid crystallinity. As a consequence of such a drastic conformational change, they isothermally become isotropic under UV radiation. For stilbenes, thermal back-reaction has not been reported, since it does not readily take place.³ For this reason, main-chain polymers based on α -methylstilbene have been reported to exhibit irreversible photochromic properties.⁴ Owing to their photoresponsive conformational changes, stilbene derivatives are suitable moieties for the synthesis of 'smart' materials and due to their photochemical properties they are still the subject of numerous studies and controversies.^{5–9} In the literature, there are many examples concerning the preparation of photoactive polymer-based films containing stilbene as the photoactive unit.^{10–12}

Recently, controlled release of contents from polymeric microcapsules has been of considerable interest in applications such as coatings,¹³ food additives,¹⁴ catalysts,¹⁵ dyes¹⁶ and drugs.¹⁷ The utility of microcapsules as vehicles for cargo storage stems from their ability to deliver beneficial agents 'just in time' to affect the outcome of larger systems. Microcapsules can release their contents in response to various stimuli such as mechanical damage,¹⁸ temperature,¹⁹ pH, ionic strength, electric field and magnetic flux.²⁰ The possibility of triggering release by light irradiation has become of particular interest: for applications in agricultural and cosmetic fields, UV- and visible-light-sensitive microcapsules are desirable, while near-IR-absorbing capsules are more suitable for applications related to biological systems. In general, microcapsules can be made sensitive to light by incorporation of light-sensitive polymers, functional dyes and metal nanoparticles. In a previous paper,²¹ we prepared microcapsules containing vanillin, whose properties could be modulated by means of UV light. Photoresponsive microcapsules based on poly[(α -methylstilbenesebacate)-co-(α -methylstilbeneisophthalate)] (P4) (Fig. 1.3.1) were prepared using a phase inversion method. P4 is a novel nematic liquid-crystalline polymer

Chapter 3

of our synthesis, with a glass transition of 45 °C and clearing point of 238 °C.²² This polymer possesses an amorphous structure and a reasonably low glass transition value because of the incorporation of isophthaloyl moieties in the polymer backbone. Before preparing and characterizing microcapsules, we performed an exhaustive characterization of a membrane based on P4 polymer obtained using conditions as similar as possible to those of microcapsule preparation. In order to simulate the morphology and behaviour of the microcapsule shell under UV irradiation, membrane characterization was first carried out using environmental scanning electron microscopy (ESEM), by measuring contact angles with water and using AFM. On the basis of AFM investigations, it was seen that the P4 film morphology changed drastically as a consequence of its exposure to UV irradiation at 365 nm: root mean square roughness, considered as a standard, deviation of height was decreased by ca 24%. The surface skewness, which depicts the asymmetry of the height distribution, changed from a negative value before UV irradiation to a positive one after UV irradiation. Moreover the average height of the film was found as 133.6 nm before and 100.1 nm after UV irradiation. Obtained results confirmed smoothing of the membrane surface after UV irradiation.

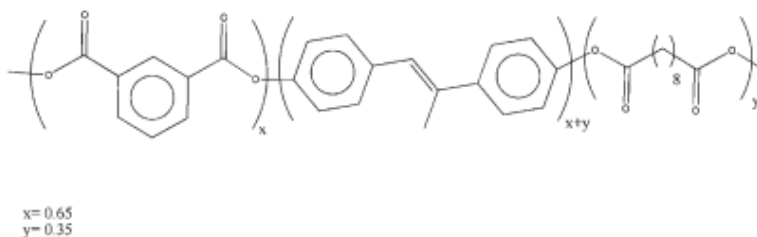


Figure 1.3.1. Structure of poly[(α -methylstilbenesebacate)-co-(α -methylstilbeneisophthalate)].²¹

Moreover, release experiments showed that vanillin release from microcapsules in water at room temperature was strongly influenced by UV irradiation: in the absence of irradiation, release was negligible while, when microcapsules were submitted to continuous irradiation with UV light for 35min, vanillin was quickly released after an induction time of about 20 min. This evidence suggests that photo-triggered release from such microcapsules occurred as a consequence of trans–cis photoisomerization of α -methylstilbene moieties in the polymer backbone which forms microcapsule shell, during UV irradiation.

Chapter 3

A considerable number of computational studies have been devoted to the stilbene molecule with regards to its photoisomerization mechanism which proceeds via singlet $\pi-\pi^*$ (S0-S1) excitation.²³⁻²⁷ A recent study by Pal et al.²⁸ involved excited-state time-dependent density functional theory (TDDFT) calculations for cis- and trans-stilbene as well as for derivatives that combine the stilbene framework with organomagnetically prone moieties such as tetrathiafulvalene or verdazyl so as to assess their behaviour as optical switches. A very recent study by Quenneville and Martínez²⁹ using CASSCF/CASPT2 methods shed some light on the nature of the transition state of the photoisomerization process and the conical intersection through which it undergoes fluorescent non-radiative decay. This conical intersection point lies close to the S1 global minimum and the photoisomerization process parallels that of ethene. Those authors also stress the need for a two-dimensional reaction coordinate involving not only the twisting of the ring planes but also the pyramidalization of the geometry of the diradical—CH₂—unit in the conical intersection region.

Among the first modern density functional theory (DFT) calculations is the one reported in the paper by Choi and Kertesz,³⁰ which provides a structural and vibrational analysis of the ground-state cis and trans isomers. Those authors saw a contrasting answer between DFT and wavefunction methods (MP2) with regards to the preference of trans-stilbene for planarity. Whereas the former method yielded a preferentially planar molecule as an energy minimum, the latter favoured a nonplanar phenyl ring arrangement albeit not by any large amount (0.8 kcalmol⁻¹).

In an effort to understand the structural basis for the release behaviour of previously studied microcapsules, in the work reported in this paper we carried out an in-depth study by means of quantum chemical calculations using periodic boundary conditions to unveil some of the structural features of the P4 polymer. The rate-limiting step for the trans to cis photochemical conversion is the vertical excitation energies of the chains. Starting with the precursor monomers, cis- and trans-4,4'-(prop-1-ene-1,2-diyl)diphenol (pddp), and model structures of P4, the vertical excitation energies were computed to verify any trend in their magnitude with increasingly larger monomeric units and with various functional groups.

1.3.2. Computation Details

All calculations were performed with the Gaussian0931 revision A.02 program. The Heyd-Scuseria-Ernzerhof³²⁻³⁵ hybrid semi-local

Chapter 3

exchange and the Perdew, Burke and Ernzerhof correlation density functionals, herein denoted as HSEh1PBE (otherwise known as HSE06 in the literature), were used as the method of choice for the calculations. This short-range hybrid functional curtails the computational unwieldiness involving the calculation of exact exchange in systems with periodic boundary conditions while retaining the advantage of hybrid functionals such as the proper quantification of band gaps.³⁵ The Pople 6-31G* contracted Gaussian basis set was used for the periodic boundary calculations while the extended 6-311+G** basis set was used for the time-dependent single-point calculations on pre-optimized structures. The number of roots was a total of 20 singlet and triplet excitations.

Geometry optimizations were performed on the atomic coordinates and the unit cell lengths until the default program convergence criteria were met and without any symmetry constraints.

1.3.3. Results and Discussion

Before studying the molecules and polymers, it is important to validate the reproduction of the experimental structural parameters by the computational methodology (previous section). So the simpler *cis*- and *trans*-stilbene (supporting information) provided a test bed to initiate this study. The *trans*-stilbene molecule was characterized crystallographically by Bouwstra et al.³⁶ (CCDC ref. CUHDOY) but *cis*-stilbene has been considerably harder to isolate in a single crystal without any structural disorder. This is likely due to the possible arrangements of the phenyl ring planes which must be offset to avoid steric hindrance. However, in a recent paper by Tabellion et al.,³⁷ a *cis*-stilbene molecule was successfully co-crystallized with a manganese complex (CCDC ref. NERFEV) without any disorder, thus providing a good source of structural parameters for this isomer. The mean structural parameters of the optimized geometries are given in Table S1.3.1 (supporting information). The calculated values compare quite well with the experimental bond lengths. In particular, the C2=C3 bond which is 1.34 Å for the *cis* isomer and 1.33 Å for the *trans* isomer is well reproduced by theHSEh1PBE functional and is similar to the values obtained by Pal and others. The C1—C2 and C3—C4 bond lengths also tally with previously published results and experimental values.

The optimized geometries of *cis*- and *trans*-pddp present very similar structural features with regards to conventional stilbene. The presence of an additional methyl group and the addition of the —OH groups in the stilbene framework should change the electronic properties

Chapter 3

of the two isomers. The optimized structures of *cis*- and *trans*-pddp, depicted in Fig. 1.3.2, present no major structural differences from those of stilbene. The C=C bond in *trans*-pddp is some 0.02 Å longer than in *trans*-stilbene, and the (C1–C2–C3–C4) angle in *cis*-pddp is also 7° like in its parent compound. The ring plane offset in *cis*-pddp is 78°, which is some 10° more than in *cis*-stilbene, likely due to the additional steric hindrance caused by the presence of the —OH groups. The π -orbitals of *trans*- and *cis*-pddp are identical (Fig. 1.3.3) making up the HOMO of the two systems, in which the C2 ($2p\pi$)—C3 ($2p\pi$) orbitals overlap in phase and there is some contribution from the —OH groups as well as the 1 s orbitals from the hydrogens in the sp^3 carbon of the methyl group. A comparative analysis between *trans*-pddp with the corresponding molecular orbitals in *trans*-stilbene shows that this molecular orbital has increased in energy, from (HOMO)=−5.676 eV to −5.129 eV, due to the out-of-phase combination with the $2p\pi$ orbital from the —OH group. A similar increase in the *cis* isomers is also seen (−5.858 to −5.369 eV).

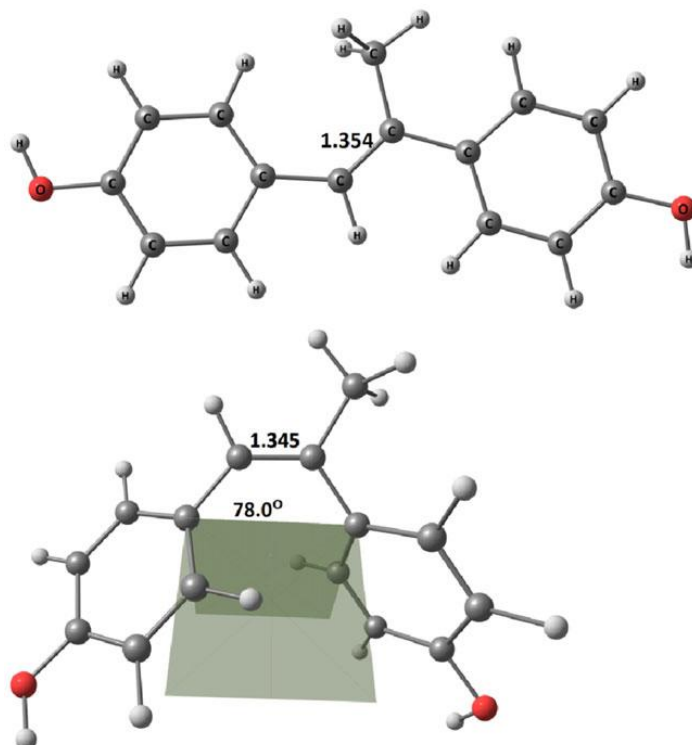


Figure 1.3.2. Optimized structures of *cis*- and *trans*-pddp with important structural parameters such as C=C bond length and ring plane offset.

Chapter 3

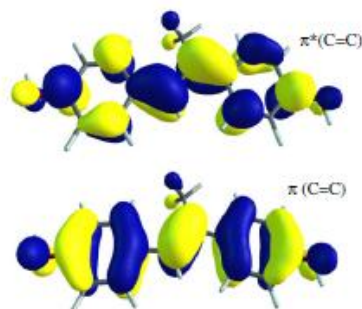


Figure 1.3.3. Frontier molecular orbitals of trans-4,4'-(prop-1-ene-1,2-diyl)diphenol.

The bulk structural properties of the P4 polymer have already been reported, in particular the chain morphology,²¹ which is seen to possess more grooves in the cis (post-irradiation) than in the trans form. The structural features of P4-based microcapsules can best be reproduced at the atomistic level using periodic boundary conditions despite introducing the spatial symmetry constraint of mono-dispersion. Indeed a more accurate reproduction of the proportion of the isophthaloyl, stilbene and aliphatic structural units would render the calculation computationally intractable. Thus we opted to create two families of models: one with a short saturated hydrocarbon chain length (cis- and trans-C2) and another with a longer chain length (cis- and trans-C8), while maintaining the isophthaloyl ratio of 1:1 instead of the actual ratio depicted in Fig. 1.3.1.

Each unit cell (monomer unit) has three aromatic units and one alkene moiety. The results match the experimental finding with regards to the bulk surface roughness of the microcapsules. As we reported previously, morphological changes of the P4 microcapsule shells, caused during release experiments by UV irradiation, were investigated using ESEM. Figure S1.3.1 (supporting information) shows a comparison of the morphology between microcapsules after preparation (Fig. S1.3.1a) and recovered after 30 min of the vanillin release experiment in the absence (Fig. S1.3.1b) and presence (Fig. S1.3.1c) of UV irradiation at 365 nm. Marked differences between the images are seen. Surface morphology of the un-irradiated microcapsules looks very similar to the morphology of the microcapsules before the release experiment, as shown in Fig. S1.3.1a, while it changes markedly in the case of irradiated

Chapter 3

microcapsules, since they do not look well-formed and globe-shaped any more but are concaved and perforated.

The minimum energy structures of the periodic trans-C2 (Fig. 1.3.4) and cis-C2 models (Fig. 1.3.5) reflect this trend in that the trans-C2 chain exhibits a larger stretch per monomer so as to maintain co-planarity between the carboxylate groups and the phenyl ring of the isophthaloyl fragment whereas a similar co-planarity is also exhibited within the stilbene fragment. The optimized unit cell length of trans-C2 is 23.5 Å and that of cis-C2 is 18.8 Å. An examination of the electronic structure of trans-C2 reveals that the frontier molecular orbital region is no longer made up solely of the π and π^* molecular orbitals localized in the stilbene fragment like in the trans-pddp precursor. The valence band belongs to the $\pi(\text{C}=\text{C})$ set but the lowest lying virtual band is an anti-bonding linear combination of atomic orbitals from the isophthaloyl unit. A plot of the highest occupied crystal orbital (HOCO) and the lowest unoccupied crystal orbital (LUCO) and their eigen values at $k = 0$ are presented in Fig. 1.3.6. The LUCO+2 which displays the $\pi^*(\text{C}=\text{C})$ also displays a considerable delocalization onto the phthaloyl π manifold. The LUCO+1 is also localized on the isophthaloyl unit and has π symmetry.

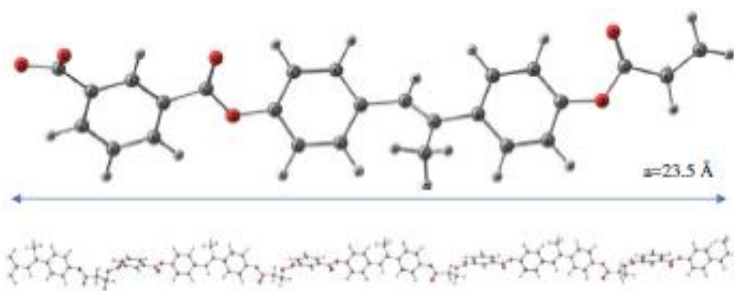


Figure 1.3.4. Unit cell (top) and extended polymer (bottom) of trans-C2.

Chapter 3

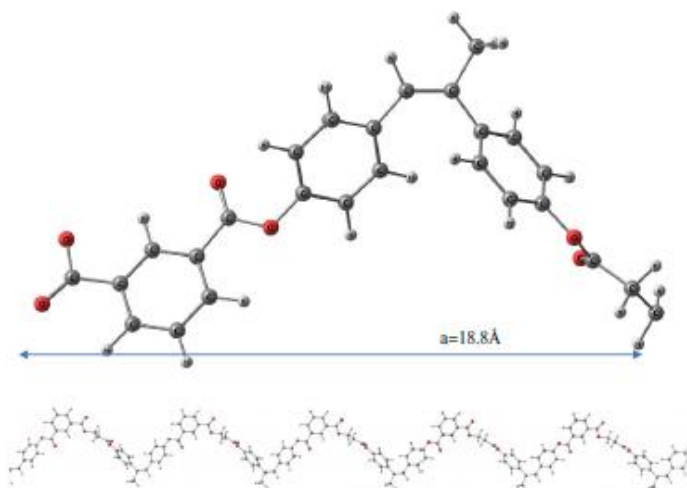


Figure 1.3.5. Unit cell (top) and extended polymer (bottom) of cis-C2.

The longer chain models cis-C8 and trans-C8 show a unit cell length of 25.6 and 31.0 Å, respectively (Fig. S1.3.2, supporting information), which corresponds to an approximate unit cell growth of 0.23 Å per methylene unit under the assumption of linear chain growth. Their respective band gaps differ by 0.05 eV, the higher gap belonging to cis-C8. The frontier crystal orbital composition is qualitatively identical to the lighter C2 derivatives. The band dispersion along the Brillouin zone ($0 \leq k \leq \pi/a$, with a being the unit cell length) for all the periodic systems considered is under 2 meV so that the HOCO–LUCO+2 gap at $k=0$ is synonymous with the valence band to third lowest virtual band gap.

In order to understand the changes in the absorption spectra upon changing the trans to the cis isomer and since, due to software limitations, TDDFT calculations cannot be performed on periodic models, new molecular models (cis-M and trans-M) were created adapting the optimized polymers by shortening the alkyl tail of the monomer to a methyl group and re-optimizing. Despite the constraints of the periodic boundary conditions not being present the geometries do not change significantly (Fig. 1.3.7) from the periodic models. The time-dependent calculations can then be compared with the experimentally obtained UV-visible absorption spectra and thus one is able to interpret the trends from the band shifts. A summary of the main data from all the models is listed in Table 1.3.1 including relative interconversion electronic energies between

Chapter 3

each isomer. It is clear that the $\pi \rightarrow \pi^*$ energy gaps in cis-M and trans-M do not differ significantly from their periodic counterparts cis-C2 and trans-C2 thus confirming the former to be good reproductions of the periodic models. The $\pi \rightarrow \pi^*$ level gaps in the C8 models are approximately the same with respect to the shorter C2 chain polymers.

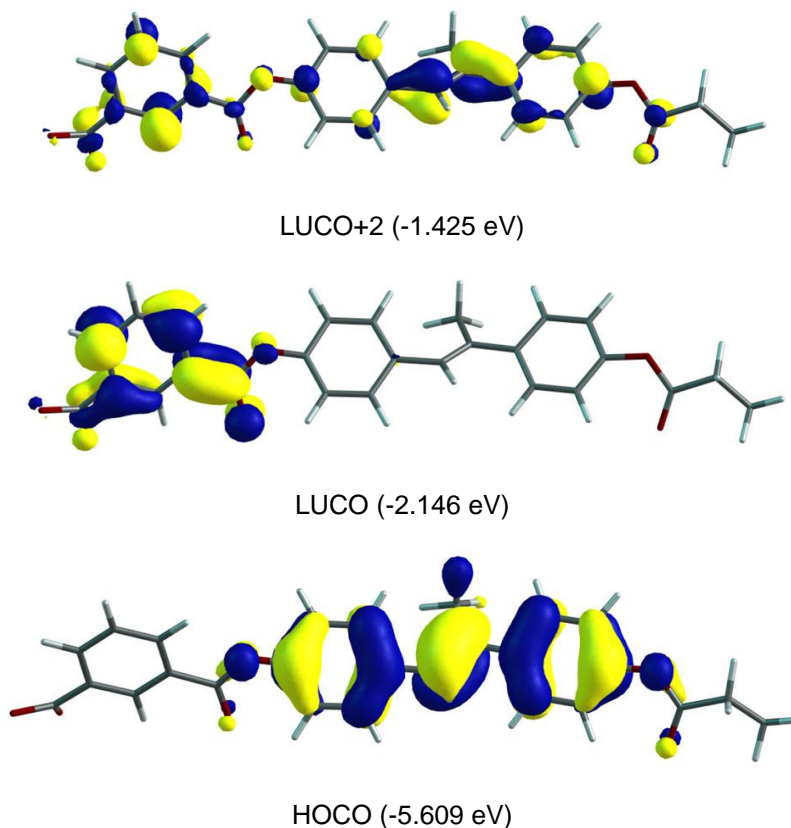


Figure 1.3.6. Frontier crystal orbitals (Γ point) of trans-C2.

Chapter 3

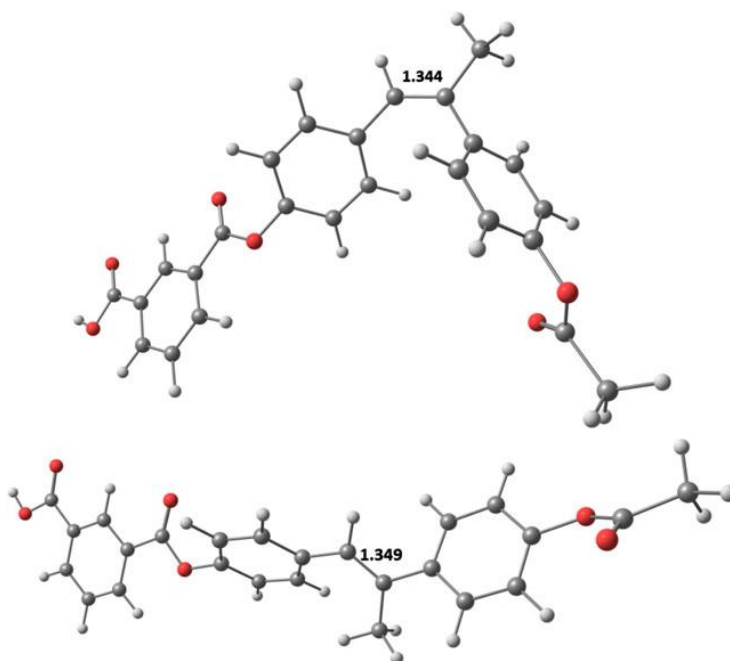


Figure 1.3.7. Molecular models adapted from the optimized polymers: cis-M (top) and trans-M (bottom) with C=C bond lengths (Å).

Table 1.3.1. Electronic, structural and energetic properties of molecular and periodic models

Model	Unit cell spacing (Å)	$\pi(\text{C}=\text{C}) \rightarrow \pi^*(\text{C}=\text{C})$ gap (eV)	ΔE (kJmol ⁻¹)
<i>cis</i> -Stilbene	-	4.11	+17.6
<i>trans</i> -Stilbene	-	3.67	0
<i>cis</i> -pddp	-	4.18	0
<i>trans</i> -pddp	-	3.52	+13.5
<i>cis</i> -M	-	4.35 ^a	+0.8
<i>trans</i> -M	-	4.18 ^a	0
<i>cis</i> -C2	18.8	4.27 ^b	+0.1
<i>trans</i> -C2	23.5	4.21 ^b	0
<i>cis</i> -C8	25.6	4.30 ^b	+4.4
<i>trans</i> -C8	31.0	4.23 ^b	0

^a Corresponding to HOMO \rightarrow LUMO+2 transition.

^b Corresponding to HOCO \rightarrow LUCO+2(k=0) gap at the Brillouin zone

Chapter 3

The TDDFT spectra of cis- and trans-M and cis- and trans-pddp molecules together with the experimental UV-visible spectra of the microcapsules before and after UV light exposure are displayed in Fig. 1.3.8. The first excitation in M within the singlet class corresponds to a HOMO→LUMO transition or qualitatively to a charge transfer from the $\pi(\text{C}=\text{C})$ bond to a π^* molecular orbital in the isophthaloyl moiety, and which is 359 and 365 nm, respectively, for the cis and trans isomers. The second transition (Table 1.3.2) is 319 and 323nm for cis and trans, respectively, also a charge transfer to the isophthaloyl moiety. These initial transitions are weak since they show a small oscillator strength (<0.2). The $\pi(\text{C}=\text{C})\rightarrow\pi(\text{C}=\text{C})^*$ transition has a strong intensity for the trans-M isomer at a calculated wavelength of 294nm while the corresponding cis-M transition is significantly weaker and downshifted (289 nm). This trend is seen experimentally where the absorption maxima in this region are at 303nm ($t=0$ min exposure to UV light) and later ($t=50$ min) at 287 nm. The second absorption bands at $\lambda < 200$ nm are poorly reproduced by the calculations mainly for two reasons: they are close to the uppermost part of the CI space (i.e. fourteenth and sixteenth roots), and they have π^* contributions from the isophthaloyl unit, which in the real microcapsules is present in a lesser proportion than in the models, used (Fig. 1.3.1). In the cis- and trans-pddp molecules, there is no isophthaloyl unit and this second band is more accurately reproduced.

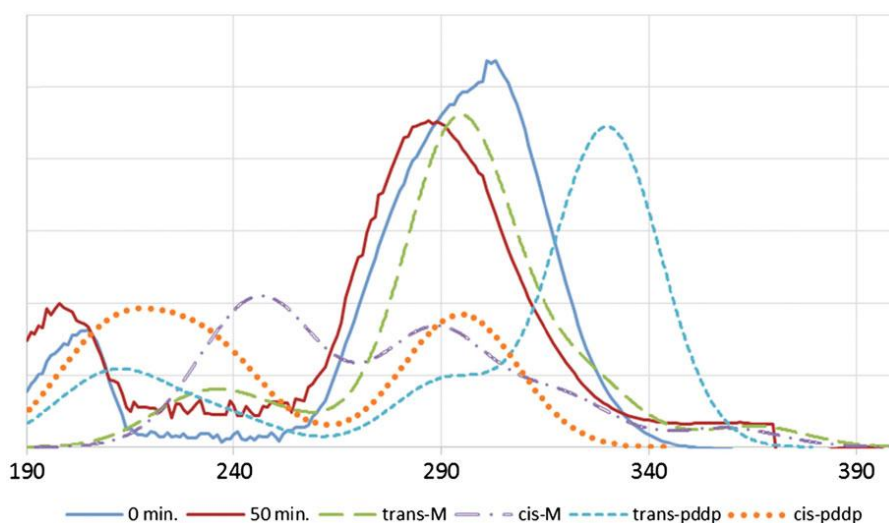


Figure 1.3.8. Experimental and simulated UV-visible spectra (nm). A Gaussian broadening was used in the theoretical transition peaks.

Chapter 3

Table 1.3.2. Main excitations from each precursor isomer with assignments to respective molecular orbital transition

Compound	λ (nm)	Partial character of $g(C=C) \rightarrow g^*(C=C)$ transition	Oscillator Strength, f
<i>cis</i> -Stilbene	303 (276) ^a	0.699 (H→L)	0.347
<i>trans</i> -Stilbene	317 (293) ^a	0.703(H→L)	0.915
<i>cis</i> -pddp	300	0.670(H→L); -0.206(H→L+1)	0.309
<i>trans</i> -pddp	330	0.702(H→L)	1.07
<i>cis</i> -M	289	0.692 (H→L+2)	0.301
<i>trans</i> -M	294	0.700 (H→L+2)	0.903

^a Experimental values in parentheses taken from Pal et al.²⁶

The important aspect of these results is that the photoactive experimental absorption band shift is reproduced by the calculations in terms of wavelength (lower wavelength after conversion) and decreasing band intensity, thus confirming the *trans*→*cis* isomer conversion in the P4 microcapsules. The reverse *cis*→*trans* reaction should be kinetically slower since the calculated absorption probability is some three times less in *cis*-M.

1.3.4. Conclusions

Microcapsules are small particles that contain an active agent or core material surrounded by a coating or shell. The encapsulation of materials for protection and phase separation has evolved into a major interdisciplinary research focus. The main aim of our research is to foster the discovery of breakthrough technologies for the controlled delivery of actives, in order to optimize and control their delivery and impact via determined release points, while minimizing the quantity of materials used for the expected purpose. So, we focused on the development and testing of new photo-control release microcapsules.

In this paper, in order to understand the structural basis for the release behaviour of microcapsules based on P4, containing the photosensitive α -methylstilbene moiety, we carried out an investigation, by means of quantum chemical calculations using periodic boundary conditions, to study some of the structural features of the P4 polymer. The pddp precursor molecules were computationally optimized and their electronic structure was characterized in which the $\pi(C=C) \rightarrow \pi(C=C)^*$ transition is the HOMO–LUMO gap for each isomer. Incorporating the

Chapter 3

isophthaloyl unit will add two further virtual molecular orbitals (LUMO and LUMO+1) mostly localized in this moiety thus placing the photoactive $\pi(\text{C}=\text{C})^*$ as the LUMO+2. The periodic models show a linear arrangement in the trans-C2 and trans-C8 chains whereas the cis-C2 and cis-C8 chains are 4.7 and 5.4 Å shorter per monomer unit thus allowing for increased grooves in the whole microcapsule as witnessed experimentally. Our theoretical calculation is fully consistent with the previously reported experimental evidence, indicating that all the results obtained from characterization of a flat membrane, as well as ESEM observation of microcapsule morphological changes during vanillin release under UV irradiation, occur as a consequence of the P4 polymer backbone conformational changes induced by α -methylstilbene moiety trans-cis isomerization.

1.3.5. Acknowledgement

NAGB gratefully acknowledges the MC/COFUND scheme ref. 291787-ICIQ-IPMP for funding.

1.3.6. Supporting information

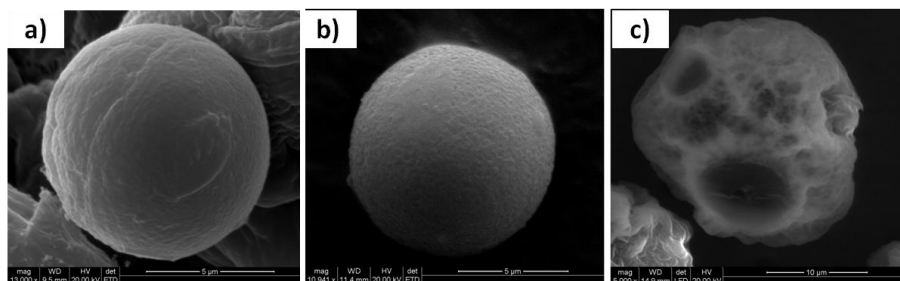


Figure S1.3.1. ESEM micrographs of a) single microcapsule containing vanillin in chloroform as a filler after preparation, b) after 30 minutes of release experiment at room temperature without UV light and c) accompanied by UV irradiation at 365 nm.

Chapter 3

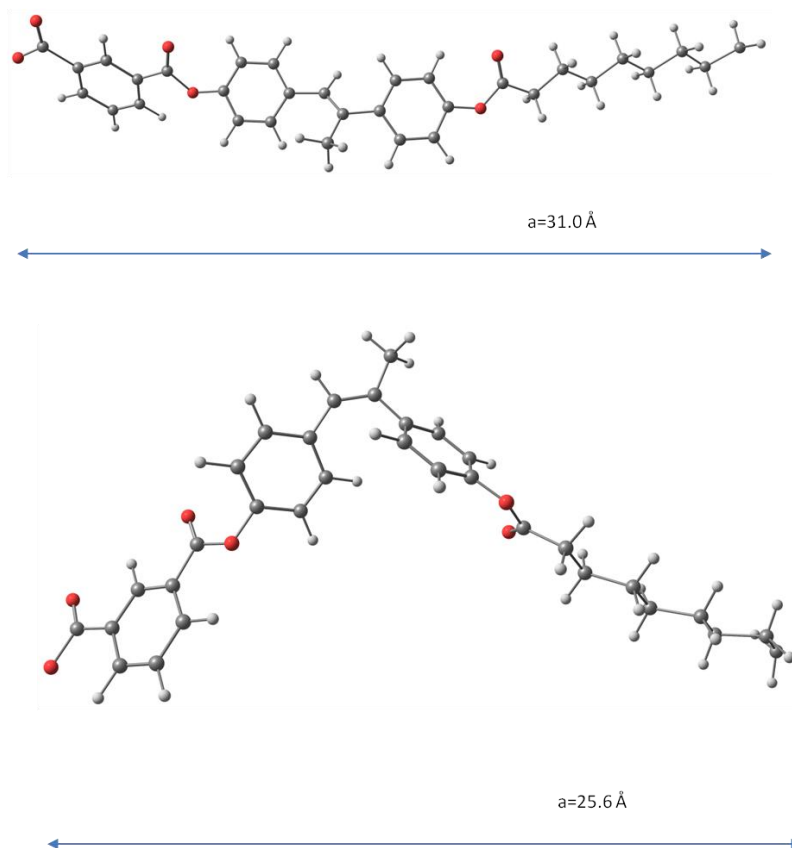


Figure S1.3.2. Unit cells of *trans*-C8 (top) and *cis*-C8 (bottom).

Table S1.3.1. Selected mean structural parameters of the *cis*- and *trans*-stilbene isomers

Structural parameters (Å,deg.)	this work		Pal et al. ¹		Exp.	
	<i>trans</i> -	<i>cis</i> -	<i>trans</i> -	<i>cis</i> -	<i>trans</i> - ²	<i>cis</i> - ³
C2-C3	1.343	1.343	1.345	1.335	1.330	1.339
C1-C2/C3-C4	1.460	1.469	1.465	1.491	1.471	1.466
∠(C1-C2-C3-C4)	180.0	6.6	180.0	0.2	180.0	5.5

Chapter 3

1.3.7. References

- (1) Ioffe I.N., Granovsky A.A., *Journal of Chemical Theory and Computation*, 2013, 9, 4973–4990.
- (2) Malkin A., Wood A., Ross D.L., Blanc J., in *Photochromism (Techniques of Chemistry)*, ed. by Brown G.H. Wiley-Interscience, New York, vol. III, 1971, p. 471 .
- (3) Lowry T.H., Schueller Richardson K., *Mechanism and Theory in Organic Chemistry*. Harper & Row, New York ,1987.
- (4) Rameshbabu K., Kannan P., *Polymer International*,2006, 55,151–157.
- (5) Tzeli D., Theodorakopoulos G., Petsalakis I.D., Ajami D., Rebek J., *Journal of American Chemical Society*, 2012, 134, 4346–4354.
- (6) Ikeda T., Mamiya J.-I., Yu Y., *Angewandte Chemie International Edition*, 2007, 46, 506–528.
- (7) Kinoshita T., *Journal of Photochemistry and Photobiology*, B 1998, 42, 12–19.
- (8) Kuad P., Miyawaki A., Takashima Y., Yamaguchi H., Harada A., *Journal of American Chemical Society*, 2007, 129, 12630–12631.
- (9) Wu W., Yao L., Yang T., Yin R., Li F., Yu Y., *Journal of American Chemical Society*, 2011, 133, 15810–15813.
- (10) Ding L., Russell T.P., *Macromolecules*, 2006, 39,6776–6780.
- (11) Hahm S.G., Lee S.W., Lee T.J., Cho S.A., Chae B., Jung Y.M. et al, *Journal of Physical Chemistry B*, 2008, 112, 4900–4912.
- (12) Altomare A., Carlini C., Ciardelli F., Panattoni M., Solaro R., Houben J.L., *Macromolecules* 1985, 18, 729–734.
- (13) Giraud S., Bourbigot S., Rochery M., Vroman, I., Tighzert L., Delobel R., Poutch F., *Polymer Degradation and Stability*, 2005, 88, 106–113.
- (14) Polavarapu S., Oliver C.M., Ajlouni S., Augustin M.A., *Journal of Agricultural and Food Chemistry*, 2012, 60, 444–450.
- (15) Fickert J., Makowski M., Kappl M., Landfester, K., Crespy D., *Macromolecules* 2012, 45, 6324–6332.

Chapter 3

- (16) Pedone A., Bloino J., Barone V., *Journal of Physical Chemistry C*, 2012, 116, 17807–17818.
- (17) Rawat S., Kohli N., Suri C.R., Sahoo D.K., *Molecular Pharmaceutics*, 2012, 9, 2403–2414.
- (18) Blaiszik B.J., Caruso M.M., McIlroy D.A., Moore J.S., White S.R., Sottos N.R., *Polymer*, 2009, 50, 990–997.
- (19) Tylkowski B., Pregowska M., Jamowska E., Garcia-Valls R., Giamberini M., *European Polymer Journal*, 2009, 45, 1420–1432.
- (20) Wang X., Yang Y., Liao Y., Yang Z., Jiang M., Xie X., *European Polymer Journal*, 2012, 48, 41–48.
- (21) Bogdanowicz K.A., Tylkowski B., Giamberini M., *Langmuir*, 2012, 29, 1601–1608.
- (22) Tylkowski B., Bogdanowicz K.A., Ambrogi V., Lederer A., Patroniak V., Giamberini M., *Polymer International*, 2014, 63, 315–326.
- (23) Orlandi G., Palmieri P., Poggi G., *Journal of American Chemical Society*, 1979, 101, 3492–3497.
- (24) Amatatsu Y., *Chemical Physical Letters*, 1999, 314, 364–368.
- (25) Amatatsu Y., *Journal of Molecular Structure: THEOCHEM*, 1999, 461–462, 311–316.
- (26) Dou Y., Allen R.E., *Journal of Chemical Physics*, 2003, 119, 10658–10666.
- (27) Minezawa N., Gordon M.S., *Journal of Physical Chemistry A*, 2011, 115, 7901–7911.
- (28) Pal A.K., Hansda S., Datta S.N., Illas F., *Journal of Physical Chemistry A*, 2013, 117, 1773–1783.
- (29) Quenneville J., Martínez T.J., *Journal of Physical Chemistry A*, 2003, 107, 829–837.
- (30) Choi C.H., Kertesz M., *Journal of Physical Chemistry A*, 1997, 101, 3823–3831.
- (31) Frisch M.J., Trucks G.W., Schlegel H.B., Scuseria G.E., Robb M.A., Cheeseman J.R. et al, *Gaussian09 rev. A02* (2009).

Chapter 3

- (32) Heyd J., Scuseria G.E. and Ernzerhof M., *Journal of Chemical Physics*, 2003, 118, 8207–8215.
- (33) Heyd J., Scuseria G.E., Ernzerhof M., *Journal of Chemical Physics*, 2006, 124, 219906.
- (34) Krukau A.V., Vydrov O.A., Izmaylov A.F., Scuseria G.E., *Journal of Chemical Physics*, 2006, 125, 224106.
- (35) Henderson T.M., Izmaylov A.F., Scalmani G., Scuseria G.E., *Journal of Chemical Physics* 2009, 131, 044108.
- (36) Bouwstra J.A., Schouten A., Kroon J., Helmholtz R.B., *Acta Crystallographica C*, 1985, 41, 420–426.
- (37) Tabellion F.M., Seidel S.R., Arif A.M., Stang P.J., *Journal of American Chemical Society*, 2001, 123, 11982–11990.

Part 2

Application of Discotic Liquid Crystalline Polymers

UNIVERSITAT ROVIRA I VIRGILI
LIQUID CRYSTALLINE POLYMERS FOR SMART APPLICATIONS.
Krzysztof Artur Bogdanowicz
Dipòsit Legal: T 1677-2015

This part is focused on obtaining novel proton exchange membrane, which could be an alternative to commercially available materials. To reach the objectives, polyamines modified with liquid-crystalline discotic dendrons in lateral position were used as an active part of hybrid membranes supported on anodised aluminium oxide membrane.

The chapter number four gives a description of proton conductivity studies for liquid crystalline polyether-based membrane *via* electrochemical impedance and discuss in details its morphology. In this way, we showed that LCPs self-assembling approach can be successfully used to prepare new proton-conducting membranes. In the fifth chapter, the synthesis of new generation of membranes is enlightened using a polyamine with the same dendritic group like for polyether. The sixth chapter emphasises the comparison of two techniques, electrochemical impedance and current-voltage curves, as methods used to illustrate the ion transport across the membrane.

Proton Exchange Membranes

After the petrol crisis and pollution, problems deriving from the use of petrol derivatives, fuel cells (FCs) and artificial photosynthesis gained an important place in development of green energy¹⁻³. The FCs are devices able to convert the chemical energy of a fuel to electric current and it is common to use fuels coming from renewable sources. The second system uses photo-processes to produce simple organic compounds or hydrogen, which can be used as a fuel for electricity production.

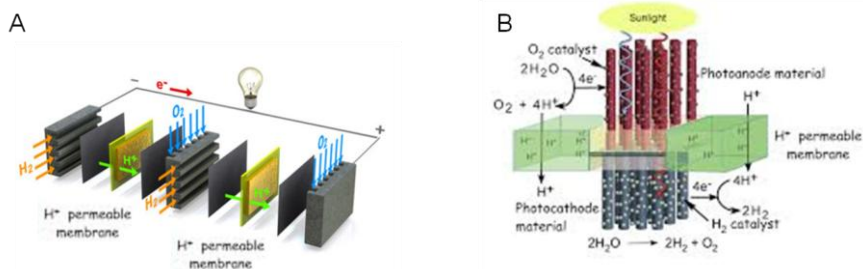


Figure 2.1. Diagram presenting hydrogen fuel cell (A) and artificial photosynthesis (B).

In both cases, the proton exchange membrane (PEM) is a key part, whose development is of great interests of active research in commercial, government, and academic institutions. A proton exchange membrane (or polymer electrolyte membrane) is a semipermeable membrane, typically made of an ionomeric polymer. This polymer should be electrically neutral and contain ionised units allowing ion exchange. One of the crucial parameters of a PEM is the ability to conduct protons through the membrane in a selective manner. This parameter is undoubtedly affected by different factors like the chemical structure and morphology of the membrane. Understanding the influence of these properties on proton conductivity is essential, not only to understand PEMs in general, but also to obtain more effective methods for establishing new materials⁴. Currently, most researchers are focused on acid-doped proton exchange membrane^{5,6}. Considering the structure of the acid-enriched polymers a distinction can be done, depending on whether the acidic groups are incorporated covalently or by other bonding. For doping two acids sulphuric and phosphoric, are most commonly used to improve proton conductivity of polymeric membranes.

The sulfonated polymers (Figure 2.2) are the example of covalently bonded acid, from where the sulfonated polytetrafluoroethylene (that is Nafion from DuPont Co) is the industrially most often used material. Membranes prepared from these material show excellent ionic properties and remarkable proton conductivity in hydrated state; additionally, they present good mechanical and physico-chemical properties. However, the disbenefits derived from water dependent proton conductivity limit their applicability^{7,8}. This important issue influencing the ion and small molecule permeability, and was the driving force for development of new sulfonated polymers⁵ and their modifications⁹⁻¹¹ in order to find materials less affected by hydration.

An alternative to sulfonated materials are phosphoric acid-doped polymers. This new polymers demonstrate interesting electrolytic properties at higher temperatures; the phosphoric acid can be incorporated in polymer both by covalent or by ionic bonding like in nata-de-coco¹² and in polysulfone-based polymers¹³ respectively. Figure 2.3 shows examples of imidazolium pendants with polysulfonic main-chain as an example of ionic interactions between the polymer and the acid.

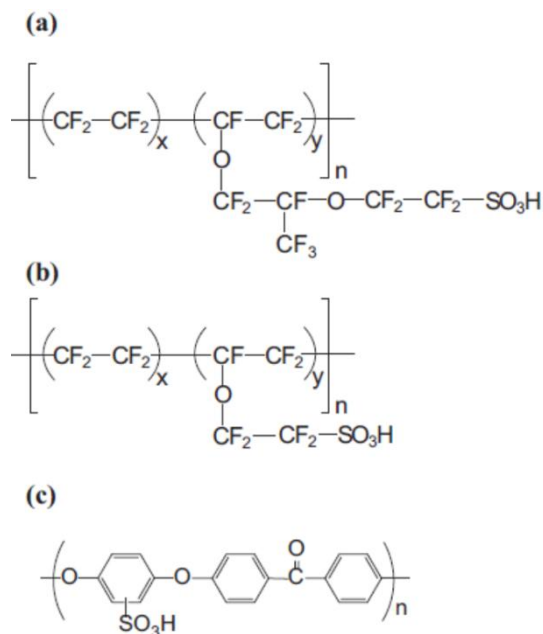


Figure 2.2. The chemical structures of sulfonated polymers: a) Nafion®, b) Aquivion® and c) SPEEK⁵.

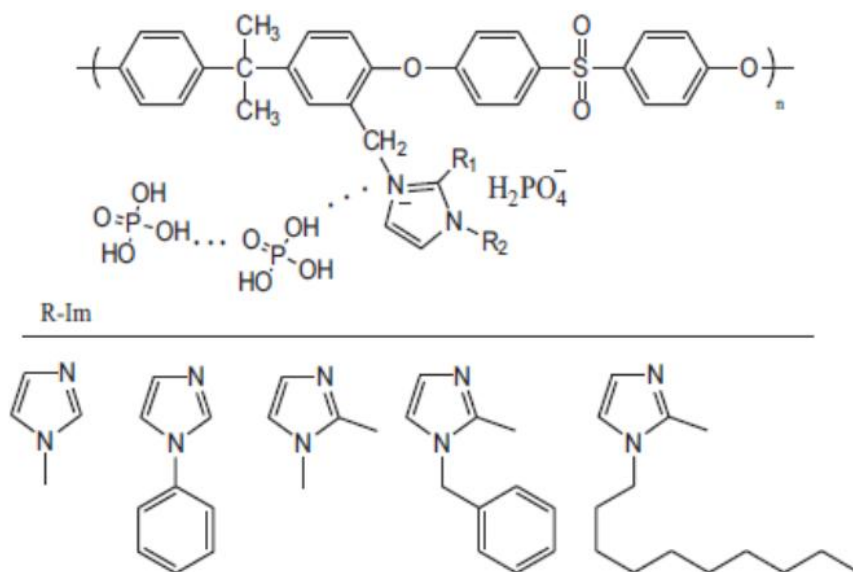


Figure 2.3. Schematic illustration of phosphorus acid doped imidazolium polymers¹³.

Proton Transport

Proton transport can occur by diffusion (bulk) and active (surface) transport (Figure 2.4). The active kind of conductivity is also water-dependent and requires active acidic group inside the channels. Sulfonated membranes are the example of materials with this kind of transport (for example, Nafion by DuPont). They are characterised by high proton conductivity *by means of* their saturation with water.

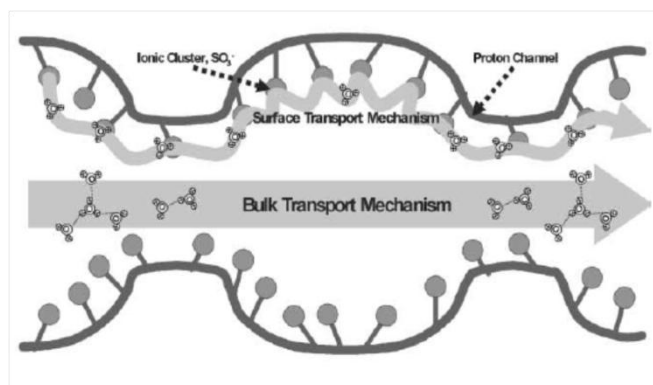
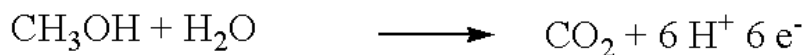


Figure 2.4. Schematic illustration of ion transport inside a Nafion channel¹⁴.

However, there are some disadvantages making them impossible to apply for all kind of FC systems. The proton conductivity increases, in such material, because of increasing sulfonation degree. When the membrane reaches the highest possible level, starts to swell dramatically under hydrated conditions, while it is brittle in dry state. For systems based on methanol as a fuel, like DMFCs, large swelling results in its high crossover. The methanol, which passes across the membrane, will be oxidised on cathode according to the reaction:



This causes loss of energy, thus FC works inefficiently. A compromise between hydrolytic and oxidative stability of membrane has not been achieved yet and in some cases there are still some issues to be addressed^{7,15}.

Another concept in the preparation of proton exchange membranes are polymers with proton donors and acceptors. They are synthesised by combining a polymer with N-groups as proton acceptors

and sulphuric acid groups as proton donors (e.g., Nafion–polybenzimidazole composite membranes)¹⁶. This modification gives mobility of proton ions in matrix without solvating water.

Efficient proton conductivity could be obtained by biomimetic ion-channels. The natural systems from ages inspires human, who tried to copy ideas to reach civilisation progress¹⁷. Nature gives several possibilities to form selective proton pathways; human successfully copied some of them: for instance, ionic gates¹⁸ and well-defined self-assembled structures¹⁹.

The self-assembling strategy was applied for polymers showing benefit for investigation of ion conductive materials. Percec and co-workers, as one of the first researchers, merged this approach with knowledge about liquid crystals to design and synthesise series of liquid crystalline macromolecules and polymers, which self-assembled into columnar structure (Figure 2.5)^{20,21}. The process of self-organization was achieved, using disc-like dendritic group linked to a core, which can be a short chain, smaller discotic molecule or polymeric chain; because of almost a plane form and big dimensions the dendrons will preferably form the outer part of a column as a result of exo-recognition. An illustration of self-assembling of LCs is presented in Figure 2.5.

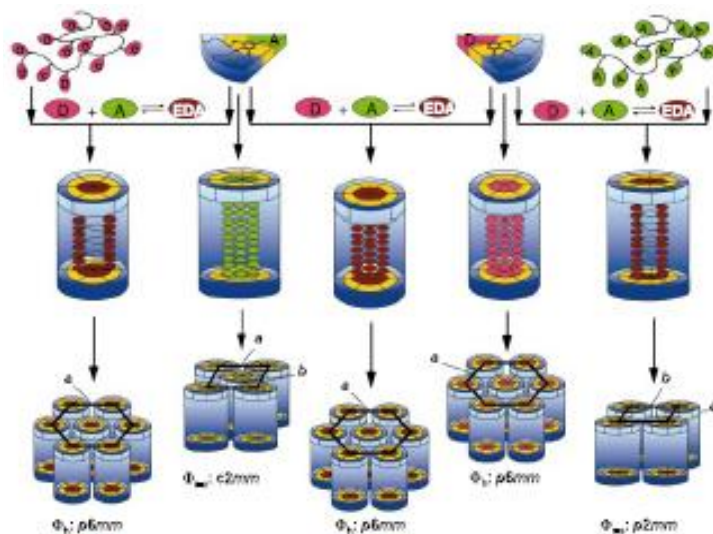


Figure 2.5. Schematic illustration of self-assembling process of liquid crystals into columns with different packing²¹.

It is expected that the main-chain of the polymer, containing electro-donor atoms like oxygen, will form the in the internal part of the column suitable for cation transport.

The work on the subject was continued and implemented in membrane science by Tylkowski and the others. In this article poly(epichlorohydrin) was dendronized with 3,4,5-tris[4-(n-dodecan-1-yloxy)benzyloxy] benzoate in lateral position and used to form ionic channels able to transport protons. The ability to form columnar structure was possible due to exo-recognition of mesogenic groups to form outer surface of the structure. The ion proton transport across the membrane in direction of thickness was noted for membranes with polymeric columns oriented homeotropically²². A similar research on the subject was recently published by Montané et al., where a polyglycidol-based polymer, because of a specific thermal treatment, led to formation of columns aligned perpendicular to the surface; in this system the ion transport was also observed²³.

References

- (1) Kordes K., Simader G., Fuel Cells and their Application, Weinheim, 1996.
- (2) Listorti A., Durrant J., Barber J. Nature Materials, 2009, 8, 929-930.
- (3) Armand M. Endres F., MacFarlane D.R., Ohno H. and Scrosati B., Nature Materials, 2009, 8, 621-629.
- (4) Wilkinson D.P., Zhang J.Z., Hui R., Fergus J., Li X., Proton Exchange Membrane Fuel Cells. Materials Properties and Performance, CRC Press, 2010.
- (5) Ohira, A., Kuroda S., European Polymer Journal, 2015, 67, 78-87.
- (6) Grigoriev S. A., Journal of Fuel Cell Science Technology, 2015, 12, 031004.
- (7) Manea C., Mulder M., Journal of Membrane Science, 2002, 206, 443.
- (8) Park, C.H, Lee C.H., Guiver M.D., Lee Y.M., Progress in Polymer Science 2011, 36, 1443-1498.
- (9) Lue, S. J., Pai Y.-L., Shih C.-M., Wu M.-C., Lai S.-M., Journal of Membrane Science 2015, 493, 212-223.
- (10) Zhang, S., He G., Zhu X., Wu X., Sun X., Zhao X., Li H., Journal of Membrane Science 2015, 493, 58-65.
- (11) Feng K., Tang B., Wu P., Journal of Material Chemistry A, 2014, 2, 16083-16092.
- (12) Radiman, C.L., Rifathin A., Journal of Applied Polymer Science 2013, 130, 399-405.
- (13) Yang, J., Wang J., Liu C., Gao L., Xu Y., Che Q., He R., Journal of Membrane Science 2015, 493, 80-87.
- (14) Tung, S.-P, Hwang B.J., Journal of Material Chemistry, 2005,15, 3532-3538.
- (15) Peckham T.J., Holdcroft S., Advanced Materials, 2010, 22, 4667-4690.
- (16) Ainla A., Brandell D., Solid State Ionics, 2007, 178, 581-591.

- (17) Zhao Y., Sakai F., Liu Y., Wei K., Chen G., Jianh M., *Advanced Materials* 2013, 25, 5215-5256
- (18) Xiao, K., Xie G., Li P., Liu Q., Hou G., Zhang Z., Ma J., Tian Y., Wen L., Jiang L., *Advanced Materials*, 2014, 26, 6560–6565.
- (19) Wegst U.G.K., Bai H., Saiz E., Tomasia A.P., Ritchie R.O., *Nature Materials*, 2015, 14, 23–36.
- (20) Percec V., Schlueter D., Ungar G., Cheng S.Z.D., Zhang A., *Macromolecules* 1998, 31 (6), 1745-1762.
- (21) Percec V., Glodde M., Bera T., Miura K.Y., Shiyonovskaya I., Singer K.D., Balagurusamy V.S.K., Heiney P.A., Schnell I., Rapp A., Spiess H.-W., Hudson S.D., Duan H., *Nature* 2002, 417, 384-387.
- (22) Tylkowski B., Castelao N., Giamberini M., Garcia-Valls R., Reina J.A., Gumí T., *Materials Science and Engineering C*, 2012, 32, 105-111.
- (23) Montané X., Bhosale S.V., Reina J.A., Giamberini M., *Polymer*, 2015, 66, 100-109.

Chapter 4

Applying Nature's Genius to Discotic Liquid-crystal Polymers for Proton Conducting Membrane

Suryakant Vilasrao Bhosale, Krzysztof Artur Bogdanowicz, Yun Li,

Ivo Vankelecom, Ricard Garcia-Valls, José Antonio Reina

and Marta Giamberini

UNIVERSITAT ROVIRA I VIRGILI
LIQUID CRYSTALLINE POLYMERS FOR SMART APPLICATIONS.
Krzysztof Artur Bogdanowicz
Dipòsit Legal: T 1677-2015

Chapter 4

2.4.1. Introduction

The development of intensive global markets has entailed a constantly increasing demand on fossil fuel. Due to this tendency, questions have arisen in relation to energy stability and climate changes and alternative technologies for energy production have received a great deal of attention in recent years. Therefore, artificial photosynthesis and polymer electrolyte membrane fuel cells seem appealing as an alternative to the conventional technologies, offering clean, effective and reliable power generation¹⁻³. Those green technologies are able to convert solar or chemical energy into electric current. One of the key element in such systems is a proton conducting membrane⁴. The most often used are the perfluorinated polymers containing proton conducting groups attached *via* side chains, such as Nafion® (DuPont), though Nafion-alike membranes indicate drawbacks such as a dramatic alteration caused by water evaporation and low selectivity⁵.

The biological systems are going towards these expectations providing with numerous examples, where transport occurs mainly in a selective way, not necessarily with the presence of water. Amongst these systems, proteic channels are the most frequently used systems to transport ions through the membranes in the cells. However, the proteic channels are very effective in ion transport through a cell membrane, though inadequate for technological applications, in terms of difficult purification and complex chemical modification. For this reason, different approaches dealing with simple polyether-based structures⁶, channels formed by stacked crown ethers⁷ and oligo(tetrahydrofurane)⁸ were investigated. Nonetheless, some complications, related to the polymer main chain random-coil conformation of polyether, the energy barrier of discontinuous transport between piled crown ethers and demanding multistep reactions to oligomerize tetrahydrofurane were observed.

One more example found in the nature, related to the self-assembling of the Tobacco Mosaic Virus (TMV) was investigated by Klug in 1983⁹. The TMV self-assembles upon the mixing of its individual components, leading to a cylindrical structure in which the proteins organise in a regular helical array by the exo-recognition of the proteins tapered shape, and force the RNA to adopt a helical conformation in the inner part of the structure.

The first examples of arrangement by the exo-recognition of a polymer containing tapered minidendritic side groups that self-assembled intramolecularly in cylindrical macromolecules, which subsequently self-organized in hexagonal columnar lattices, were discovered and reported

Chapter 4

by Percec et al in 1991¹⁰. It was also demonstrated that the structure assembled into ionic channels and conductivity enhancement along those ion-passages was reported. The ion-channels core were formed by crown-ethers and oligo(ethylene oxide), which were organised in a hexagonal columnar bidimensional lattice^{11,12}. Furthermore, the shape depends of the supramolecular architecture on the molecular taper angle and an increased ionic conductivity in other liquid crystalline states were disclosed¹³.

Recent research delineated two types of one-dimensional ion-conductive polymer films containing ion nanochannels, based on the photopolymerization of aligned columnar liquid-crystals, that is fan-shaped imidazolium salts having different acrylate groups at the periphery¹⁴. In the columnar structure, the ionic section self-assembles into the inner part of the column. Ionic conductivity was measured for the films with columnar orientation, perpendicular (homeotropical) and parallel to the surface. The film with the columns oriented homeotropically to the surface shows higher anisotropy of ionic conductivities than that of the film with the columns aligned parallel to the surface.

Moreover, some scientists proposed different synthetic biomimetic transport approaches, for instance, 'ion-transporting molecular cable' and 'proton-conductive materials formed by the self-organization' introduced by Bennin et al and Ueda et al respectively^{15,16}.

In our present work, we synthesised side-chain liquid crystalline polyethers dendronized with potassium 3,4,5-tris[4-(n-dodecan-1-yloxy)benzyloxy]benzoate. The synthesis was performed according to the procedure described by Ronda et al¹⁷ with some modifications. The structure of the polymers was designed to self-assembly into columns, which should be subsequently homeotropically aligned. In our case, orientation plays a crucial role in ion transport across the membrane, since it promotes an ion passageway formation. The proper alignment of columns perpendicular to the surface was achieved by applying a thermal treatment. It was proved that under moderated conditions of temperature and humidity, the polymeric membranes showed water-independent proton conductivity comparable to Nafion. Ion size-dependent transport was also observed in permeability tests in aqueous solution.

Chapter 4

2.4.2. Materials and Methods

Materials

Inorganic and organic compounds were provided from Sigma-Aldrich and Fisher Scientifics, and used as received. For all experiments, which required water or aqueous solutions, Mili-Q water was used.

Potassium 3,4,5-tris[4-(n-dodecan-1-yloxy)benzyloxy]benzoate. The potassium 3,4,5-tris[4-(n-dodecan-1-yloxy)benzyloxy]benzoate was synthesised according to procedure reported by Suryakant Bhosale¹⁸.

Polymers. The structures of the studied polymers are reported in Figure 2.4.1. The polymers were obtained *by means of* the modification of poly(epichlorohydrin) (PECH) and poly(epichlorohydrin-co-ethylene oxide) (P(ECH-co-EO)) (50:50) by the dendron potassium 3,4,5-tris[4-(n-dodecan-1-yloxy)benzyloxy]benzoate, to obtain columnar mesophases. Anhydrous THF as a solvent, stoichiometric amounts of TBAB, the reaction duration of 8 days and 65°C were selected in all cases. In order to obtain a higher degree of modification, the concentration of PECH in the solution was increased from 0.083 M to 0.1 M and also the amount of the tapered group was increased by 4, compared with the previous report.¹⁷ Moreover, the temperature was increased from 60 to 65°C. In the study two modifications from each family were selected: 63% modified **HP1** and 72% modified **HP2** were selected from PECH family, while 59% modified **CP1** and 69% modified **CP2** were selected from P(ECH-co-EO) family (Figure 2.4.1). The clearing temperatures for all polymers are presented in Table 2.4.1.

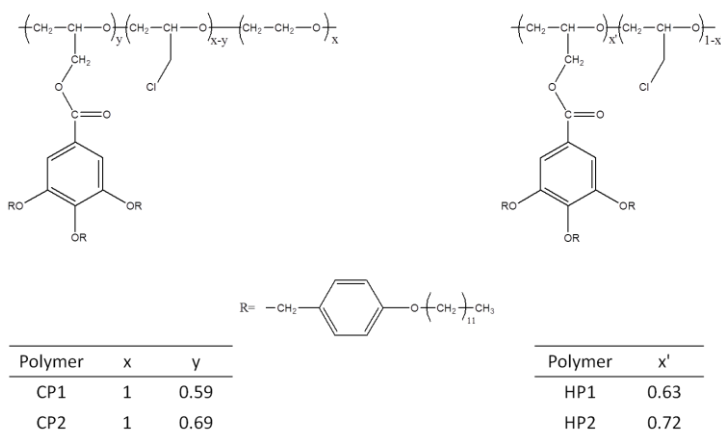


Figure 2.4.1. The structure of two polymeric families based on poly(epichlorohydrin-co-ethylene oxide), and poly(epichlorohydrin).

Chapter 4

Table 2.4.1. Clearing temperatures for HP and CP polymers

Name	Modification (%)	T _c [°C]
HP1	63	116 ^a
HP2	72	142 ^a
CP1	59	85-90 ^b
CP2	69	115-118 ^b

^a determined from second heating scan

^b determined by POM

Membrane Preparation

Supports. Teflon- Teflon support, with a thickness 0.2 mm, was purchased from Servisio Estación S.A. (Barcelona). The support before being used was washed with acetone and air-dried.

Hydrophilic glass- The glass plates were immersed in a piranha solution (3:7 v/v of 30% H₂O₂ and H₂SO₄) for 5 min. Next the substrate was washed, in the following exact order, with water, acetone and methanol, and dried. The hydrophilicity of the treated glass was confirmed by contact angle (CA) measurements (CA before treatment: 49.1°; after treatment: 38.1°).

Immersion Precipitation. A 30% solution (w/w) of polymer in THF was prepared and spread with a casting machine (K paint applicator, RK Paintcoat Instruments Ltd., United Kingdom) onto a treated glass surface or a teflon sheet with a controlled thickness (gap size 300 μm). Later, the support with a wet film on top was immersed in a bath of Milli-Q water. After which, a polymer dense membrane with a thickness of approximately 200 μm was formed and peeled off from the support.

Vapour Precipitation. A polymeric solution, similar to the immersion precipitation, was placed onto a treated glass support. Afterwards, the wet film was placed in a chamber with stable conditions of 20°C and 95% humidity. The sample was kept inside until the full precipitation of polymer occurred.

Thermal Treatment (baking process). A teflon-supported membrane was prepared by immersion precipitation as described above. Then placed on a Linkam TP92 hot stage and heated above the polymer clearing temperature, after that being slowly cooled (0.5°C/minute) to room temperature. Subsequently, the membrane was kept at room

Chapter 4

temperature for approximately 1-hour and then separated from the teflon sheet. An intact and uniform membrane was obtained as is shown in Figure S2.4.1. This process was tested on a hydrophilic substrate that is treated glass, with the same results.

Shearing Process. HP1 was mechanically oriented by shearing at temperatures slightly below its clearing temperature on a silicon single crystal wafer surface cut parallel to the plane (510). The direction of shearing was in the xy plane.

Characterisation

Transmission Electron Microscopy (TEM). The samples were cooled with liquid nitrogen to the cutting temperature of -60°C to prevent deformation of the original microstructure. A cutting speed of 0.1 mm/s was used to obtain samples with thickness of 50 nm. The samples were placed on carbon coated-copper grids.

The ultramicrotomed samples were then stained dark by exposure to the ruthenium tetroxide vapours for 5 minutes to incorporate high atomic number atoms in the membrane. The staining provides a better contrast between the phase domains in the TEM analysis, which was carried out with a JEOL 1011 Transmission Electron Microscope with a voltage of 80 kV.

The photomicrographs, obtained by TEM, were scan photocopied, after which the images were treated using the Adobe Photoshop 6.0 software program. The measurements of structures observed in the morphology were determined using the Image-Pro Plus version 1.48 software.

Contact angle (CA). The static contact angles with water on a membrane surface were measured with a Dataphysics OCA 15EC contact angle instrument (Filderstadt, Germany) equipped with a motorized pipette and deionised water as the probe liquid. The contact angle was measured immediately after placing the water drop (3 μL) on the membrane surface. The measurements were repeated using different areas of the film: for each test reported, at least three drops of water were used.

X-Ray diffraction (XRD). The XRD measurements were taken using a Bruker-AXS D8-Discover diffractometer equipped with parallel

Chapter 4

incident beam (Göbel mirror), vertical θ - θ goniometer, XYZ motorized stage and with a GADDS (General Area Diffraction System). The samples were placed directly on the sample holder for a reflection analysis. For samples oriented by shearing a low background Si(510) sample holder for reflection analysis were used. An X-ray collimator system close-to-the-sample allows analyzing areas of 500 μm . The X-ray diffractometer was operated at 40 kV and 40 mA to generate $\text{CuK}\alpha$ radiation. The GADDS detector was a HI-STAR (multiwire proportional counter of 30x30 cm with a 1024x1024 pixel) placed at 30cm from the sample. The X-ray beam hit the sample at 0.5° of incidence. The collected frame (2D XRD pattern) covers at such distance a range from 0.9 up to $9.2^\circ 2\theta$. The diffracted X-ray beam travels through a He beam path (SAXS attachment) to reduce the air scattering at low angles. The direct X-ray beam is stopped by a beam stop placed directly on the detector face. The exposition time was of 300s each frame.

Atomic Force Microscopy (AFM). The AFM images were recorded with an Agilent 5500 Environmental Atomic Force Microscope (Agilent Technology) equipped with an extender electronics module, which enables phase imaging in a Tapping Mode. All images were recorded in a tapping mode using: Multi 75 and AHR150-15 (BudgetSensors) silicon cantilever (thickness = 3 μm and 1nm, respectively) with a force constant at 3 N/m and a resonance frequency of 75 kHz and 150 kHz, respectively, and an extra-thin cantilever tip (Hires_C19/Cr-Au, MicroMasch, having a resonance frequency of approx.60 Hz and. The scan rate was typically 0.7–2 Hz. All images ($1 \times 1 \mu\text{m}$) were measured at room temperature, in unfiltered air. The microscope was placed on an active vibration isolation chamber (Agilent Technology), which was further placed on a large sturdy table to eliminate external vibration noise. The Nanotec WSxM 5.0 Develop 4.0 Image Browser Scanning Probe Microscopy23 was used for the roughness analysis of the images.

Inductively coupled plasma mass spectrometry (ICP-MS). The determination of sodium was carried out using inductively coupled plasma mass spectrometry by Thermo Elemental (Mod. XSeries II, Bremen, Germany). Each sample was analyzed three times using ultrapure commercial standard solutions (Merck, Darmstadt, Germany and J.T. Baker, North Kingstown, RI, USA). Sc, Y, Ir and Rh were used as internal standards. The original samples were diluted to reach a measuring range of ICP-MS.

Permeability tests. The transport experiments were performed using a teflon test cell that consisted of two compartments, separated by

Chapter 4

the tested membrane, containing the feed and the stripping solutions, respectively. The feed and the stripping volumes were 200 ml and the effective membrane area was 0.86 cm². For the proton transportation experiments, the initial feed solution was 0.1 M HCl aqueous solution and the stripping solution 0.1 M aqueous solution of corresponding salt: LiCl, NaCl or KCl. The pH of the stripping solution was measured every 10 s by an Orion Dual Star pH/ISE Multimeter. All experiments were repeated three times. The calculations of the proton permeability were carried out in accordance with the equations:

Under steady-state conditions, proton flux was calculated by Fick's First Law:

$$J = \frac{P\Delta C}{l} \cdot 10^{-3} \quad (1)$$

where l (cm) is the membrane thickness and ΔC is the difference in concentration (mol l⁻¹) between the initial feed solution (C_0) and the final stripping solution. In our experimental conditions, C_0 was much greater than the final stripping concentration, so we considered $\Delta C \sim C_0$.

P is the proton permeability (cm² s⁻¹), defined as:

$$P = DS \quad (2)$$

where D is the proton diffusion coefficient and S is the sorption equilibrium parameter.

The flux is related to the permeability coefficient p (cm s⁻¹), as:

$$J = pC_0 \quad (3)$$

$$P = pl \quad (4)$$

The permeability coefficient can be described by the following equation:

$$-\ln \frac{C_f}{C_0} = \frac{Ap}{V_f} t \quad (5)$$

Chapter 4

where C_0 (mol l⁻¹) is the initial concentration of the feed solution and C_f (mol l⁻¹) is the feed concentration calculated from the stripping solution at time t (s):

$$C_f = C_0 - C_s \quad (6)$$

V_f is the feed volume (mL) and A is the actual membrane area (cm²).

We calculated the proton permeabilities in accordance with the above equations. Data were fitted according to equation (5) in the time range 30-115 hours.

DSC. Thermal transitions were detected with Mettler-Toledo differential scanning calorimetry mod. 822 in dynamic mode at a heating or cooling rate of 10 °C /min. Nitrogen was used as the purge gas. The calorimeter was calibrated with an indium standard (heat flow calibration and an indium-lead-zinc standard (temperature calibration).

POM. The clearing temperatures were roughly estimated using polarized optical microscopy (POM); textures of the samples were observed with an Axiolab Zeiss optical microscope equipped with a Linkam TP92 hot stage.

Proton conductivity measurements. The proton conductivity of membranes was measured using four-point probe conductivity cell (lab-made conductivity cell was used which was prepared in Centre For Surface Chemistry And Catalysis, Katholieke Universiteit Leuven, Belgium) at RH 5%, 50% and 100% at different temperatures range. In case of HPs, conductivities were measured at 30 °C, 50 °C and 70 °C, while in case of CPs, at 30 °C and 50 °C. Membrane impedance was determined using a M2 Materials Mate's 7260 Impedance Analyser. The impedance analyzer was worked in galvanostatic mode over frequency range from 1 Hz 107 Hz by Nyquist method⁹ using Zscore software. Each sample was cut in 3.14 cm² prior to mounting on the cell. The proton conductivity (σ) was obtained by following formula:

$$\sigma = l/RS$$

where σ is the proton conductivity (S/cm), and l is the thickness of the membrane (cm). R is the membrane impedance (Ω) and S is the surface area for ion to penetrate the membrane (cm²). The impedance of each

Chapter 4

sample was measured five times to ensure data reproducibility and calculate standard deviations.

Electric Resistance. The integral electric resistance of the sample was measured by using a simple sensitive Ohm-meter of Keithley: 199 system DMM/Scanner.

2.4.3. Result and Discussion

Membrane Preparation, Characterization and Permeability

As mentioned previously, our polymeric systems exhibited all a columnar liquid crystalline phase in a wide temperature range and were designed to consist of ion conducting paths having hydrophobic mesogenic side chains and hydrophilic ether linkages in a polymer backbone. In order to get efficient ion transport, it is crucial that the polymeric columns are homeotropically oriented to the membrane surface. Hence, the initial idea was to apply diffusion induced phase separation techniques to obtain oriented membranes on a hydrophilic glass support: the anchoring of hydrophilic ether linkage to the hydrophilic substrate would take place, whilst the mesogenic part would attempt to minimize the contact with hydrophilic non-solvent, which in this case is water. Thereby, considering this possibility, the HP1 polymer was initially used to prepare membranes by immersion and vapour precipitation methods, as explained in the Membrane preparation section. However, these attempts proved unsuccessful: unoriented membranes resulted, as shown by XRD (Figure 2.4.2A,B).

The studies carried out by Percec et al.¹⁹ posed further reflection on how to obtain a homeotropic orientation. For instance, the polymer poly(3',4',5'-tris[4''-(n-dodecyl-1-oxy)benzyloxy]benzylmethacrylate) referred to as G1-PMA, was used to investigate self-assembly in a columnar fashion, which is well organized below and above T_g . According to this research, the polymer backbone does not have a significant influence on the structure adopted by the system. Rather, the aromatic moieties in the dendrons are producing driving forces in the self-assembly process, inducing a helical arrangement. Based on the high degree of local order found within the dendrons, they were identified as the structure-directing moieties of the columnar architecture. In further studies,²⁰ they demonstrated, with the combination of different techniques including DSC, XRD and POM, how these dendrons could self-assemble and self-organize into hexagonal columnar and rectangular columnar

Chapter 4

liquid crystals. Combining the NMR information with the XRD data, the outcome indicated that this kind of material can be homeotropically oriented when the system is allowed to self-organize during slow cooling on a hydrophobic substrate from the melt, into the liquid crystal and glassy hexagonal columnar phases. π - π stacking of aromatic moieties is responsible for this homeotropic orientation.¹⁹

Therefore, taking into account the structural similarities of the reported polymer to our columnar liquid crystal polymers, a new technique, namely *baking process*, was unearthed. This treatment basically includes the heating of the polymer film above its clearing temperature and subsequent cooling to room temperature at a very slow rate. This method was tested to prepare membranes out of different polymers as well as on treated glass or teflon supports.

Hence, to induce the wanted organisation, the *baking process* was applied to membranes obtained by phase inversion precipitation. A homeotropically oriented columnar structure was obtained in the case of both homo- and copolymers. As an example presented in Figure 2.4.2C, the XRD pattern of HP1 showed a well defined signal at $2\theta = 2.2^\circ$, well polarised at the equator as shown from the maximum around 90° in the Phi diffractogram.

In order to quantify column orientation, the width at half height (WHH) of the peak obtained from the azimuthal scan of the reflection at 2θ around 2° (corresponding to the intercolumnar distance) was calculated and it is shown in Table 2.4.2 for different polymers and supports.

Results from Table 2.4.2 clearly show that satisfactory homeotropic orientation was achieved both in the case of baking process performed on a hydrophilic (treated glass) and on a hydrophobic substrate (teflon sheet), since very close WHH values and the same orientation angles resulted. Since the nature of the support does not seem to play a crucial role in the orientation process, this suggests that the hierarchical structures in HP and CP polymers tend to form down from the top surface. This could depend on the dendrons anchoring to the air interface: the aliphatic tails present in the dendrons, which are more mobile and possess low surface energy, would favour the dendrons moving toward the air interface over the main chain components, due to their higher air compatibility and entropy. An analogous behaviour was recently found in the case of nanocylinder orientation of a liquid crystal block copolymer

Chapter 4

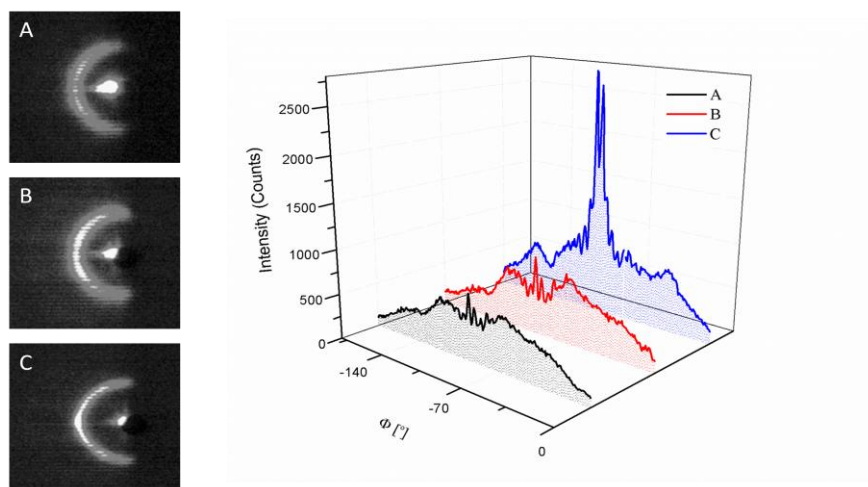


Figure 2.4.2. XRD analysis- Debye ring pattern (left side) and Phi diffractogram from azimuthal scan on the reflection at $2\theta = 2.2^\circ$ or 2.1° (right side), of HP1 polymer membrane prepared by immerse precipitation (A), vapour precipitation method (B) and membrane after baking process on a teflon sheet (C).

Table 2.4.2. Calculated peak width at half height (WHH) and angle of orientation of membranes prepared by baking process out of different polymers on treated glass or teflon supports.

Sample, support	WHH ($^\circ$)	Angle of orientation ϕ ($^\circ$)
HP1, teflon	11	89
HP1, glass	9	89
HP2, teflon	12	90
HP2, glass	10	89
CP1, teflon	6	91
CP1, glass	7	91
CP2, teflon	9	88
CP2, glass	8	89

Chapter 4

film, based on poly(ethylene oxide) and a polymethacrylate bearing azobenzene mesogen side chains²¹.

Therefore, the nature of the supporting material did not influence the degree of order in the final membrane; hence, since the membranes could be more easily peeled off the teflon support than the glass one, samples prepared by baking on a teflon sheet were selected for further studies.

Thermally treated and untreated polymeric membranes were investigated in terms of water contact angle (CA) measurement. As an example, HP1 and CP2 polymers were employed. CA tests were performed both on the teflon-side and air-side, i.e., the part which was directly in contact with the teflon support during the baking process, and the air-exposed side. The results of CA tests are shown in Table 2.4.3.

Table 2.4.3. Water contact angles of untreated and thermally treated HP1 and CP2 polymers

Sample	Modification (%)	Angle [°]
HP1	63	71 ^a , 97 ^b
CP2	69	85 ^a , 133 ^b

^a untreated sample

^b after Baking process

Both sides of the treated membranes were hydrophobic, having similar contact angles (Table 2.4.3), whereas untreated samples resulted more hydrophilic. Hence, the thermal treatment results in the enhancement of the membrane surface hydrophobicity, which is related to the oriented structure. These data seem to confirm that the orientation process is driven by the dendrons anchoring to the air surface: for this reason, the tapered groups, that represent the hydrophobic part of the polymer, are more exposed than the hydrophilic part in the oriented membrane²². The disparity of the angle values between the HP1 and CP2 may be the result of the slightly higher orientation of CP2 copolymer (Table 2.4.3) which, in turn, can be attributed to its higher flexibility.

Oriented membranes were also studied in terms of surface analysis by AFM; for the sake of comparison, AFM was also performed on one of the homopolymers (HP1) unoriented and in-plane oriented by shearing.

For all the homeotropically oriented samples, a fingerprint-like pattern was observed in the phase image. In the case of HP1 (Figures 2.4.3 A,B), this image looked extremely homogeneous on both membrane

Chapter 4

sides. Root-Mean-Squared (RMS) roughness was calculated from topographic images (Figures 2.4.3C, D) and gave low values, 10.2 nm (Teflon side) and 8.0 nm (air side), respectively. The XRD pattern of the oriented HP1 (Figure S2.4.2A) shows a single sharp peak at $2\theta = 2.1^\circ$ ($d_{100} = 39.3 \text{ \AA}$). This information, combined with the AFM results, suggests that homeotropically oriented HP1 exhibits a columnar lamellar mesophase, with the lamellas aligned perpendicular to the membrane surface²³. Actually, the lamellar thickness, as measured by AFM, resulted in approximately 40 \AA , which is in agreement with the value of the d_{100} spacing calculated from XRD. Similar results were found for HP2 copolymer.

Differently, in the case of the oriented CP1 AFM phase image, it seemed like overall surface area was not showing uniform fingerprint-like structure (Figure 2.4.4A); the calculated RMS roughness resulted 4.3 nm (air side) and 9.1 nm (Teflon side). On the other hand, for this sample XRD pattern (Figure S2.4.2B) exhibited three sharp reflections, in the ratio $1 \div 1/\sqrt{3} \div 1/2$, which correspond to d_{100} , d_{110} and d_{200} of a hexagonal columnar phase. Hence, for CP1 the evidences from XRD and AFM suggest a coexistence of lamellar columnar and hexagonal columnar structure in the oriented membranes. Again, this can be ascribed to higher flexibility of CP copolymers: in fact, in this case the homeotropic orientation of the columns does not prevent them from a local organisation into more ordered Φ_h mesophase.

Although, in the case of the unoriented and shear-oriented membranes, no such lamellar organisation can be guessed from their respective the phase images (Figure S2.4.3A and S2.4.3B): this suggests that homeotropic orientation prompts a lamellar columnar structure in the membranes.

Preliminary tests were performed on the homopolymer HP2 in relation to the proton transport process phenomena. For this reason, a set of permeability experiments was carried out using hydrochloric acid as the feed phase, while the stripping phase contained three different selected monovalent alkaline cations: Li^+ , Na^+ and K^+ alternatively, in the form of chloride. The obtained results (Table 2.4.4) show that the highest permeability value was obtained for sodium cation, while no proton transport was detected at all when potassium ion solution was forming the stripping phase. It is noteworthy that no permeability at all was detected for the unoriented samples.

Chapter 4

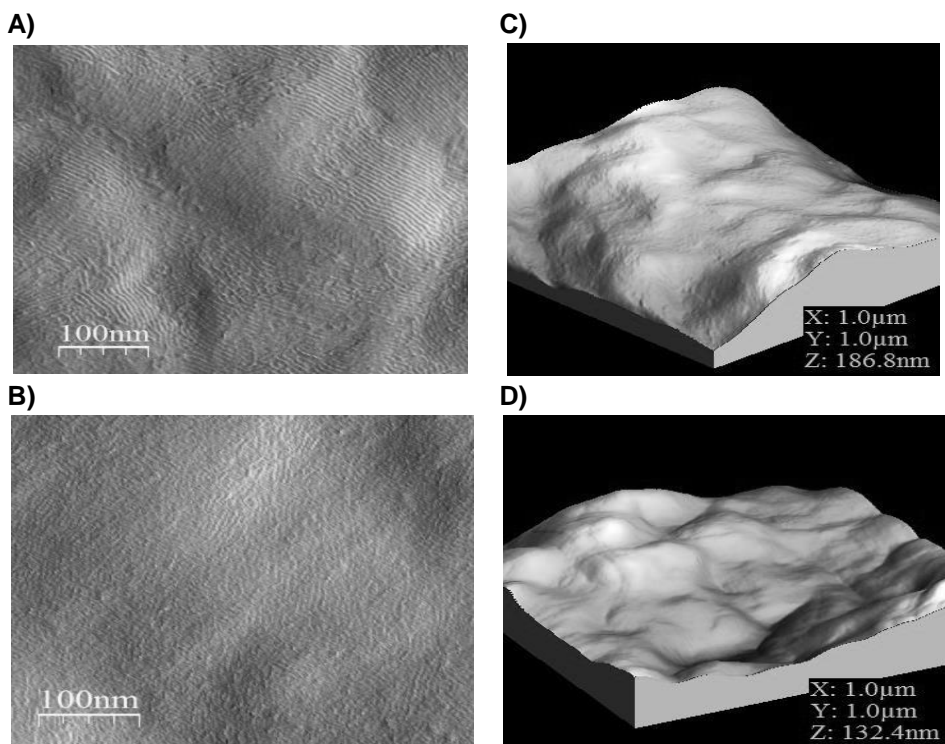


Figure 2.4.3. AFM phase image pattern of oriented membranes of HP1 prepared on teflon: A) air side B) teflon side, and corresponding topographic image patterns C) air side D) teflon side.

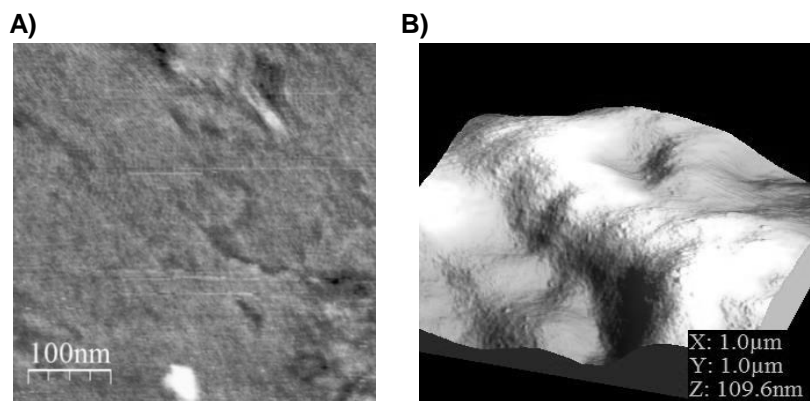


Figure 2.4.4. AFM phase image pattern of oriented CP1 membrane (A) and corresponding topographic image pattern (B).

Chapter 4

Under the hypothesis of cation antiport mechanism, proton transport in these experiments should be limited by the stripping cation permeability, which, in turn depends on the size of the polyether ion channel. Lower permeability for Li^+ could be because of a poor coordination of this cation to the hypothesised polyether channel, which is responsible for the transport. In the case of K^+ , one can suppose that the cation size is too big for the transport to occur in the oriented channels. Therefore, these materials could also be selective to cations according to their size.

Table 2.4.4. Proton permeability of HP2 oriented membranes when different cations solutions are forming the stripping phase.

Cation in stripping	Proton Permeability [$\times 10^7 \text{ cm}^2 \text{ s}^{-1}$]
Na^+	5.6 (± 0.1)
Li^+	3.7 (± 0.3)
K^+	not detected

Additionally, in the case of the experiments performed with sodium, the variation of Na^+ concentration was determined by ICP-MS in the feed compartment, at the start-up time and at the end of the experiment. As consequence to its transport a variation of proton concentration in the stripping compartment was noticed. Within the experimental error, the variation was found to be equal, with values of 11,43(± 0.01) ppm for $\Delta[\text{H}^+]$ and 12(± 1) ppm for $\Delta[\text{Na}^+]$. Hence, both reported experimental evidences suggest a cation antiport mechanism for transport in oriented HP2 membranes.

A structural study was performed on the HP2 membrane after the permeability test, in order to clarify whether transport may affect the polymer organisation. The XRD analysis of a sample after the experiment with lithium in the stripping compartment (Figure S2.4.4) did not show any changes with respect to a fresh oriented sample. In the 2theta diffractogram only one reflection could be observed at $2\theta = 2.1^\circ$, $d = 39.3 \text{ \AA}$. On the other hand, a remarkable change in the superficial structure was visible from the AFM analysis (Figure 2.4.5, top). In the phase image, well-defined aggregations can be distinguished, which in the topography appear as hills, whose diameter is roughly 50 nm; hence, they may correspond to columnar clusters. RMS roughness resulted extremely low, that is 0.9 nm.

Chapter 4

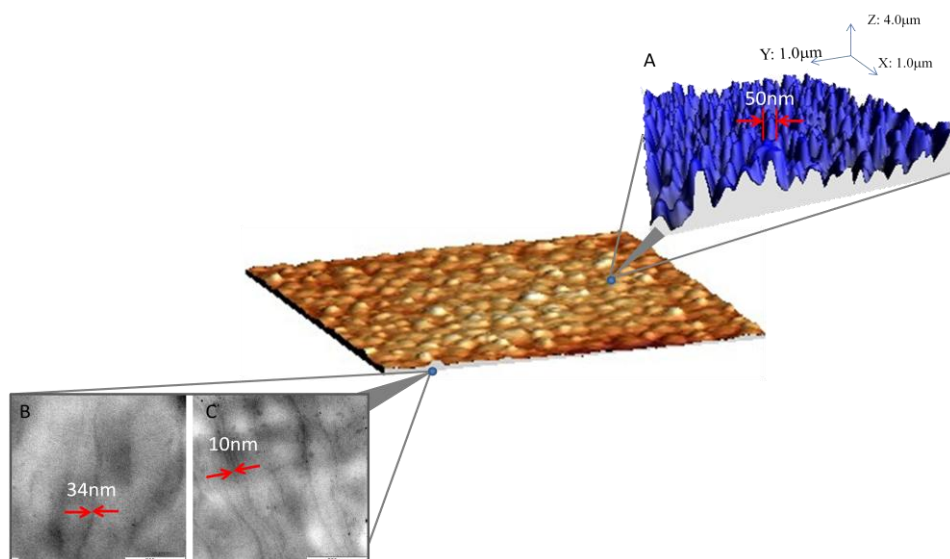


Figure 2.4.5. Structural analysis of a HP2 membrane after permeability with Li^+ . Top: the AFM surface topography image with indication of hills diameter; bottom: TEM image before (left) and after (right) staining with RuO_4 .

TEM analysis was also performed on the cross-section of HP2 membrane after lithium transport experiment.

As it can be seen in Figure 2.4.5 (bottom left), a striped cross-section surface can be guessed from TEM image. When the sample was stained 5 minutes with RuO_4 vapours, to improve the contrast between the organised aromatic portions and the amorphous regions of the membrane²⁴, the stripes turned definitely more evident (Figure 2.4.5, bottom right). A rough estimate of the width of a single stripe gave approximately 10 nm, which is more detailed than in case of unstained samples (single strip width of approximately 34 nm). Therefore, it seems that, favoured by cation passage, oriented polymeric columns tend to form bundles that may constitute actually an "ionic cable".

Membrane Conductivity

Prior to Electrochemical Impedance Spectroscopy (EIS) measurements, the integral electric resistance of the homeotropically oriented membranes was evaluated using sensitive Ohm-meter; no intrinsic electric conductivity was observed, what indicates that the

Chapter 4

samples behave as good dielectrics and the conducting channels are free of any charge, as expected.

The conductivity values of homo- and co-polymers at different temperatures and percentages of relative humidity (RH), obtained from EIS, are given in Table 2.4.5. The RH values equal to 5%, 50% and 100% were used to explore the effect of RH on proton conductivity, while applying different temperatures. A softening of polymers was found to be a limiting barrier to perform the conductivity tests at temperatures above 100°C, although the clearing temperature of polymeric materials was higher than 100°C. It was found that the membranes were able to stand the temperatures up to 50°C and 70°C for CPs and HPs, respectively, above which the material was likely to soften and stuck to the membrane holder of the conductivity cell. Thus, the conductivity experiments were carried out at temperatures 30°C and 50°C in the case of CPs, and at 30°C, 50°C and 70°C in the case of HPs.

Table 2.4.5. Proton conductivity versus temperature and relative humidity for samples HP1, HP2, CP1 and CP2.

Membrane	Relative Humidity [%]	$\sigma \times 10^3$ at 30°C [S/cm]	$\sigma \times 10^3$ at 50°C [S/cm]	$\sigma \times 10^3$ at 70°C [S/cm]
HP1	5	1.6 (± 0.4)	1.9 (± 0.4)	2.5 (± 0.3)
HP2	5	4.1 (± 0.8)	4.2 (± 0.6)	5.1 (± 0.1)
CP1	5	3.5 (± 0.3)	7.3 (± 0.3)	-
CP2	5	8.8 (± 0.7)	14.0 (± 1.5)	--
HP1	50	1.6 (± 0.4)	1.8 (± 0.6)	2.5 (± 0.3)
HP2	50	4.0 (± 0.3)	4.4 (± 0.7)	5.1 (± 0.7)
CP1	50	4.3 (± 0.6)	6.7 (± 0.2)	-
CP2	50	9.2 (± 0.4)	13.0 (± 3.1)	-
HP1	100	1.6 (± 0.6)	1.9 (± 0.5)	2.4 (± 0.5)
HP2	100	4.1 (± 0.2)	4.3 (± 0.4)	5.0 (± 0.2)
CP1	100	4.3 (± 0.2)	7.3 (± 0.2)	-
CP2	100	9.2 (± 0.6)	14.0 (± 2.2)	-

The proton conductivity of the materials increases with the degree of the modification and its higher values were obtained for copolymers in comparison to homopolymers. The difference between both families could be explained by the presence of more flexible ethylene oxide moieties in the polymeric main chain; it facilitates a better orientation of ionic pathways required for proton conductivity. In the case of Nafion 117 the conductivity depends on the humidity and temperature. Its values tend to drop with increment of temperature above 100°C and decrease of relative humidity. The experimental value for this material is 13.25 mS/cm at 30°C

Chapter 4

in 100% RH atmosphere. On the other hand, for the membranes based on the polyether, the highest conductivity was achieved for CP2 and is equal to 8.8 mS/cm at 30°C and 14 mS/cm at 50°C in 5% RH atmosphere in both cases. It can be seen that the proton conductivity values for polyether-based membranes are similar to those obtained for Nafion. Moreover, despite of increment of the relative humidity percentage, the conductivity remains constant. This fact undoubtedly indicates independency of proton conductivity in CPs and HPs from water content, alike Nafion.

2.4.4. Conclusions

Polymeric membranes based on oriented dendronized poly(epichlorohydrin) and poly(epichlorohydrin-co-ethylene oxide) have been investigated applying different preparation methods. Immersion precipitation, vapour precipitation and baking process on different supports were used to homeotropically orient the polymers. Studies showed that the immersion and vapour precipitation failed in aligning the polymers in a homeotropic fashion, whilst the baking process proved its effectiveness to arrange polymeric columns perpendicular to the membrane surface, achieving good reproducibility in all cases. Homeotropic orientation was studied by XRD analysis in reflection mode at small angles of 2θ . The static contact angle measurements disclosed hydrophobic nature of oriented membranes on both sides, where the unoriented ones were hydrophilic. AFM technique revealed a fingerprint-like phase images on both sides of the oriented membrane. These results, together with XRD, give an evidence of arrangement of oriented polymer as columns perpendicular to the membrane surface for HPs, or as both lamellae and columns for CPs. The homeotropic orientation of the ion conducting columns in the membrane resulted in remarkable proton conductivity, in the range of 10^{-2} to 10^{-3} S/cm, independently from the relative humidity.

2.4.5. Acknowledgments

Financial support from Ministerio de Economía y Competitividad (CTQ2013-46825-R) is gratefully acknowledged. The authors are also grateful do Dr. Olivier Henry and Dr. Giulio Malucelli for help with contact angle measurements.

Chapter 4

2.4.6. Supporting information

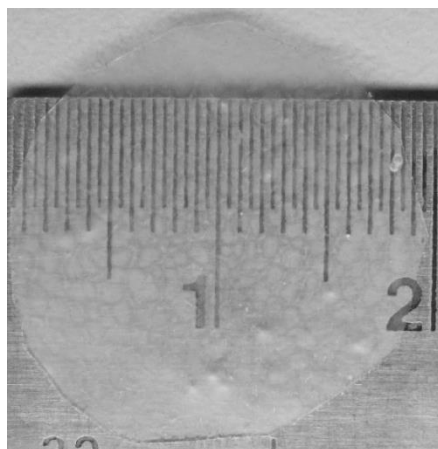


Figure S2.4.1. Oriented membrane of approximately 2 cm diameter obtained by phase inversion precipitation followed by baking process.

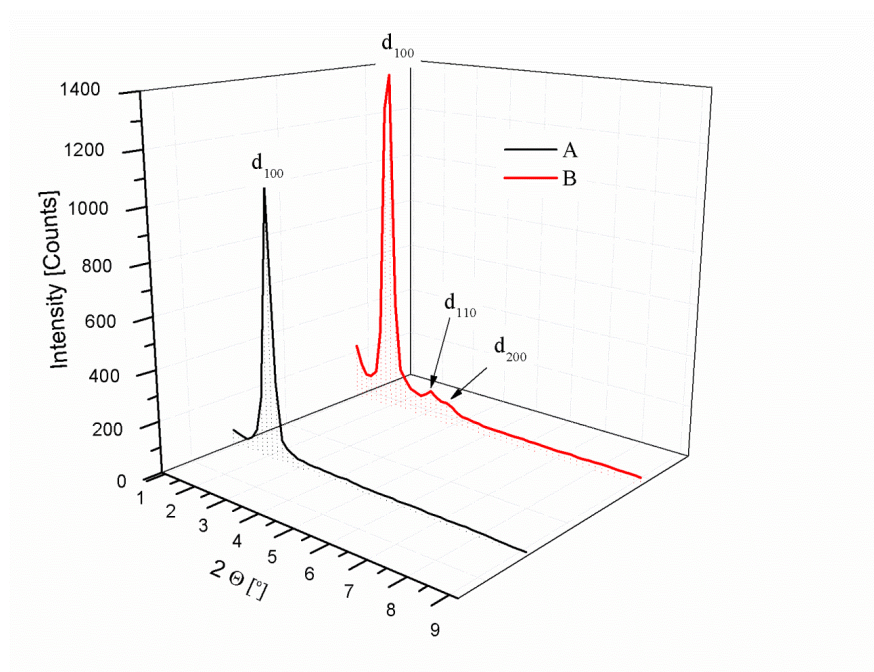


Figure S2.4.2. XRD diffraction pattern of intensity vs 2θ : A- oriented HP1 membrane, B- oriented CP1 membrane.

Chapter 4

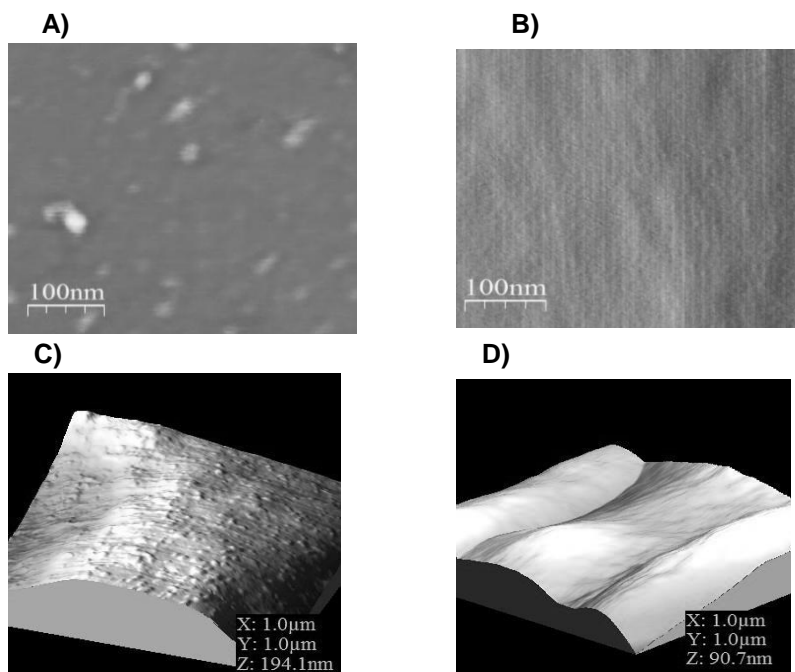


Figure S2.4.3. AFM phase image pattern of surface morphology of HP1 membranes: a) unoriented b) shear oriented, and topographic image pattern of surface morphology of HP1 membranes: c) unoriented d) shear oriented.

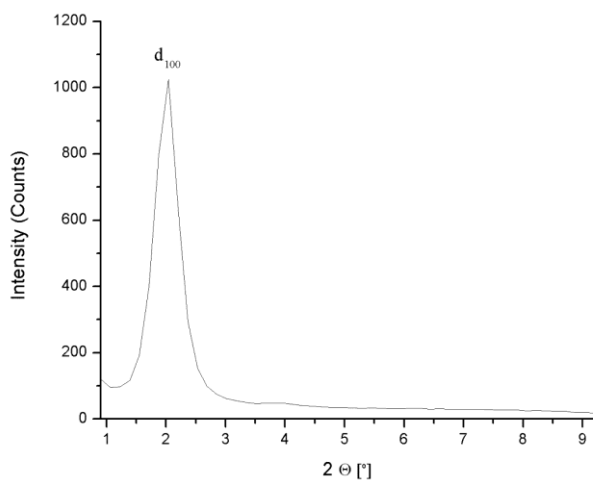


Figure S2.4.4 XRD diffraction pattern of intensity vs 2θ fo HP2 after lithium permeability test.

Chapter 4

2.4.7. References

- (1) Sharma, S., Ghoshal, S. K., *Renewable and Sustainable Energy Reviews*, 2015, 43, 1151-1158.
- (2) Hawkes, A., Staffell, I., Brett, D.; Brandon, N., *Energy and Environmental Science* 2009, 2, 729-744.
- (3) Hwang, J.-J., *Renewable and Sustainable Energy Reviews*, 2013, 19, 220-229.
- (4) Smitha, B., Sridhar, S., Khan, A. A., *Journal of Membrane Science* 2005, 259, 10-26.
- (5) Yang, C., Costamagna, P., Srinivasan, S., Benziger, J., Bocarsly, A. B., *Journal of Power Sources*, 2001, 103, 1-9.
- (6) Kreuer, K. D., *Solid State Ionics* 1997, 97, 1-15.
- (7) Dulyea, L. M., Fyles, T. M., David Robertson, G., *Journal of Membrane Science*, 1987, 34, 87-108.
- (8) Koert, U., Stein, M., Harms, K., *Angewandte Chemie International Edition in English*, 1994, 33, 1180-1182.
- (9) Klug, A., *Angewandte Chemie International Edition in English*, 1983, 22, 565-582.
- (10) Percec, V., Heck, J., *Polymer Bulletin* 1991, 25, 431-438.
- (11) Percec, V., Johansson, G., Heck, J., Ungarb, G., Battyb, S. V., *Journal of the Chemical Society, Perkin Transactions 1*, 1993, 1411-1420.
- (12) Percec, V., Schlueter, D., Ungar, G., Cheng, S. Z. D., Zhang, A., *Macromolecules*, 1998, 31, 1745-1762.
- (13) Percec, V., Cho, W.-D., Ungar, G., Yeadley, D. J. P., *Journal of the American Chemical Society*, 2001, 123, 1302-1315.
- (14) Yoshio, M., Kagata, T., Hoshino, K., Mukai, T., Ohno, H., Kato, T., *Journal of the American Chemical Society*, 2006, 128, 5570-5577.
- (15) Beginn, U., Zipp, G., Möller, M., *Advanced Materials*, 2000, 12, 510-513.

Chapter 4

- (16) Ueda, S., Kagimoto, J., Ichikawa, T., Kato, T., Ohno, H., *Advanced Materials*, 2011, 23, 3071-3074.
- (17) Ronda, J.C., Reina, J.A., Giamberini, M., *Journal of Polymer Science Part A: Polymer Chemistry*, 2004, 42, 326-340.
- (18) Bhosale, S.V., Rasool, M.A., Reina, J.A., Giamberini, M., *Polymer Engineering & Science*, 2013, 53, 159-167.
- (19) Rapp, A., Schnell, I., Sebastiani, D., Brown, S. P., Percec, V., Spiess, H.W., *Journal of the American Chemical Society*, 2003, 125, 13284-13297.
- (20) Percec, V., Glodde, M., Bera, T. K., Miura, Y., Shiyankovskaya, I., Singer, K. D., Balagurusamy, V.S.K., Heiney, P.A., Schnell, I., Rapp, A., Spiess, H.W., Hudson, S.D., Duan, H., *Nature*, 2002, 417, 384-387.
- (21) Komura, M., Yoshitake, A., Komiyama, H., Iyoda, T., *Macromolecules*, 2015, 48, 672-678.
- (22) Tylkowski, B., Castelao, N., Giamberini, M., Garcia-Valls, R., Reina, J.A., Gumí, T., *Materials Science and Engineering: C*, 2012, 32, 105-111.
- (23) Rice, R.H., Mokarian-Tabari, P., King, W.P., Szoszkiewicz, R., *Langmuir*, 2012, 28, 13503-13511.
- (24) Magonov, S.N., Whangbo, M.H., *Surface Analysis with STM and AFM: Experimental and Theoretical Aspects of Image Analysis*; Wiley, 2008.

Chapter 5

Liquid Crystalline Polymeric Wires for Selective Proton Transport, Part 1: Wires Preparation

Krzysztof Artur Bogdanowicz, Griffin Anthony Rapsilber,

José Antonio Reina and Marta Giamberini

UNIVERSITAT ROVIRA I VIRGILI
LIQUID CRYSTALLINE POLYMERS FOR SMART APPLICATIONS.
Krzysztof Artur Bogdanowicz
Dipòsit Legal: T 1677-2015

Chapter 5

2.5.1. Introduction

Artificial photosynthesis interests scientists from all backgrounds, providing the possibilities to mimic nature on the premise of precise design and functionality of materials. This approach appears as a source of sustainable fuels for instance hydrogen and methanol¹. When it is combined with a fuel cell (FC), converting energy of chemical bonds into electricity², it presents practical access to power locked into solar radiation.

An essential element of artificial synthesis systems and polymer electrolyte membrane fuel cell is a proton exchange membrane that influences the performance, the selectivity and the durability of the system^{3,4}. Predominantly Nafion® was used in such systems considering various properties such as high proton conductivity and good mechanical properties⁵. However, the existence of serious drawbacks, for example water dependent transport and methanol crossover, shifts the attention towards bioinspired materials⁶.

Chen and co-workers disclosed an example of biomimetic material in which proton transport occurs without the presence of water, through supramolecular nanochannels formed by benzotriazole-based polymers. This example suggested that supramolecular organisation is crucial in obtaining efficient proton transport⁷. To achieve a highly organised structure of aromatic cores of discotic columnar liquid crystals, support with nanoconfinements were used. The strategy of using the discotic shaped molecules and the additional effect of π - π stacking of the neighbouring aromatic cores was successfully implemented to encourage the growth of a columnar mesophase inside the pores of the support⁸. A further important part is to ensure a continuous and an uniform organisation of disc-shaped molecules in the supramolecular wires as described by Hatice Duran et al.⁹.

In addition, promising materials like families of modified poly(epichlorohydrin) (PECH), polyglycidol (PG) and poly[2-(aziridin-1-yl)ethanol] (PAZE) were designed to be used as proton conducting membranes. The polymers were grafted by dendrons and exhibited columnar mesophases. Moreover, in the case of PECH and PG proton transport was proved^{10,11,12}. Šakalytė et al. reported that the new family of modified PAZE exhibited a columnar mesophase and partial crystallinity. Crystallinity of the polymers tend to be stabilised, on increasing the modification degree and it is undesirable because of the negative influence on the mechanical properties of the material, which finally results in increased brittleness. Nonetheless, a low modification degree

Chapter 5

does not ensure a proper columnar organisation. Columnar orientation is required for the formation of ion-conductive channels.

PAZE-based polymers show a similarity to the previously mentioned discotic macromolecules^{5,9} providing the possibility to control the growth of the columnar oriented mesophase inside pores and the formation of wires. Nonetheless, controlling the phase state, molecular packing and orientation of liquid crystalline polymers through nanoconfinement is a challenging task.

In this article, we describe the fabrication of side-chain liquid crystalline polymeric wires using PAZE modified with the dendron 3,4,5-tris[4-(n-dodecan-1-yloxy)benzyloxy]benzoic acid, with 40% and 72% modification degrees, respectively, and anodised aluminium oxide as a support. Wire formation, *by means of* the columnar mesophase growing inside the support channels, was first observed and controlled by thermal treatment. The procedure is fully reproducible on a larger scale and does not require complicated operations. In relation to other studies in the area of proton conductive polymers, our polymeric channels are acid free, therefore the expected transport would be *via* hopping mechanism without the need of water. Thereby, the water-free transport should reduce the problems caused by the membrane swelling induced by water absorption and the possible cross over effect, which reduces the selectivity of the membrane.

2.5.2. Materials and Methods

Materials

Inorganic and organic compounds were provided by Sigma-Aldrich and Fisher Scientifics and used as received. For all experiments, which needed water or aqueous solutions, Milli-Q water was used. Anodised Aluminium Oxide (AAO) from Whatman™ with pore sizes 0.02 μm and 0.2 μm in a disc form and a diameter of 13 mm were used as received.

Synthesis of polymer

The polymers were obtained by grafting liquid crystalline poly[2-(aziridin-1-yl)ethanol] (PAZE) with the dendron 3,4,5-tris[4-(n-dodecan-1-yloxy)benzyloxy]benzoic acid as described elsewhere¹². Their structure is reported in Figure 2.5.1.

Chapter 5

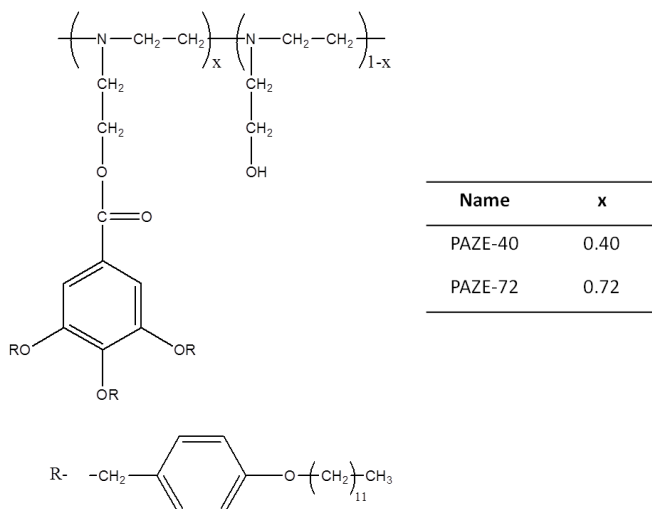


Figure 2.5.1. Structure of modified poly[2-(aziridin-1-yl)ethanol].

Characterisation Methods

Contact Angle (CA). The static contact angles with water on a membrane surface were measured with a Dataphysics OCA 15EC contact angle instrument (Filderstadt, Germany) equipped with a motorised pipette and deionised water as the probe liquid. The contact angle was measured immediately after placing the water drop (3 μ L) on the membrane surface. The measurements were repeated using different areas of the film: for each test reported, at least three drops of water were used.

X-Ray diffraction (XRD). The XRD measurements for low angle range were taken using a Bruker-AXS D8-Discover diffractometer, equipped with parallel incident beam (Göbel mirror), vertical θ - θ goniometer, XYZ motorised stage and with a GADDS (General Area Diffraction System). The samples were placed directly on the sample holder for a reflection analysis. An X-ray collimator system close-to-the-sample allows analysing areas of 500 μ m. The X-ray diffractometer was operated at 40 kV and 40 mA to generate CuK α radiation. The GADDS detector was an HI-STAR (multiwire proportional counter of 30x30 cm with a 1024x1024 pixel) placed at 30 cm from the sample. The X-ray beam hit the sample at 0.5° of incidence. The collected frame (2D XRD pattern) covers at such distance a range from 0.9° up to 9.2° of 2 θ . The diffracted X-ray beam travels through a He beam path (SAXS attachment) to reduce the air scattering at low angles. The direct X-ray beam is stopped by a

Chapter 5

beam stop placed directly on the detector face. The exposition time was of 300s per frame.

XRD measurements for wide angle range were made using a Siemens D5000 diffractometer (Bragg-Brentano parafocusing geometry and vertical θ - θ goniometer) equipped with an Anton-Paar TTK low temperature chamber. The goniometer was fitted with a curved graphite diffracted-beam monochromator, incident and diffracted -beam Soller slits, a 0.03° receiving slit and scintillation counter as a detector. The angular 2θ diffraction range was between 1 and 40° . Sample was deposited on to a low background Si(510) plate and this onto the temperature chamber sample holder. The data were collected with an angular step of 0.03° at 3s per step. $\text{CuK}\alpha$ radiation was obtained from a copper X-ray tube operated at 40 kV and 30 mA. The patterns were collected after 300s of delay time at 25°C , 55°C and 70°C for PAZE-40 and 25°C , 45°C and 60°C for PAZE-72 with the heating rate of $10^\circ\text{C}/\text{min}$ for both cases. A static air-atmosphere was used throughout the measurement.

Differential Scanning Calorimetry (DSC). Thermal transitions were detected with Mettler-Toledo Differential Scanning Calorimeter mod. 822 in dynamic mode at a heating or a cooling rate of $10^\circ\text{C}/\text{min}$ in cycle: 1st heating from -15°C to 140°C , followed by cooling to -15°C and 2nd heating to 180°C . Nitrogen was used as the purge gas. The calorimeter was calibrated with an indium standard (heat flow calibration) and an indium-lead-zinc standard (temperature calibration).

Scanning Electron Microscopy (SEM). Both internal and external morphology of hybrid membranes were analysed by Scanning Electron Microscopy SEM (JEOL JSM-6400 Scanning Microscopy Series), with an acceleration voltage of 15–20 kV. For better conductivity, the sample was covered with a carbon layer produced by a vapour deposition.

With the aim to obtain a surface-free polymeric layer a cryostat (Leica CM 1950) was employed. First of all, the membrane was attached over a specimen disc with a freezing medium. An embedding medium for frozen tissue specimens was used (Sakura Tissue). Once the membrane was fixed over the specimen disc, the disc was immersed into liquid nitrogen. Then, the specimen disc was placed in the cryochamber. After that, the sample was scraped. Finally the membrane was analysed by SEM.

Chapter 5

Polarize Optical Microscopy (POM). The clearing temperatures were roughly estimated by POM; textures of the samples were observed with an Axiolab Zeiss optical microscope equipped with a Linkam TP92 hot stage.

Water and Methanol Uptake. Weighted membranes were immersed in deionised water or methanol solutions (1M, 2M, 6M and 12M) at room temperature for 24 h to ensure the membranes were saturated. The liquid on the surface of the wet membranes was quickly removed with filter paper, and then the weights were measured. The weights of the dry membranes were obtained after the wet membranes were dried in air for four days at room temperature, till reaching constant weight. The water uptake can be calculated as follows:

$$\text{Water uptake (\%)} = \frac{(W_{\text{wet}} - W_{\text{dry}})}{W_{\text{dry}}} \cdot 100$$

where W_{wet} and W_{dry} are the weights of wet and dry membrane samples, respectively.

Raman Spectroscopy. An Renishaw Confocal Microscope (Leica DM 2500) with FT-IR (IlluminatIR II) and Smith Streamline Raman Imaging module equipped with a 785 nm diode laser was used to acquire the Raman spectra at laser power of 5%. The spectra were recorded in a range from 100 cm^{-1} to 3200 cm^{-1} .

Atomic Force Microscope (AFM). The AFM images were recorded with an Agilent 5500 Environmental Atomic Force Microscope (Agilent Technology) equipped with an extender electronics module, which enables phase imaging in the Tapping Mode. All images were recorded in tapping mode using an extra-thin cantilever tip (Hires_C19/Cr-Au, MicroMasch) having a resonance frequency of approx.60 Hz. The scan rate was typically 0.7–2 Hz. All images ($1 \times 1 \text{ }\mu\text{m}^2$ and $0.5 \times 0.5 \text{ }\mu\text{m}^2$) were measured at room temperature, in unfiltered air. The microscope was placed in an active vibration isolation chamber (Agilent Technology), which was further placed on a large, sturdy table to eliminate external vibration noise. The Nanotec WSxM 5.0 Develop 4.0 Image Browser Scanning Probe Microscopy23 was used for the roughness analysis of the images.

Chapter 5

Membrane Preparation

The hybrid membranes were prepared by impregnation of the AAO disc with a 30% (w/w) polymeric solution in tetrahydrofuran (THF) (approximated amount of solution per disc was 30 mg). Subsequently, the membrane was placed in a water bath for 10 minutes, in order to induce polymer precipitation, and dried in air overnight. The procedure was conducted on a teflon sheet to prevent of the membrane adhesion to the surface.

Thermal Treatment (baking process)

The polymer/ceramic membrane on teflon was placed on a LinKam TP92 hot stage and heated up to 90°C and kept for 10 minutes. Afterwards, it was cooled slowly at 0.5°C/minute rate to an annealing temperature: 30°C, 40°C or 50°C, keeping the temperature constant for 3 hours, 24 hours or 72 hours, respectively. Finally, the membrane was cooled to room temperature with a cooling rate of 0.5°C/minute. The same procedure was repeated on a bigger scale using a Hewlett Packard 5890 Series II Gas Chromatograph oven.

2.5.3. Results and Discussion

The objective of this study was the preparation of wires inside an inorganic support *via* growth of the homeotropically oriented columnar liquid crystalline polymer.

As previously described, a family of side-chain liquid crystalline modified poly[2-(aziridin-1-yl)ethanol] was designed to obtain a columnar structure where the polymer backbone forms a channel, which is stabilised by grafted dendrons¹². The inner part of the columns contains nitrogen atoms, where the electron-donor character is expected to carry positively charged particles across the membrane without the need of water^{10,11}. Consequently, polymers with a modification degree of 40% (PAZE-40) and 72% (PAZE-72) were chosen for this study. The thermal features of the polymers are presented in Table 2.5.1. Preliminary trials revealed a practical unfeasibility to form an intact and self-supporting membrane using the polymer alone, because of its brittleness. This fact hinders the possibility of using this material for future applications without any modification.

Chapter 5

Table 2.5.1. Calorimetric features of polyamines obtained by DSC

Polymer	Modification degree (%)	T_c (°C) ^a	Mesophase
PAZE-40	40	43	Col
PAZE-72	72	44	Col

^a - clearing temperature value obtained from second heating scan, at scan rate: 10°C/minute.

Therefore, anodised aluminium oxide (AAO) was used as a supporting material to improve the mechanical resistance. Additionally, the very well defined structure and cylindrical channels can contribute in orientation of the polymeric columns perpendicularly to the surface, which is important for ion transport across the membrane¹³. The fact the AAO is an electrical insulator, makes it a more suitable material in terms of nanotechnology applications^{14,15}. The AAO with pore size of 0.2 μm was used firstly to prepare hybrid membranes.

In an effort to confirm the polymer presence inside the untreated hybrid membranes, a Raman study was performed (see Supporting Information). The signals of AAO template (Figure S2.5.1 for AAO support) did not appear in the spectrum as a result of a low response to the irradiation: that is why all peaks were assigned as coming from the polymer. The spectra of the inner part were recorded up to 20 μm below the surface (Figure S2.5.2), for both sides. The studies at the different depths were conducted as a result of the penetration of a laser beam, reaching an acceptable noise level, which allowed observing signals coming from the polymer. The analysis confirmed the presence of polymer, both on the surface and in the internal part of membrane.

To establish the polymer distribution inside the channels for freshly precipitated membranes, SEM microscopy was employed. Figure 2.5.1A presents a micrograph of the membrane cross-section, which displays the formation of a polymeric dense layer on the impregnation side. Due to its low conductivity, all samples were covered with a carbon layer and a line microanalysis was carried out. The lines were drawn perpendicular to the support channels for the whole thickness of the cross-section. The presence of the polymer was confirmed for the open channels as maxima in the intensity of the carbon element, which in turn corresponded to the minima of the aluminium intensity; they were found to

Chapter 5

be the open channels filled with polymer and are represented as black lines in Figure 2.5.1B.

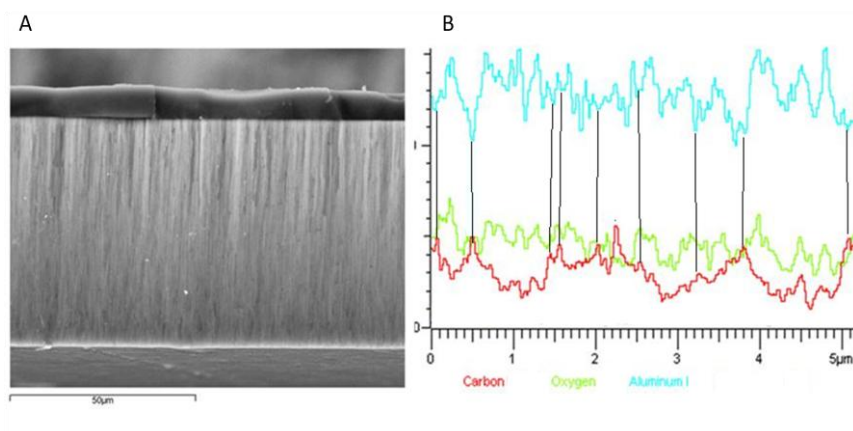


Figure 2.5.1. SEM analysis; A- the cross-section in back scattering mode of PAZE-40 over the AAO and B- line microanalysis for the same cross-section.

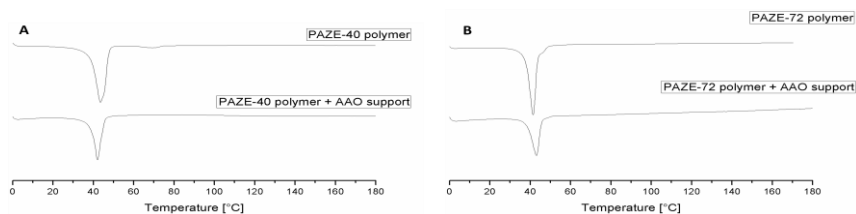


Figure 2.5.2. Thermographs of the second heating scan of PAZE-40 with and without the support in A, and PAZE-72 with HYB72-02 with and without the support in B.

The influence of the inorganic part of the hybrid membrane on the thermal properties of the polymer was explored by DSC. Figure 2.5.2 presents the thermographs of the PAZE polymers and their hybrid membranes (PAZE-40- Figure 2.5.2A, and PAZE-72- Figure 2.5.2B). For all samples only one endotherm was observed and interpreted as signal coming from the clearing of columnar mesophase, based on the XRD analysis and POM. Only a small shift of 2°C towards lower temperatures could be observed for hybrid membranes with respect to their corresponding unsupported polymers.

Chapter 5

Undoubtedly, the inorganic support does not influence significantly the thermal properties the polymer, which is observed in the DSC spectra.

To focus on the tuning of a well-defined general procedure, considering the thermal and the structural similarities of both polymers, PAZE-40 was used as a model system. The hybrid membranes (HYB40), prepared by the impregnation of a polymeric solution and the phase inversion precipitation, were analysed using XRD to establish polymer organisation. Supports with two different pore size, 0.02 μm (HYB40-002) and 0.2 μm (HYB40-02), were used. The diffractograms were found to be qualitatively similar in the case of both supports on both sides of the unbaked membranes. The low angle XRD reveals numerous signals with the intraplanar spacings at 35.8 Å, 19.2 Å, 16.5 Å, 14.0 Å and 11.2 Å, where just the first three corresponded to the indexation (hkl)= (100), (110) and (200) of hexagonal organisation. The other signals come from crystalline residue as expected for polymer with partial proclivity to crystallisation (Figure 2.5.3A)¹². Furthermore, some broad picks were detected at 2θ angles in range from 0.9° to 5.5°. They could be related to the coexistence of another type of packing, overlapped with the hexagonal, as it was noticed for the signal at $2\theta=2.47^\circ$ (d_{100}) as a left-side shoulder. The pattern suggests a possible coexistence of two lattices, from which the best defined is the columnar hexagonal, with the parameter of single unit cell (a) equal to 41.3 Å. The full data are presented in Table 2.5.2. Nonetheless, the azimuthal scan on the d_{100} shows a random orientation of columns.

Table 2.5.2. Results of XRD analysis for HYB40 supported with AAO (with pore size 0.02 μm and 0.2 μm) before and after the thermal treatment.

Name	d_{100} [Å]	d_{110} [Å]	d_{200} [Å]	a [Å]	Mesophase
HYB40-002	35.8	19.2	16.5	41.3	Col _h
HYB40-02	35.0	19.1	16.2	40.4	Col _h
HYB40-002T30	42.0	-	-	-	Col
HYB40-02T30	40.2	-	-	-	Col

To achieve a homeotropical alignment of the columns, a thermal treatment was used as reported in the experimental section. Several scientists proved the positive influence of the thermal treatment on the improvement of the homeotropical alignment of columns formed by liquid crystalline polyethers and polyglycidols^{16,11}. The orientation perpendicular to the surface was achieved by heating above the clearing temperature

Chapter 5

and slowly cooling to room temperature, which enabled the self-assembly of columns to the stablest mesophase in the expected direction^{10,11}. A temperature of 30°C was chosen to grow a columnar mesophase during a 3-hour isothermal period using support of different pore size (abbreviation T30). The XRD diffractograms, for the annealed samples, HYB40-002T30 and HYB40-02T30, demonstrate the disappearance of most signals, except the (100) reflection, which appears at lower 2-theta angles (Figure 2.5.3A), compared to the untreated sample. Clearly, as a result of the baking process, polymer organisation changed. The absence of other reflections than the (100) in the XRD pattern is not uncommon for the hexagonal columnar mesophases¹⁷; however, formation of other mesophases like lamellar columnar cannot be excluded. Furthermore, the azimuthal scan performed on the reflection (100) also shows differences amongst the treated membranes, obtained with the different pore size of the AAO. The signal in the phi scale for HYB40-02T30 was higher and narrower than for the membrane supported with smaller pores (Figure 2.5.3B and 2.5.3C, respectively).

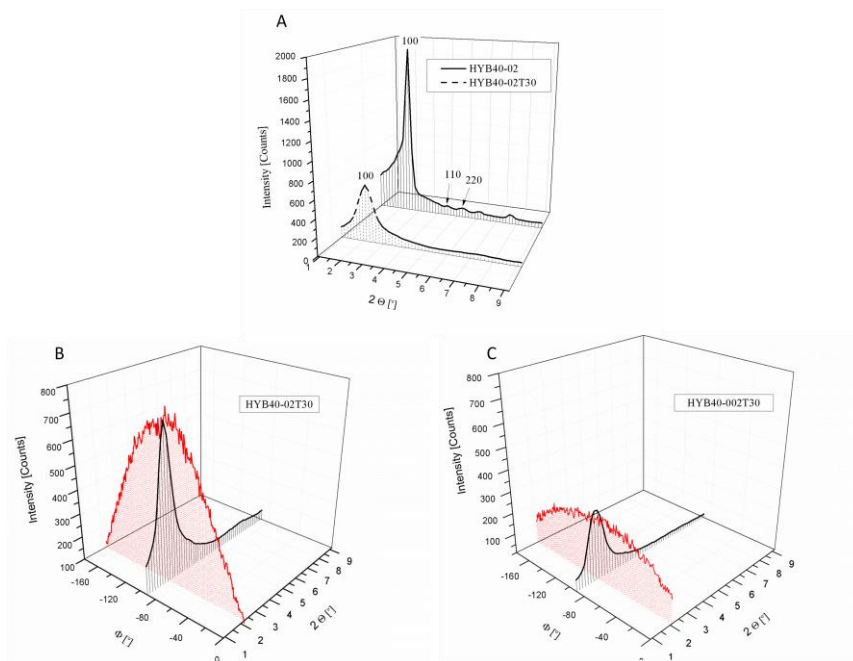


Figure 2.5.3. XRD diffractograms for samples before and after thermal treatment (A) and the comparison of the azimuthal scan, on the reflection d_{100} , of thermally treated samples HYB40-02T30 (B) and HYB40-002T30 (C).

Chapter 5

Therefore, the anodised aluminium oxide with a pore size of $0.2\mu\text{m}$ was selected for the preparation of the hybrid membranes and studied more deeply.

To optimise the conditions of the thermal treatment two other temperatures, 40°C (T40) and 50°C (T50) were evaluated with the time of the annealing, 27 hours and 72 hours, respectively. The time of the isothermal step was based on the POM observation of the polymer. It was observed that the higher the temperature of annealing, the longer time was required to grow a columnar mesophase, as expected. The samples after the different treatments were analysed by X-ray diffraction and the diffractograms are presented in Figure 2.5.4 A (HYB40-02T40) and B (HYB40-02T50). As it is shown in this figure, the increasing temperature of annealing determined an enhancement of the columnar organisation order, which can be observed in 2-theta scan as an increase of intensity and sharpening of signals. Two coexisting lattices, hexagonal and tetragonal, can be observed for HYB40-02T50 with d-spacings 42.1 \AA , 29.4 \AA and 23.8 \AA , which corresponds to Miller indices: (100), common for both lattices, (110*) for tetragonal and (110) for hexagonal. In addition, a narrowing of the signal at 90° in the azimuthal scan, was noted for $d_{100}=42.1\text{ \AA}$. This confirms the improvement in the alignment of the columns in the membrane, giving a satisfactory orientation for both sides of the hybrid membrane.

Afterwards, the annealing at 50°C was applied to a membrane containing PAZE-72 and supported with the AAO with a $0.2\mu\text{m}$ pore size (HYB72-02T50). After the treatment, the membrane shows columnar tetragonal lattice with interplanar spacing: $d_{100}=41.6\text{ \AA}$, $d_{110}=29.0\text{ \AA}$ (Figure 4C), which is similar to the XRD results of the membranes prepared with PAZE-40 after the same thermal treatment (Figure 2.5.4B). Also some signals coming from crystalline residue were observed. Although, the azimuthal scan performed on the reflection at $2\Theta=2.14^\circ$ put into evidence higher orientation, due its sharpening since the width at the half of the peak height (WHH) had a lower value (76.2° versus 127.0° found in the case of PAZE-40 and is presented in Figure 2.5.3 B and 2.5.4 C, respectively); however the peak maximum was located around 70° , which means that the columns are slightly inclined with respect to the homeotropic orientation.

Chapter 5

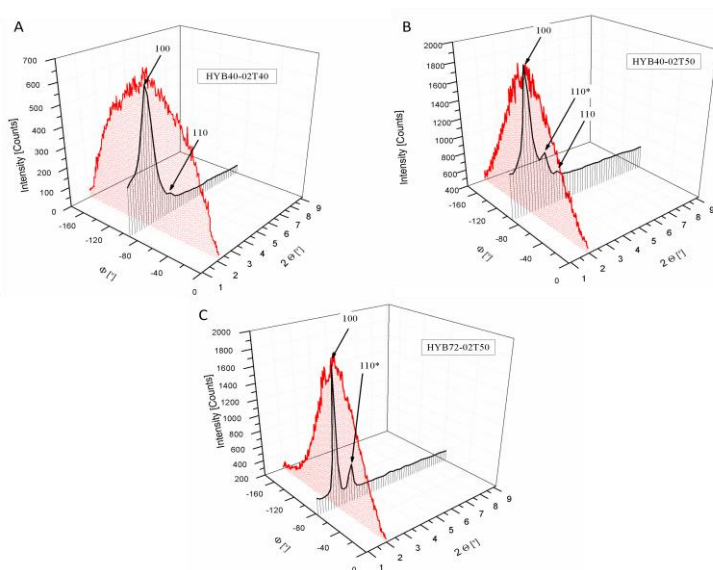


Figure 2.5.4. Comparison of 2-theta and azimuthal scan of baked samples at different temperatures of the annealing: HYB40-02 annealed at 40°C (A), and at 50°C (B) and HYB72-02 after thermal treatment at 50°C (C).

The thermal treatment was performed on a bigger scale using an oven with a controlled cooling rate, successfully obtaining reproducible results for all obtained membranes, reaching an area of 187 cm² of equal thermal exposure.

To explore a possible impact of the morphological changes on the membrane surface a CA study was conducted. An interesting relation between the orientation degree and values of the contact angle measurements was found and shows that the improvement of the columns alignment increases the hydrophobicity of the surface from 86° to 168° for hybrid membranes annealed at 30°C and 50°C, respectively. This phenomenon can be explained by the higher exposure of the hydrophobic side groups on the surface and screening of the internal polar part of the polymer. A similar tendency was observed by Bhosale et al. in the case of a family of modified polyethers and polyglycidols¹¹, where high surface hydrophobicity was associated to the homeotropical column organization in the membrane.

In furtherance to elucidate characteristics of the surface, an AFM analysis was employed for the hybrid membranes containing PAZE-40

Chapter 5

prior to and after the baking process at 50°C. The image of the untreated sample does not reveal a defined formation. The surface was smooth with some small mounds, as is presented in Figure 2.5.5A. Withal, the treated membrane showed changes on the surface by the formation of a loose structure of fibres (see Figure 2.5.5B). Several fibres appear to form clusters, which are randomly directed. The root-mean-square (RMS) analysis shows a significant change in roughness from 13.8 nm to 21.3 nm as a result of the treatment. The difference in the surface texture is caused by reorganised polymer, from random to homeotropical-like alignment and was observed in the CA measurements.

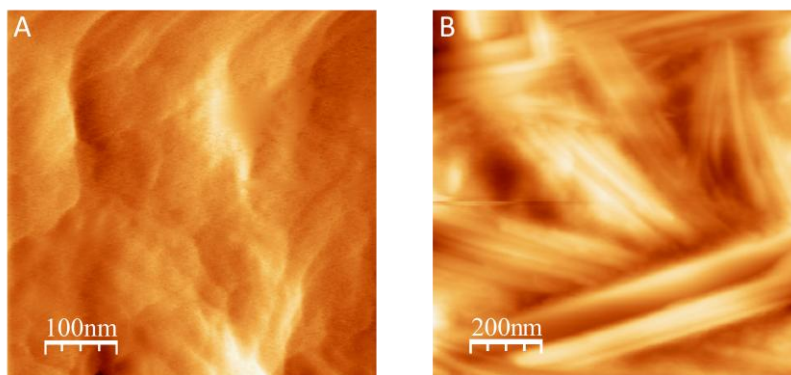


Figure 2.5.5. Topography image of PAZE-40 supported on 0.2 μm AAO prior to (A) and after annealing at 50°C (B).

The formation of wires was observed for treated membranes, containing PAZE-40 and PAZE-72, in which the dense layer was removed mechanically and is presented in Figure 2.5.6. A clearer view was obtained for the procedure performed under cryostatic conditions. Figure 2.5.6A shows a scrapped sample at room temperature and Figure 2.5.6B a sample scrapped in liquid nitrogen. The measurements of the diameter of the wires observe in Figure 6B gave a value ranging between 181 nm-250 nm for a single wire, which is in a good agreement with the size of the 0.2 μm pores of the support.

Chapter 5

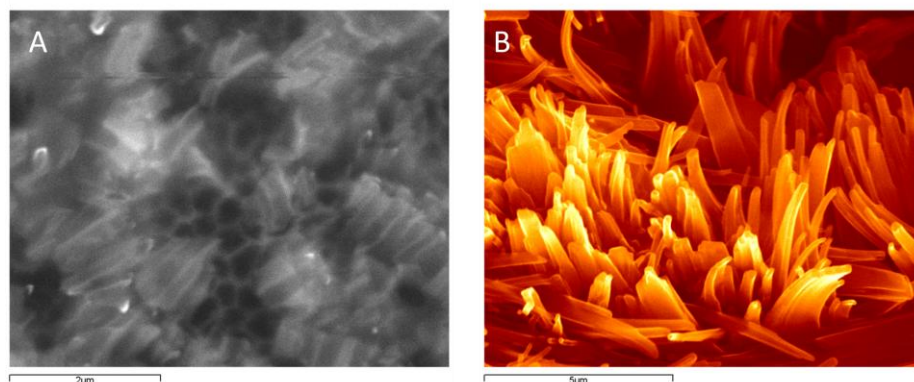


Figure 2.5.6. Images of scrapped samples: A- at room temperature and B- under cryostatic conditions.

Considering that the average size of the columns is approximately like a cell parameter, which is 42.1 \AA , a single pore of the AAO could contain roughly 225 columns forming a single wire. The formation of the continuous structure of a wire is possible by virtue of π - π stacking observed by Percec et al.¹⁸ and explained by Rapp et al.¹⁹. The stacking of aromatic units is more organized within a polymer unit, apart from the terminal groups, which have greater mobility, thus allowing the intramolecular interaction within the columns²⁰. In the AAO, the pores cover almost 40% of the surface, reducing the actual active area of the membrane, in relation to the total surface of the support. This fact implies a lower amount of polymer required to form a membrane and high mechanical stability given by the inorganic template.

To further characterize the hybrid membranes HYB40-02T50 and HYB72-02T50 an uptake test of water and methanol aqueous solutions was performed. The results for both hybrid membranes show almost identical results. Table 2.5.3 displays a general trend on the example of a membrane based on PAZE-40. The results present low water absorption and a decreasing propensity of uptake values for solutions with higher methanol content, which makes it a suitable candidate for systems for energy production using methanol as a source of hydrogen. The bibliographic values for Nafion membrane show a 21% of water uptake and reports on deformation by swelling²¹. On the contrary, the use of an inorganic structure limits the possibility of polymer protrusion within the internal structure, which stabilizes the wire structure.

Chapter 5

Table 2.5.3. Uptake values for hybrid membranes with PAZE-40 and PAZE-72 after thermal treatment at 50°C (HYB40-02T50 and HYB72-02T50, respectively).

Name	Water	1 M Methanol	2 M Methanol	6 M Methanol	12 M Methanol
HYB40-02T50	11(±3)%	10(±3)%	13(±3)%	9(±3)%	6(±3)%
HYB72-02T50	11(±3)%	11(±3)%	10(±3)%	9(±3)%	7(±3)%

2.5.4. Conclusions

We have presented the preparation of liquid crystalline wires in an inorganic support by columnar mesophase growth inside the pores, under precisely strict control of the thermal conditions. From the structural and the morphological perspective, both polymers, PAZE-40 and PAZE-72, show almost identical features and behaviour in all studied aspects. However, the use of the higher modified polymer for future application could be more suitable due to a better organization, which could result in a higher conductivity. The presence of anodised aluminium oxide does not influence the thermal properties of the polymer; moreover, it strengthened the organization of the columns in the satisfactory alignment and contributes in maintaining the dimensional firmness of the membrane. Low values of water and methanol solutions uptake unveils a great improvement over acid-based membranes. Furthermore, additional studies on ionic and methanol transport across the membrane will be fully presented in the second part of this article.

2.5.5. Acknowledgements

Financial support from Ministerio de Economía y Competitividad (CTQ2013-46825-R) is gratefully acknowledged. The authors are also grateful to Dr. Francesc Gispert for help with XRD measurements.

Chapter 5

2.5.6. Supporting Information

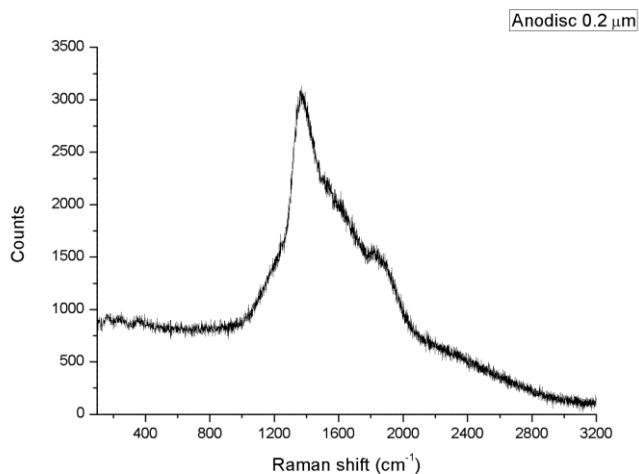


Figure S2.5.1. Raman spectrum of AAO support with 0.2 μm pores.

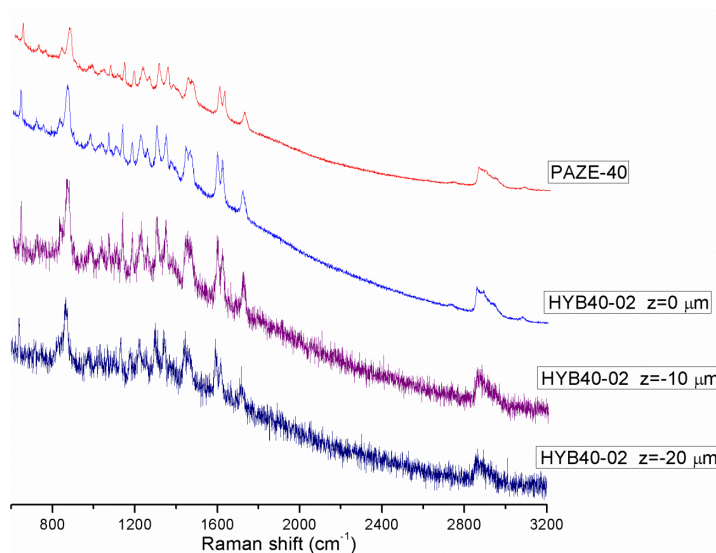


Figure S2.5.2. Comparison of Raman spectra of PAZE-40 with HYB40-02 at different depths (z).

Chapter 5

2.5.6. References

- (1) Listorti A., Durrant J., Barber J., *Nature Materials* 2009, 8, 929-930.
- (2) Buratto S.K., *Nature Nanotechnology*, 2010, 5, 176-176.
- (3) Sharma S., Ghoshal S.K., *Renewable and Sustainable Energy Reviews* 2015, 43, 1151-1158.
- (4) Peckham T.J., Holdcroft S., *Advanced Materials*, 2010, 22, 4667-4690.
- (5) Jiang S. P., Liu Z.; Tian Z.Q., *Advanced Materials* 2006, 18, 1068-1072.
- (6) Wegst U.G.K., Bai H., Saiz E., Tomsia, A.P., Ritchie, R.O., *Nature Materials*, 2015, 14, 23-36.
- (7) Chen Y., Thorn M., Christensen S., Versek, C., Poe A., Hayward R.C., Tuominen M.T., Thayumanavan S., *Nature Chemistry*, 2010, 2, 503-508.
- (8) Zhang R., Zeng X., Kim, B., Bushby, R.J., Shin K., Baker P.J., Percec V., Leowanawat P., Ungar G., *ACS Nano*, 2015, 9, 1759-1766.
- (9) Duran H., Hartmann-Azanza B., Steinhart M., Gehrig D., Laquai F., Feng, X., Müllen K., Butt H.-J., Floudas G., *ACS Nano* 2012, 6, 9359-9365.
- (10) Tylkowski B., Castelao N., Giamberini M., Garcia-Valls R., Reina J.A., Gumí T., *Materials Science and Engineering: C*, 2012, 32, 105-111.
- (11) Montané X., Bhosale S.V., Reina J.A., Giamberini M., *Polymer*, 2015, 66, 100-109.
- (12) Šakalytė A., Reina J.A., Giamberini M., *Polymer* 2013, 54, 5133-5140.
- (13) Bureekaew S., Horike S., Higuchi M., Mizuno M., Kawamura T., Tanaka D., Yanai N., Kitagawa S., *Nature Materials*, 2009, 8, 831-836.
- (14) Poinern G.E.J., Ali N., Fawcett D., *Materials*, 2011, 4, 487-526.
- (15) Lee W., Park S.-J., *Chemical Reviews*, 2014, 114, 7487-7556.

Chapter 5

- (16) Chvalun S.N., Blackwell J., Cho J.D., Kwon Y.K., Percec V., Heck J.A., *Polymer*, 1998, 39, 4515-4522.
- (17) Zennaro A., Hincapié C.A., Martos A., Sebastián R.M., Barberá J., Serrano J.L., Sierra T., *European Journal of Organic Chemistry* 2013, 2013, 5331-5340.
- (18) Percec V., Glodde M., Bera T.K., Miura Y., Shiyanovskaya I., Singer K.D., Balagurusamy V.S.K., Heiney P.A., Schnell I., Rapp A., Spiess H.W., Hudson S.D., Duan H., *Nature* 2002, 417, 384-387.
- (19) Rapp A., Schnell I., Sebastiani D., Brown S.P., Percec V., Spiess H.W., *Journal of the American Chemical Society* 2003, 125, 13284-13297.
- (20) Nakano T., *Polymer Journal*, 2010, 42, 103-123.
- (21) Zawodzinski T.A., Derouin C., Radzinski S., Sherman R.J., Smith V.T., Springer T.E., Gottesfeld S., *Membranes. Journal of The Electrochemical Society* 1993, 140, 1041-1047.

Chapter 6

Liquid Crystalline Polymeric Wires for Selective Proton Transport, Part 2: Ion Transport in Solid-state

Krzysztof Artur Bogdanowicz, José Antonio Reina, Philippe Sizat

and Marta Giamberini

UNIVERSITAT ROVIRA I VIRGILI
LIQUID CRYSTALLINE POLYMERS FOR SMART APPLICATIONS.
Krzysztof Artur Bogdanowicz
Dipòsit Legal: T 1677-2015

Chapter 6

2.6.1. Introduction

Polymeric ion exchange materials which provide a selective proton transport, play a key role in green technologies like artificial photosynthesis and fuel cells^{1,2}. The actual efficiency of proton-exchange membranes depends mainly on their ability of rapid and selective transfer of proton ion³. Two predominant methods to characterise ion transfer in ion exchange membranes can be found in the field of physics of dielectric materials and in a process called electro dialysis: electrochemical impedance and current voltage curve.

We report on a new generation of hybrid biomimetic materials arisen from a fusion between materials science, life science and nanotechnology. The combination of liquid crystalline dendronised poly[2-(aziridin-1-yl)ethanol] (PAZE), which self-assembles into columns and a well-defined anodised aluminium oxide template, results in the formation of polymeric wires. A homeotropical-like orientation of columns was achieved by applying the thermal treatment at optimum conditions. The preparation and characterisation of the material are fully described in the first part of this article.

Since the development of electrochemical impedance spectroscopy (EIS), some decades ago, the scientist reached a milestone in establishment of a tool useful for understanding the phenomenon of ion conductivity. The EIS is a deep-studied technique for diagnose and modelling that has been extensively used in electrochemical systems (for an ample range of fuel cells' features) enabling characterisation of the ion exchange membrane with high accuracy⁴. The fundamentals of this technique are based on registration of system response under applied small amplitude perturbation of current or voltage under investigation conditions. The obtained value, known as impedance (Z), describes a complex behaviour of materials, which in overall consist of real (Z') and imaginary ($-Z''$) part. The first represents the resistance, ruled by Ohm law, and the second describes the capacitance. These values can be plotted out as Nyquist plot, showing the relation between Z' versus $-Z''$, which typically forms a characteristic half circle. This graph can be used with the purpose of interpretation of system by simulating an equivalent electrical circuit; it is a physical description of system using elements like resistor and capacitors to create a model. Due to presence of a double layer capacitance of the interface electrode/membrane and a polarised resistance on the membrane surface, the value of Z' at the highest measured frequency can be used as the membrane resistance, since is the least affected by these effects. This membrane resistance is

Chapter 6

afterwards used to calculate its specific conductivity (σ) following the equation:

$$\sigma = \frac{l}{AR} \quad (1)$$

where, l is the distance between electrodes, A is the membrane area and R is the value of the Z' of the samples at the highest frequency⁴.

Another approach used to characterise the ion transport in ion-exchange membranes is to investigate current-voltage curves of membrane system in aqueous salt solution. This method comprises combining the advantages of an actual ion migration caused by the concentration polarisation phenomenon, well-known from theoretical and experimental studies^{5,6}. The concentration polarisation, exhibited by cation exchange membranes, is attributed to the fact that the cation carries the charge, while in solution both cations and anions are charge carriers. The concentration polarisation causes also an additional diffusion transport, causing presence of diffusion boundary layers at membrane surfaces. The typical current-voltage curve, consistent with principles of the concentration polarisation theory, shows a lineal increase of the electric current with increasing voltage, reaching a limiting value of current (I_{lim}). The limiting current is the necessary current required to transfer all available cations and is represented graphically as a *pseudo-plateau*. Usually, a following third region can be observed with an increasing slope and can be ascribed to several distortions⁷⁻⁹.

In the second part, we focus on ion transport of this novel material using two different approaches: electrochemical impedance spectroscopy and current-voltage measurements. The impedance values for hybrid systems were obtained for different relative humidity conditions and at increasing temperature. Besides, the transport of various alkali ions and proton ion was observed at room temperature and expressed by current-voltage curves. The results for the new generation of hybrid material were compared with the commercial membrane- Nafion 117. The PAZE-based hybrid membranes display a high proton-selectivity unreported for any other membrane to the best of our knowledge. Further, we highlight a serious issue related to the acid-free internal structure in comparison with Nafion-like materials, which must be considered in the results interpretation. Additionally, the evaluation of methanol crossover discloses a significant improvement, since it was found three orders of magnitude lower permeability than the hydrated Nafion 117.

Chapter 6

2.6.2. Materials and Methods

Materials

Inorganic and organic compounds were provided by Sigma-Aldrich and Fisher Scientifics and used as received. For all experiments, which required water or aqueous solutions, Mili-Q water was used. Anodised Aluminium Oxide (AAO) from Whatman™ with pore sizes 0.2 μm in a disc form and a diameter of 13 mm were used as received.

The Nafion 117 membrane from DuPont was provided by Fuel Cell Etc and cleaned before using¹⁰. The cleaning included boiling in 3% aqueous H_2O_2 for 30 minutes, followed by immersion in hot 5% aqueous sulphuric acid for 1-hour. After each step the membrane was placed into hot water to wash. At the end the clean membrane was placed in water.

As described in part 1, samples were named according to their modification degree, pore size of AAO support and annealing temperature. In general, they were named: HYB X-Y or HYB X-YTN, where X stands for the modification degree (%), Y for the pore size in μm and N for the annealing temperature in $^\circ\text{C}$, if any. The active area for hybrid membranes, in all analysis, is reduced to 40% of the total area, because of the possibility of forming conductive wires only inside the pores, which occupy 40% of the support surface.

Membrane preparation

The hybrid membranes were prepared as described in **Part 1** by impregnation of the AAO disc with a 30% (w/w) polymeric solution in tetrahydrofuran (THF) (estimated amount of solution per disc was 30 mg). Afterwards, the membrane was placed in a water bath for 10 minutes to induce polymer precipitation and was dried in air overnight. The procedure was conducted on a teflon sheet to prevent the membrane adhesion to the surface.

Thermal Treatment (Baking process)

The polymer/ceramic membrane on teflon was placed on a LinKam TP92 hot stage and heated up to 90°C and kept for 10 minutes. Afterwards, it was cooled at $0.5^\circ\text{C}/\text{minute}$ rate to 50°C , keeping the temperature constant 72 hours. Finally, the membrane was cooled to room temperature with a cooling rate of $0.5^\circ\text{C}/\text{minute}$.

Chapter 6

Characterisation

Methanol permeability test. The transport experiments were performed using a teflon test cell that consisted of two compartments, separated by the tested membrane, containing the feed and the stripping solutions, respectively. The feed and the stripping volumes were 200 mL and the effective membrane area was 0.86 cm². The initial feed solution was 1 M methanol aqueous solution and the stripping was mili-Q water in all cases.

The methanol content was determined by means of gas chromatography (Varian CP-3800) with FID as a detector and SUPELCOWAX™ 10 fused capillary column (30m x 0.25mm x 0.25µm). The calculations of methanol permeability were carried out in accordance with the equations:

Under steady-state conditions, methanol flux was calculated by Flick's First Law:

$$J = \frac{P\Delta C}{l} \cdot 10^{-3} \quad (2)$$

where l (cm) is the membrane thickness and ΔC is the difference in concentration (mol l⁻¹) between the initial feed solution (C_0) and the final stripping solution. In our experimental conditions, C_0 was much greater than the final stripping concentration, so we considered $\Delta C \sim C_0$.

P is the methanol permeability (cm² s⁻¹), defined as:

$$P = DS \quad (3)$$

where D is the methanol diffusion coefficient and S is the sorption equilibrium parameter.

The flux is related to the permeability coefficient p (cm s⁻¹), as:

$$J = pC_0 \quad (4)$$

$$P = pl \quad (5)$$

Chapter 6

The permeability coefficient, can be described by the following equation:

$$-\ln \frac{C_f}{C_0} = \frac{Ap}{V_f} t \quad (6)$$

where C_0 (mol l⁻¹) is the initial concentration of the feed solution and C_f (mol l⁻¹) is the feed concentration calculated from the stripping solution at time t (s):

$$C_f = C_0 - C_s \quad (7)$$

V_f is the feed volume (mL) and A is the actual membrane area (cm²).

We calculated the methanol permeability in accordance with the above equations. Data were collected up to 48 hours and fitted according to equation (6).

Impedance test. AC impedance measurements were performed using Autolab PGstat 20 in potentiostatic mode. The amplitude of 350 mV and 20 different frequencies from the range of 50 kHz and 5 Hz were selected. Current ranging was set automatically from 100 mA to 1 μ A. A hermetic brass chamber with ventilation valve consisting of through-plane set-up equipped with four 2-probe stainless steel electrodes (with area equal 0.27 cm²). In each pair of electrodes just one of them can have the possibility to move and the applied pressure depend on a force of a metal spring. The cell was closed and placed in a thermostatic bath, to collect the data in temperatures from RT to 70°C. To implement controlled humidity level the chamber was filled with 50 mL of water or a mixture of water-glycerol, which was not in contact with the electrodes. Three different relative humidity (RH) values were chosen: 98%, 75% and 50%, which required pure water, water-glycerol (20 mL-30 mL) and water-glycerol (13 mL-37 mL) respectively¹¹. The stabilisation period was 24 hours before desired RH was reached. All proton conductivities were calculated according to equation (1).

Current-voltage curve. Current-voltage (I-V) measurements were performed using Autolab PGstat100 in potentiostatic mode with current ranging (automatic) from 100 mA to 100 μ A, potential range from 0 V to 4.98 V, step 0.01 V and scan rate 0.01 V/s. The experimental set-up is presented in Figure 2.6.1. The distance between the reference electrodes (Ag/AgCl) and membrane was 0.85 cm. The solution volume in each

Chapter 6

compartment was 90 mL. The measurements were performed at the ambient temperature approx. $24.5 \pm 0.8^\circ\text{C}$.

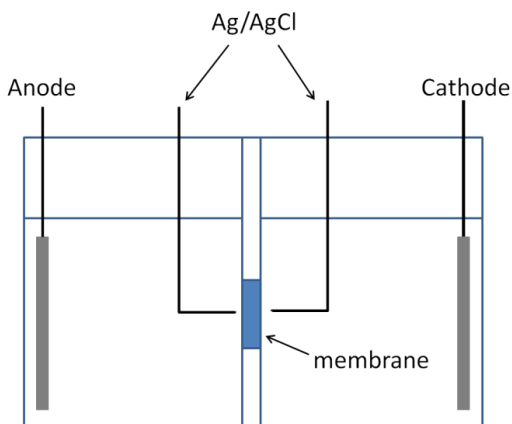


Figure 2.6.1. The experimental set-up for Current-Voltage measurements.

Samples for this measurement were placed in Parafilm M with a hole giving a total membrane area equal to 0.57cm^2 . The composite membrane was placed between two sheets of Parafilm and sealed. The values of voltage for samples were calculated by subtracting the solution resistance without the membrane. Compensation was calculated according to equation:

$$U_{\text{comp}} = U_m - R_{\text{sol}} \cdot I_m \quad (8)$$

where U is the voltage, R is the resistance, I is the current and the subscripts $_{\text{comp}}$, $_{\text{m}}$ and $_{\text{sol}}$ refer to compensated value, measured value and solution alone, respectively.

SEM. Both internal and external morphologies of hybrid membranes were analysed by Scanning Electron Microscopy SEM (JEOL JSM-6400 Scanning Microscopy Series), with an acceleration voltage of 15–20 kV. For better conductivity, the sample was covered with a carbon layer produced by vapour deposition.

Chapter 6

2.6.3. Results and Discussion

In Part 1 of this article we reported on preparation of hybrid membranes containing dendronised poly[2-(aziridin-1-yl)ethanol], modified at 40% and 72%, respectively, and Anodised Aluminium Oxide support. The membranes were prepared by impregnation of support with polymeric solution. The tendency of these polymers to self-assemble into columns, which could work as cationic channels, was used to form conductive wires across the membrane. The satisfactory homeotropical-like orientation of polymeric columns was achieved by using a thermal treatment with annealing at 50°C during 72 hours and the results were confirmed by X-ray diffraction at low 2θ angles. The polymer/ceramic system showed low water and methanol solution uptake, which suggests a great improvement in terms of water influence on the studied material.

Conductivity measured by EIS

To evaluate the conductivity of hybrid membrane, AC impedance measurements were carried out. Based on the morphological studies, the data obtained from the analysis were assigned only to the polymer since the pores of AAO are fully filled (article Part 1) and crystalline aluminium oxide structure behaves as an insulator¹². Nafion 117 membrane was used as control sample to monitor the home-made set-up and the influence of the conditions (controlled temperature and humidity changes) on the sample. The impedance data will be discussed with reference to ionic conductivity of tested materials.

In the measured conditions of humidity, Nafion 117 membrane shows a significant increase of conductivity for the highest RH (0.145 mS/cm and 0.481 mS/cm for dry and after equilibration for 24h at RH 98%, respectively); increasing temperature also improve the conductivity, reaching value of 2.02 mS/cm. This behaviour was expected and it is in a good agreement with the performance reported in the literature¹³, which confirms correct working of the system.

For all hybrid membranes, a similar behaviour was observed and an example of typical graphical representation of the results- Nyquist plot is presented in Fig. 2.6.2. In this figure the points at low Z' were obtained for the frequencies in the range between 50 kHz and 100 Hz; moreover, they form a curvature which could be a part of a full arch and because of the limited analysis range was not observed. The results of the impedance at frequencies below 100 Hz showed randomness and higher impedance values, than the values obtained at higher frequencies.

Chapter 6

In order to describe the polymer conductivity by an equivalent electric circuit, a model was simulated. A common practice is the simplicity of the model, which is as important as its adequate reflection of the real system. Hence, it is necessary to identify the main components contributing to the overall impedance of the system in order to determine an accurate representation in the form of equivalent circuit.

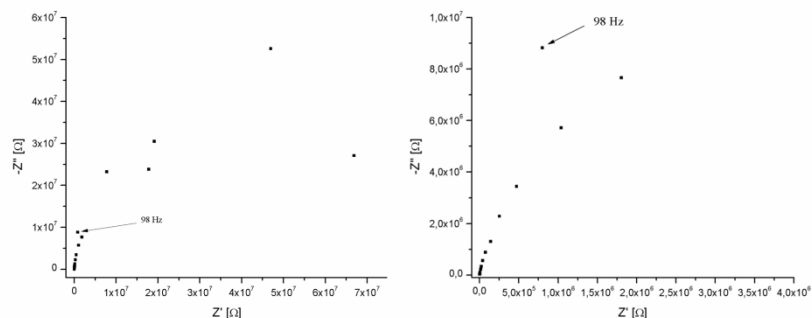


Figure 2.6.2. A Nyquist plot for composite membrane containing PAZE modified in 40%.

The Nyquist plots were successfully fitted in the equivalent circuit presented in Fig S2.6.1 (see Supporting Information section). As it is shown in the figure, the model contains three elements: resistor 1 (R_1) connected, first in parallel to constant phase element (CPE_1) and second in series to resistor 2 (R_2). For systems, where exhibit complicated frequency response, like in this case, a constant phase element was used and plays a role of imperfect capacitor. If the impedance of the CPE is expressed as $Z = 1/(i\omega CPE)^n$, the power of the CPE (n) defines its character between perfect resistor, for n equals to 0, or perfect capacitor, when n is equal to 1. For all cases, n value was found to be equal to 0.98, which shows almost perfect capacitor behaviour⁴. In studied case, CPE_1 and R_1 were assigned as the blocking interface electrode/membrane and R_2 as the bulky resistance of polymer.

To dispute conductivity properties of the tested membranes, equation (1) was applied, where the real Z' values at the highest obtained frequency were used as the resistance value.

Chapter 6

Table 2.6.1. Specific conductivity ($\times 10^{-5}$ S/cm) of composite membranes at (30 ± 1) °C at different relative humidity.

Sample	Relative humidity		
	50%	75%	98%
HYB40-02	2.9 \pm 0.2	2.2 \pm 0.7	2.2 \pm 0.1
HYB40-02T50	2.8 \pm 0.2	2.5 \pm 0.3	2,8 \pm 0.2
HYB72-02	3.2 \pm 0.2	2.7 \pm 0.3	2.2 \pm 0.1
HYB72-02T50	2.7 \pm 0.8	2.6 \pm 0.3	2.5 \pm 0.3

Table 2.6.1. contains values of proton conductivity of AAO/PAZE-based polymers, before and after thermal treatment; similar conductivity values can be observed for membranes based on PAZE-40 with and without thermal treatment. Although, the difference in conductivity was more significant for the PAZE-72 based system, which showed higher values for untreated sample. Furthermore, a similar decrease of conductivity can be noted with simultaneous increase of humidity for all data.

In addition, Figure 2.6.3 and Figure 2.6.4 represent the change of conductivity induced by increasing temperature at three RH values for HYB72-02 and HYB72-02T50, respectively. A fluctuation of values can be observed for hybrid systems based on both polymers slightly above 60°C; conductivities were found independent of relative humidity conditions. On the other hand, differently than the real part, the evolution of the imaginary part of impedance at the highest frequency was affected by temperature. In all cases, a decline of the imaginary impedance values was observed in the temperature around 60°C, which could be associated with the isotropization of the polymer. This fact put in the evidence that melted polymer could improve the contact between membrane surface and the electrodes, while the Z' values maintain relatively stable.

The impedance analysis for anodised aluminium oxide was performed only to detect possible imperfections of the hybrid systems. In case of AAO alone, the curves were showing a linear and stable behaviour with constant slope in the measured frequency range just in case of wet support (Figure S2.6.2). The impedance values at highest frequency were affected by water and showed an increase of Z' values for

Chapter 6

the wet sample comparing with the dry sample (58.8 Ω and 783.7 Ω for dry and wet sample, respectively). Besides, it was noted that the presence of water improves the contact between membrane and electrode, which results in a significant decrease of $-Z''$ values (for dry 1756.0 Ω and for wet sample 316.5 Ω). This behaviour is typical of a passive transport through the pores¹⁴.

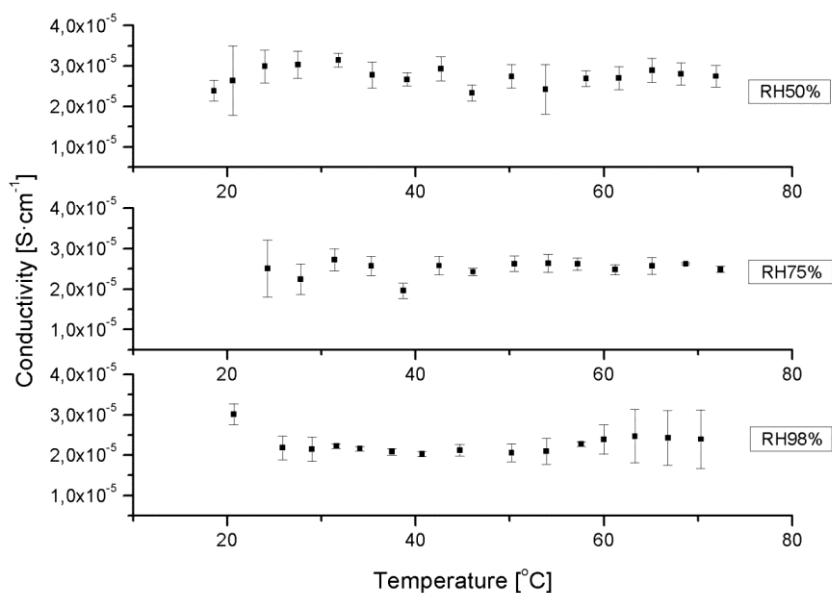


Figure 2.6.3. The conductivity values for HYB72-02 at different temperature and at three relative humidity values.

Chapter 6

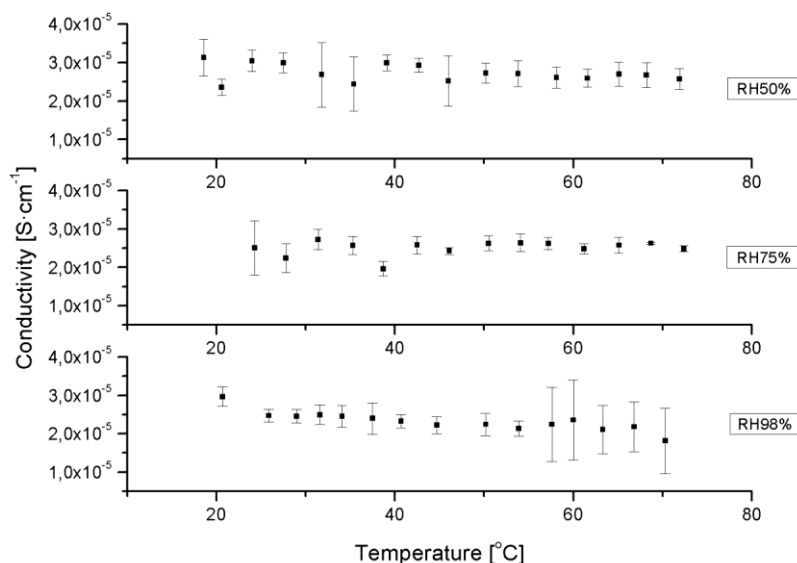


Figure 2.6.4. The conductivity values for HYB72-02T50 at different temperature and at three relative humidity values.

Studied ceramic/polymer membranes exhibit an unvarying performance, slightly influenced by temperature and relative humidity. In case of liquid crystalline polymers, it was presumed that the conductivity would change drastically above its isotropisation temperature¹⁵, which was not observed in this case. In PAZE-based hybrid system, the clearing temperature is around 45°C, above which columns disappear; it should influence the conductivity of polymeric wires formed by columns. The inconsistency from expected behaviour might be explained by the non-ionic nature of the polymers used to form the membranes. The presence of any ionic elements inside the channels, like sulphuric groups, is responsible for the ionic conductivity observed under AC current^{3,16}, because of their easy polarisability¹⁷. If one performs the impedance measurement for a channel filled with ions, for instance with sodium cations, that would give a value of the resistance, from which the specific sodium conductivity could be calculated. Consider an opposite case, where the channel is built of weakly polarised bonds and ions are not present inside, the impedance values would be significantly greater than in prior example. Thus, the resistance value could not be interpreted as

Chapter 6

coming from ion conductivity, since the channel is not occupied by ions, but as a result of weak bond polarisation of bonds in the channel. The second case can well represent the hybrid systems, where the channels are formed by polymeric backbone with weakly polarising bonds. The strategy of using dendritic mesogen in lateral position causes polymer self-assembling into ion-free columns^{18,19} without need of using cationic templates. This limits the possibility to introduce cations and their corresponding counterions in the structure^{20,21}. This specific structure and the low water uptake, makes impossible to fill the channels with ions and to gain ion conductivity values from AC impedance in the case of our hybrid membranes.

Ion transport in aqueous solution

To characterise the ion transport, current-voltage measurements were performed using a set-up described in Characterisation section in Figure 2.6.1. The current-voltage (C-V) curves obtained for the HYB40-02T50 in 0.1M HCl, show three characteristic regions: ohmic, limiting current and electroconvective, as presented in Figure 2.6.5. The value of ohmic resistance (R_{ohm}) density is equal 69 ± 19 [$\Omega \cdot \text{cm}^2$] and the limiting current (I_{lim}) density of $(3.23 \pm 0.67) \times 10^{-3}$ [$\text{A} \cdot \text{cm}^{-2}$]. Obtained values showed stability within the error range for all measured samples, preserving all described characteristics. The presence of well defined limiting current range indicated the cation permselectivity of HYB40-02T50 membranes, which signify that the cations contributes mainly in charge transfer across the membrane.

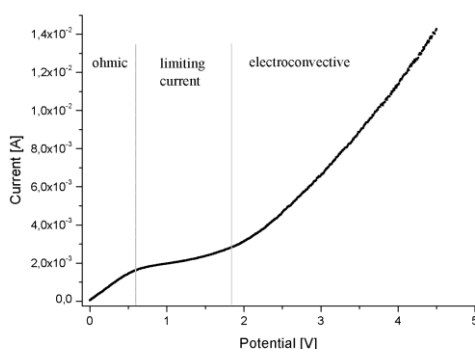


Figure 2.6.5. Hybrid membrane based on PAZE modified in 40% and thermally treated.

Chapter 6

The experiment performed for HYB72-02T50 in the 0.1M hydrochloric acid does not present a typical C-V curve like for HYB40-02T50. The limiting current region was not defined in all cases. However, the difference between ohmic and convectional regions was distinguished. The ohmic resistance density was equal $(1.2 \pm 0.5) \times 10^2 \text{ } [\Omega \cdot \text{cm}^2]$.

The measurements performed on membranes based on PAZE with both modification degrees show a significant increase of the ohmic resistance for all used alkaline ions. The measurements performed in alkali salt solutions show a big disparity of resistance values, therefore, in Table 2.6.2 we show resistance ranges for each ion. For comparison of the results, the most unfavourable and the lowest resistance values obtained for each of the ions have been selected to represent the most objective conditions. To express the selectivity of the membranes, a ratio of admittance (reverse resistance) of alkali ion value over proton ion ($Y_{\text{ion}}/Y_{\text{H}^+}$) was calculated for each membrane (Table 2.6.3). A direct comparison of admittance between Nafion and the hybrid membranes cannot be done because of difference in the diffusion boundary layer for both systems and different membrane thickness.

Table 2.6.2. Ohmic resistance range obtained from C-V curves for different cations.

Sample name	$R_{\text{ohm}} \times 10^{-3} [\Omega \cdot \text{cm}^2]$			
	HCl	LiCl	NaCl	KCl
Nafion	0.003	0.006	0.019	0.012
HYB40-02	0.404 - 5.070	14.651 - 15.200	0.594 - 176.521	1.670 - 93.364
HYB40-02T50	0.069 \pm 0.019*	0.378 - 4.184	1.127 - 7.346	2.446 - 35.764
HYB72-02	0.171 - 11.018	9.340 - 76.966	4.907 - 15.578	0.497 - 93.873
HYB72-02T50	0.12 \pm 0.05*	7.015 - 222.573	2.461 - 18.117	1.265 - 162.826

* resistance values for which error was possible to establish

Chapter 6

Table 2.6.3. Selectivity ($Y_{\text{ion}}/Y_{\text{H}^+}$ ratio) values for alkaline cations.

Sample name	$Y_{\text{ion}}/Y_{\text{H}^+} \times 100$ [%]		
	Li^+	Na^+	K^+
Nafion	47.3	14.2	22.8
HYB40-02	2.8	68.0	24.2
HYB40-02T50	18.2	6.1	2.8
HYB72-02	1.8	3.5	34.4
HYB72-02T50	1.7	4.8	9.3

From the $Y_{\text{ion}}/Y_{\text{H}^+}$ ratio, it can be concluded that, except for HYB40-02, all hybrid membranes show an improvement in proton selectivity compared with Nafion 117. Within the ceramic/polymer system, the best performance was disclosed by the samples after thermal treatment in comparison with its untreated analogue; HYB40-02T50 shows the stablest performance and high proton selectivity. For HYB72-02T50 shows almost proton specific transport with lightly higher resistance but without a well-defined limiting region.

The ion transport across a membrane in case of hybrid system is affected by several factors related to the surface and to the morphology of membranes and influence ion diffusion at the membrane surface and its mobility inside the membrane. For better understanding of this new generation of hybrid biomimetic materials, analogies to other well-established systems will be done, highlighting similarities and differences between them.

PAZE polymers grafted with dendritic groups, were designed to self-assemble into columnar structures like those described by Percec et al.^{18,19,22}. For better visualisation Figure 2.6.6 present a schematic process of self-assembly into columns, which form polymeric wires.

Chapter 6

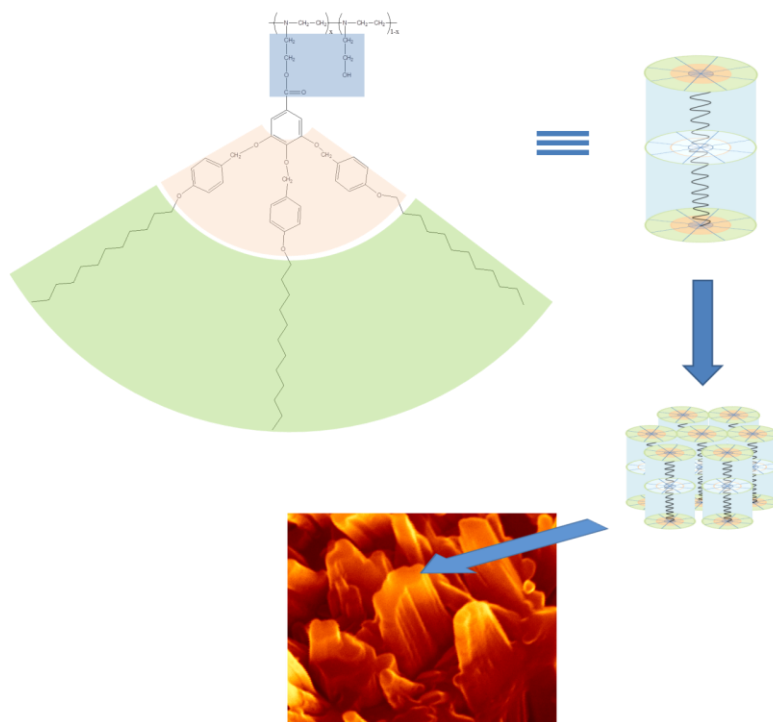


Figure 2.6.6. Schematic illustration of polymer organisation. We show the self-assembly of PAZE- modified polymer into columns and columns aggregation, which are the building blocks for polymeric wires.

The internal cavity of the columns is expected to be formed by polymer backbone with nitrogen atoms, as electron-donor sides, separated by ethylene units. Armand et al.²¹ described the ion motion for lithium salts in a complex with poly(ethylene oxide) (PEO); PEO might be considered as linear version of crown ethers. The ions migration, both cation and anion, was possible because of the metal ions coordination and solvation-desolvation along the polymer chain. However, this requires polymer mobility, which can be achieved at temperatures above the glass transition, where polymer can be considered as a solvent. A similar study was performed on different liquid crystalline polymer with metal salt showing similar behaviour to PEO^{23,24}. Differently from PEO-based systems, the hybrid membranes channels are not filled with ions, which limits the possibilities to record cation transport across the membranes to a system, where charge misbalance occurs. The charge misbalance obtained in C-V measurements conditions allows registration of cations

Chapter 6

migration through the hybrid membranes. Satisfactory homeotropical-like alignment of the columns was obtained by thermal treatment and consequently showed lower resistance values for proton-ion. The higher resistance within an ample range for alkali ions could be explained by irregular channel size; the polymeric backbone is grafted randomly by tapered mesogens, which could act on channel resulting in formation of narrower and wider segments. Likewise, the unequal thickness of polymer, forming dense layer, would entail longer time of penetration affecting all cations, having greater impact on bigger species.

Methanol Crossover

The permeation of methanol was measured and took place over concentration gradient as a driving force at atmospheric pressure. The HYB40-02T50 showed almost two magnitudes lower methanol crossover than the Nafion 117 membrane at the same conditions: methanol permeability values equal to $3.49 \times 10^{-8} \text{ cm}^2 \text{ s}^{-1}$ and $2.56 \times 10^{-6} \text{ cm}^2 \text{ s}^{-1}$, respectively.

Due to the unusual structure of the polymeric channels, the membrane cannot be compared with typical acid-based PEMs. Considering the morphology of the channels present in our hybrid systems, the methanol could pass across the membrane *by* both inner hydrophilic as well as the boundary hydrophilic/hydrophobic part of the columns (column scheme presented in Figure 2.6.6). Methanol uptake from 1M solution gave 6% in the case of PAZE, while a remarkably higher value, that is 30%, was obtained in the case of AAO. Hybrid membranes, on the other hand, gave 9% methanol uptake: therefore, one can guess that the presence of PAZE considerably limits the interaction of methanol with the support material.

2.6.4. Conclusion

Ion transport for novel hybrid membranes based on modified poly[2-(aziridin-1-yl)ethanol] supported on anodised aluminium oxide were studied. The results for hybrid materials put in to evidence that the electrochemical impedance give lower values of proton conductivity in case of materials with non-ionomeric structure. Whence, the current-voltage experiments were used for ion transport characterisation; the results obtained for two different modification degrees disclosed lower proton conductivity and high selectivity to hydrogen ion compared with Nafion 117. It was proved that the homeotropical alignment of polymeric columns increased the transport across the membrane. Moreover, the

Chapter 6

material turned to be less affected by methanol crossover, giving value two orders of magnitude lower than commercial Nafion 117. Interesting results of hybrid systems could indicate the potential use for practical application where selective ion transport is high priority, like artificial photosynthesis.

2.6.5. Acknowledgement

Financial support from Ministerio de Economía y Competitividad (CTQ2013-46825-R) is gratefully acknowledged.

2.6.6. Supporting Information

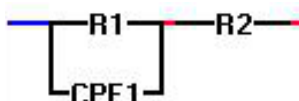


Figure S2.6.1. An equivalent circuit model used to fit experimental data.

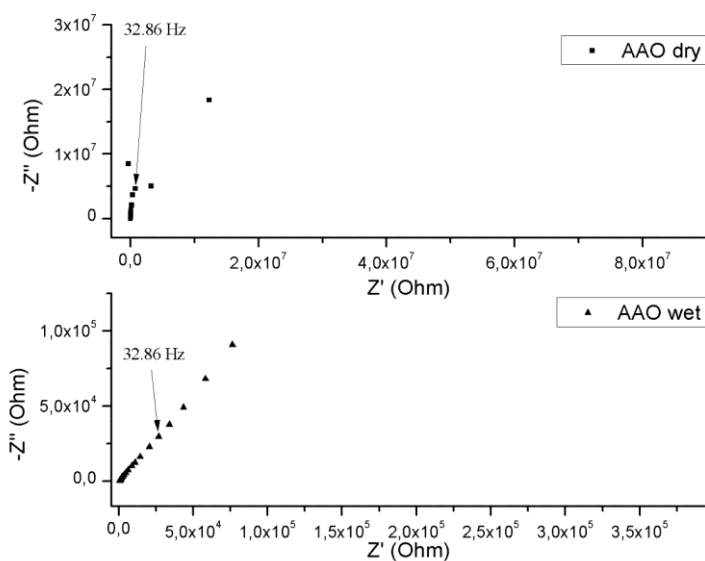


Figure S2.6.2. The Nyquist plot for dry (top) and wet (bottom) AAO support.

Chapter 6

2.6.7. References

- (1) Bureekaew S., Horike S, Higuchi M., Mizuno M., Kawamura T., Tanaka D., Yanai N. & Kitagawa S., *Nature Materials* 2009, 8, 831 - 836.
- (2) Sharma S., Ghoshal S.K., *Renewable and Sustainable Energy Reviews* 2015, 43, 1151-1158.
- (3) Peckham T.J., Holdcroft S., *Advanced Materials*, 2010, 22, 4667–4690.
- (4) Niy S.M.R., Hoorfar M., *Journal of Power Sources*, 2013, 240, 281-293.
- (5) Aguilera V.M., Mafe S., Manzanares J.A., Pellicer J., *Journal of Membrane Science*, 1991, 61, 177-190.
- (6) Choi J.-H., Park J.-S., Moon S.-H., *Journal of Colloid and Interface Science*, 2002, 251, 311–317.
- (7) Chamoulaud G., Bélanger D., *Journal of Colloid and Interface Science*, 2005, 281, 179-187.
- (8) Choi J.-H., Lee H.-J., Moon S.-H., *Journal of Colloid and Interface Science*, 2001, 238, 188–195.
- (9) Pawlowski S., Sístat P., Crespo J.G., Velizarov S., *Journal of Membrane Science*, 2014, 471, 72–83.
- (10) Zawodzinski Jr T.A., Neeman M., Sillerud L.O., Gottesfeld S., *Journal of Physical Chemistry*, 1991, 95, 6040-6044.
- (11) Forney C.F., Brandl D.G., *HortTechnology*, 1992, 2, 52-54.
- (12) Poinern G.E.J., Ali N., Fawcett D., *Materials* 2011, 4, 487-526.
- (13) Sone Y., Ekdunge P., Simonsson D., *Journal of The Electrochemical Society*, 1996; 143, 1254-1259.
- (14) Ruiz-Hitzky E., Aranda P., Casal B., Galván J.C., *Advanced Materials*, 1995, 7, 180-184.
- (15) Tan S., Wu Y., Liang T., Yang X., *International Journal of Hydrogen Energy*, 2014, 39, 17391-17397.

Chapter 6

- (16) Argun A.A., Ashcraft J.N., Hammond P.T., *Advanced Materials*, 2008, 20, 1539–1543.
- (17) Mark J.E. ed., *Physical Properties of Polymers Handbook*, Springer, 2006.
- (18) Percec V., Glodde M., Bera T.K., Miura Y., Shiyanovskaya I., Singer K.D., Balagurusamy V.S.K., Heiney P.A., Schnell I., Rapp A., Spiess H.W., Hudson S.D., Duan H., *Nature* 2002, 417, 384-387.
- (19) Percec V., Schlueter D., Ungar G., Cheng S.Z.D., Zhang A., *Macromolecules*, 1998, 31, 1745-1762.
- (20) Barteau K.P., Wolffs M., Lynd N.A., Fredrickson G.H., Kramer E.J., Hawker C.J., *Macromolecules*, 2013, 46, 8988-8994.
- (21) Armand M., *Advanced Materials*, 1990, 2, 278-286.
- (22) Rapp A., Schnell I., Sebastiani D., Brown S. P., Percec V., Spiess H.W., *Journal of the American Chemical Society*, 2003, 125, 13284-13297.
- (23) Imrie C.T., Ingram M.D., McHattie G.S., *Advanced Materials*, 1999, 932-834.
- (24) Dias F.B., Batty S.V., Gupta A., Ungar G., Voss J.P., Wright P.V., *Electrochimica Acta*, 1998, 43, 1217-1224.

General Conclusions

UNIVERSITAT ROVIRA I VIRGILI
LIQUID CRYSTALLINE POLYMERS FOR SMART APPLICATIONS.
Krzysztof Artur Bogdanowicz
Dipòsit Legal: T 1677-2015

General Conclusions

- ❖ We synthesized and characterized three nematic liquid crystalline polyesters, containing α -methylstilbene moieties in the main chains and aliphatic or aromatic spacers and evaluated two synthetic strategies to obtain higher yield and higher molecular weight of the polymer.
- ❖ The kinetic studies of photoisomerisation process in solution for all α -methylstilbene-based polyesters were performed using ^1H NMR and different time of UV irradiation and it was found to be of first order, with constants of the order of 10^{-4} s^{-1} .
- ❖ The Z to E photoisomerization at 180°C for polymeric membrane containing α -methylstilbene derivatives was first time reported after irradiating the sample at 254 nm and the process was monitored as liquid-crystalline texture changes under POM microscope.
- ❖ The photosensible microcapsules, containing different core materials, based on poly(α -methylstilbenesebacate-co- α -methylstilbeneisophthalate) successfully formed single shell using semicontinuous nozzle device.
- ❖ The release experiment showed stability of microcapsules in the absence of light and release of vanillin under irradiation at 365 nm, reaching plateau after 20 minutes.
- ❖ The release from microcapsules was proved both theoretically and experimentally, being a result of polymer main chain contraction caused by E to Z isomerisation of α -methylstilbene moiety.
- ❖ Homeotropical orientation of modified poly(epichlorohydrine) and poly(epichlorohydrine-co-ethylene oxide) was induced by baking process and was confirmed by XRD analysis at small 2Θ angles.

General Conclusions

- ❖ The homeotropical alignment of the ion conducting columns in the membrane resulted in remarkable proton conductivity, in the range of 10^{-2} to 10^{-3} S/cm, independently from the relative humidity.
- ❖ A successful columnar mesophase growth of dendronized poly[2-(aziridin-1-yl)ethanol] inside the AAO support was obtained by precisely strict control of the thermal conditions.
- ❖ Polymeric wires formation of modified polyamine was revealed in SEM micrographs and the AAO could contains roughly 225 columns.
- ❖ The electrochemical impedance was proved to give unreliable proton conductivity values for hybrid materials based on polyamines in comparison to current-voltage curve.
- ❖ The hybrid systems exhibited selective proton transport, in comparison to other monovalent cations, and the methanol cross-over disclosed values two order of magnitude lower then Nafion 117 membrane.

Appendixes

UNIVERSITAT ROVIRA I VIRGILI
LIQUID CRYSTALLINE POLYMERS FOR SMART APPLICATIONS.
Krzysztof Artur Bogdanowicz
Dipòsit Legal: T 1677-2015

Appendixes

Appendix A. List of Figures, Tables and Schemes

Figure 1. Schematic representation of the molecular arrangement in A-the crystal, liquid crystal and isotropic liquid; B- nematic, smectic and columnar mesophase.

Figure 2. Schematic representation of helically twisted molecular layers among the director axes (n) in cholesteric mesophase.

Figure 3. Exemplary packing of disc-like molecules in columnar mesophases: columnar hexagonal (Col_h), columnar tetragonal (Col_{tet}), columnar oblique (Col_{ob}) and columnar rectangular (Col_r).

Figure 4. Schematic representation of rod-like and disc-like molecules.

Figure 5. Examples of different calamatic molecules.

Figure 6. Disc-like molecules with different discotic cores.

Figure 7. A schematic representation of the MC-LCPc and SC-LCPs.

Figure 1.1. Schematic representation of capsules structure: single core is surrounded by continuous one shell (left); multiple cores are suspended in wall matrix (middle); and single core coated by two different wall materials (right).

Figure 1.2. Photoisomerization of stilbene.

Figure 1.1.1. 1H NMR spectra in $CDCl_3$ of P2 before (top) and after (bottom) irradiation for 20 min. The insets show magnifications of vinyl (6.3–6.9 ppm) and methylic (2.10–2.30 ppm) proton regions.

Figure 1.1.2. ^{13}C NMR spectrum in $CDCl_3$ of P2 before photoirradiation.

Figure 1.1.3. 1H NMR spectrum in $CDCl_3$ of P4. The insets show magnifications of vinyl (6.7–6.9 ppm) and methylic (2.15–2.40 ppm) proton regions.

Figure 1.1.4. POM micrographs: (a) P1, 182 °C, on cooling from the isotropic phase; (b) P2, 185 °C, first heating; (c) P3, 161 °C, second heating; (d) P4, 194 °C, first heating. Heating or cooling rates: 10 °C min^{-1} .

Figure 1.1.5. Normalized FTIR spectra at room temperature of P2 powder (a) before and (b) after heating for 15 min at 200 °C.

Figure 1.1.6. POM micrographs of P4 film at 180 °C: (a) before photoirradiation; (b) after 10 min photoirradiation at 364 nm; (c) after 20min photoirradiation at 364 nm; (d) after 20 min photoirradiation at 364 nm followed by 10 min photoirradiation at 254 nm.

Figure 1.1.7. UV absorption spectra of P2 in chloroform (a) before and (b) after 45 min UV irradiation at 364 nm.

Figure 1.1.8. ESEM micrographs of (a) the surface and (b) cross-section of P2 membrane.

Figure 1.1.9. Static contact angles with water for a P2 membrane: (a) before irradiation; (b) after UV irradiation at 365 nm. The contact angle

Appendixes

decreases, revealing that the membrane is more hydrophilic after irradiation.

Figure S1.1.1. ^1H NMR spectrum in CDCl_3 of P1.

Figure S1.1.2. ^{13}C NMR spectrum in CDCl_3 of P1.

Figure S1.1.3 ^1H NMR spectrum in CDCl_3 of α -methylstilbene. The insets show a magnification of vinyl (6.45- 6.75 ppm) and methylic (2.17-2.24 ppm) protons regions.

Figure S1.1.4. ^1H NMR spectrum in CDCl_3 of P3.

Figure S1.1.5. ^{13}C NMR spectrum in CDCl_3 of P3.

Figure S1.1.6. ^{13}C NMR spectrum in CDCl_3 of P4.

Figure S1.1.7. DSC thermograms of: (a) P3, second heating scan; (b) P4, first heating scan; (c) P2, first heating scan; (d) P1, second heating scan. Scan rate: $10^\circ\text{C}/\text{min}$.

Figure S1.1.8. XRD pattern of: (a) P2, 30°C ; (b) P2, 180°C ; (c) P4, 30°C .

Figure S1.1.9. Thermogravimetric analysis in nitrogen of: (a) P3; (b) P4; (c) P2; (d) P1.

Figure 1.2.1. Structure of poly(α -methylstilbenesebacate-co- α -methylstilbeneisophthalate).

Figure 1.2.2. Schematic diagram of the atomization setup.

Figure 1.2.3. ESEM micrographs of the (a) surface and (b) cross-section of the P4 membrane.

Figure 1.2.4. AFM images of P4 membrane (a) before and (b) after 30 min of irradiation with UV light at 365 nm.

Figure 1.2.5. Model of the structural change of the P4 film, containing α -methylstilbene moieties in the main chain, induced by photoisomerization.

Figure 1.2.6. Wettability changes of the P4 membrane (a) before irradiation, (b) after UV irradiation at 365 nm, and (c) after UV irradiation at 365 nm followed by additional irradiation at 245 nm.

Figure 1.2.7. ESEM micrographs of (a) microcapsules containing chloroform as a filler, (b) a single microcapsule after cryogenically cutting, and (c) details of the fractured cross section.

Figure 1.2.8. ESEM micrographs of (a) microcapsules containing vanillin in chloroform as filler, (b) a single microcapsule, and (c) detail of the fractured cross section after cryogenically cutting.

Figure 1.2.9. Vanillin release from P4 microcapsules in water at 20°C , in the time range of 0–35 min, in the absence (■) and presence (◆) of continuous irradiation with UV light at 365 nm.

Figure 1.2.10. ESEM micrographs of a single microcapsule containing chloroform/vanillin after 30 min of release experiments at room temperature (a) without UV light and (b) accompanied by UV irradiation at 365 nm.

Appendixes

Figure S1.2.1. Characteristic size distribution, as measured on 245 microcapsules, of P4 capsules containing chloroform as a core.

Figure S1.2.2. Characteristic size distribution, as measured on 167 microcapsules, of P4 capsules containing vanillin as a core.

Figure 1.3.1. Structure of poly[(α -methylstilbenesebacate)-co-(α -methylstilbeneisophthalate)].

Figure 1.3.2. Optimized structures of cis- and trans-pddp with important structural parameters such as C=C bond length and ring plane offset.

Figure 1.3.3. Frontier molecular orbitals of trans-4,4'-(prop-1-ene-1,2-diyl)diphenol.

Figure 1.3.4. Unit cell (top) and extended polymer (bottom) of trans-C2.

Figure 1.3.5. Unit cell (top) and extended polymer (bottom) of cis-C2.

Figure 1.3.6. Frontier crystal orbitals (Γ point) of trans-C2.

Figure 1.3.7. Molecular models adapted from the optimized polymers: cis-M (top) and trans-M (bottom) with C C bond lengths (\AA).

Figure 1.3.8. Experimental and simulated UV-visible spectra (nm). A Gaussian broadening was used in the theoretical transition peaks.

Figure S1.3.1. ESEM micrographs of a) single microcapsule containing vanillin in chloroform as a filler after preparation, b) after 30 minutes of release experiment at room temperature without UV light and c) accompanied by UV irradiation at 365 nm.

Figure S1.3.2. Unit cells of trans-C8 (top) and cis-C8 (bottom).

Figure 2.1. Diagram presenting hydrogen fuel cell (A) and artificial photosynthesis (B).

Figure 2.2. The chemical structures of sulfonated polymers: a) Nafion®, b) Aquivion® and c) SPEEK.

Figure 2.3. Schematic illustration of phosphorus acid doped imidazolium polymers.

Figure 2.4. Schematic illustration of ion transport inside a Nafion channel¹⁴.

Figure 2.5. Schematic illustration of self-assembling process of liquid crystals into columns with different packing.

Figure 2.4.1. The structure of two polymeric families based on poly(epichlorohydrin-co-ethylene oxide), and poly(epichlorohydrin).

Figure 2.4.2. XRD analysis- Debye ring pattern (left side) and Phi diffractogram from azimuthal scan on the reflection at $2\theta = 2.2^\circ$ or 2.1° (right side), of HP1 polymer membrane prepared by immerse precipitation (A), vapour precipitation method (B) and membrane after baking process on a teflon sheet (C).

Figure 2.4.3. AFM phase image pattern of oriented membranes of HP1 prepared on teflon: A) air side B) teflon side, and corresponding topographic image patterns C) air side D) teflon side.

Appendixes

Figure 2.4.4. AFM phase image pattern of oriented CP1 membrane (A) and corresponding topographic image pattern (B).

Figure 2.4.5. Structural analysis of a HP2 membrane after permeability with Li^+ . Top: the AFM surface topography image with indication of hills diameter; bottom: TEM image before (left) and after (right) staining with RuO_4 .

Figure S2.4.1. Oriented membrane of approximately 2 cm diameter obtained by phase inversion precipitation followed by baking process.

Figure S2.4.2. XRD diffraction pattern of intensity vs 2θ : A- oriented HP1 membrane, B- oriented CP1 membrane.

Figure S2.4.3. AFM phase image pattern of surface morphology of HP1 membranes: a) unoriented b) shear oriented, and topographic image pattern of surface morphology of HP1 membranes: c) unoriented d) shear oriented.

Figure S2.4.4 XRD diffraction pattern of intensity vs 2θ fo HP2 after lithium permeability test.

Figure 2.5.1. Structure of modified poly[2-(aziridin-1-yl)ethanol].

Figure 2.5.1. SEM analysis; A- the cross-section in back scattering mode of PAZE-40 over the AAO and B- line microanalysis for the same cross-section.

Figure 2.5.2. Thermographs of the second heating scan of PAZE-40 with and without the support in A, and PAZE-72 with HYB72-02 with and without the support in B.

Figure 2.5.3. XRD diffractograms for samples before and after thermal treatment (A) and the comparison of the azimuthal scan, on the reflection d_{100} , of thermally treated samples HYB40-02T30 (B) and HYB40-002T30 (C).

Figure 2.5.4. Comparison of 2-theta and azimuthal scan of baked samples at different temperatures of the annealing: HYB40-02 annealed at 40°C (A), and at 50°C (B) and HYB72-02 after thermal treatment at 50°C (C).

Figure 2.5.5. Topography image of PAZE-40 supported on $0.2\ \mu\text{m}$ AAO prior to (A) and after annealing at 50°C (B).

Figure 2.5.6. Images of scrapped samples: A- at room temperature and B- under cryostatic conditions.

Figure S2.5.1. Raman spectrum of AAO support with $0.2\ \mu\text{m}$ pores.

Figure S2.5.2. Comparison of Raman spectra of PAZE-40 with HYB40-02 at different depths (z).

Figure 2.6.1. The experimental set-up for Current-Voltage measurements.

Figure 2.6.2. A Nyquist plot for composite membrane containing PAZE modified in 40%.

Appendixes

Figure 2.6.3. The conductivity values for HYB72-02 at different temperature and at three relative humidity values.

Figure 2.6.4. The conductivity values for HYB72-02T50 at different temperature and at three relative humidity values.

Figure 2.6.5. Hybrid membrane based on PAZE modified in 40% and thermally treated.

Figure 2.6.6. Schematic illustration of polymer organization. We show the self assembly of PAZE- modified polymer into columns and columns aggregation, which are the building blocks for polymeric wires.

Figure S2.6.1. An equivalent circuit model used to fit experimental data.

Figure S2.6.2. The Nyquist plot for dry (top) and wet (bottom) AAO support.

Table 1.1.1. Characteristics of the obtained polymers and copolymers

Table 1.1.2. NMR assignments for polymer P2

Table 1.1.3. NMR assignments for polymer P3

Table 1.1.4. NMR assignments for polymer P4

Table 1.1.5. Calorimetric features of polymers from first heating scan

Table 1.1.6. Results of TGA of polymers

Table 1.1.7. Kinetic data for E–Z photoisomerization in CDCl_3 of polymers at 20 °C.

Table 1.2.1. Values of Standardized Roughness Parameters for P4 Membrane from AFM Analysis

Table 1.3.1. Electronic, structural and energetic properties of molecular and periodic models

Table 1.3.2. Main excitations from each precursor isomer with assignments to respective molecular orbital transition

Table S1.3.1. Selected mean structural parameters of the cis- and trans-stilbene isomers

Table 2.4.1. Clearing temperatures for HP and CP polymers

Table 2.4.2. Calculated peak width at half height (WHH) and angle of orientation of membranes prepared by baking process out of different polymers on treated glass or teflon supports.

Table 2.4.3. Water contact angles of untreated and thermally treated HP1 and CP2 polymers

Table 2.4.4. Proton permeability of HP2 oriented membranes when different cations solutions are forming the stripping phase.

Table 2.4.5. Proton conductivity versus temperature and relative humidity for samples HP1, HP2, CP1 and CP2

Table 2.5.1. Calorimetric features of polyamines obtained by DSC

Table 2.5.2. Results of XRD analysis for HYB40 supported with AAO (with pore size 0.02 μm and 0.2 μm) before and after the thermal treatment.

Appendixes

Table 2.5.3. Uptake values for hybrid membranes with PAZE-40 and PAZE-72 after thermal treatment at 50°C (HYB40-02T50 and HYB72-02T50, respectively).

Table 2.6.1. Specific conductivity ($\times 10^{-5}$ S/cm) of composite membranes at $(30 \pm 1)^\circ\text{C}$ at different relative humidity.

Table 2.6.2. Ohmic resistance range obtained from C-V curves for different cations.

Table 2.6.3. Selectivity ($Y_{\text{ion}}/Y_{\text{H}^+}$ ratio) values for alkaline cations.

Scheme 1.1.1. Synthesis route to polymers and copolymers (THF, tetrahydrofuran; pyr, pyridine; DMAP, 4-dimethylaminopyridine; RT, room temperature; 1,2-DCE, 1,2-dichloroethane).

Appendixes

Appendix B. List of Publications

Directly related with the thesis:

Authors: K. A. Bogdanowicz, B. Tylkowski, M. Giamberini

Title: Preparation and Characterization of Light-Sensitive Microcapsules based on a Liquid Crystalline Polyester

Journal: Langmuir

Volume: 29

Pages: 1601-1608

Year: 2013

Authors: B. Tylkowski, K. A. Bogdanowicz, V. Ambrogi, A. Lederer, V. Patroniak, M. Giamberini

Title: Synthesis and characterization of a new family of photoactive liquid crystalline polyesters based on α -methylstilbene

Journal: Polymer International

Volume: 63

Pages: 315-326

Year: 2014

Authors: N. A. G. Bandeira, B. Tylkowski, K. A. Bogdanowicz, M. Giamberini, C. Bo

Title: An atomistic insight into light-sensitive polymers with methylstilbene building blocks

Journal: Polymer International

Volume: 64

Pages: 935-941

Year: 2015

Authors: S. V. Bhosale, K. A. Bogdanowicz, Y. Li, I. Vankelecom, R. Garcia-Valls, J. A. Reina, M. Giamberini

Title: Applying nature's genius to discotic liquid-crystal polymers for proton conducting membrane

Journal:

In preparation

Authors: K. A. Bogdanowicz, G. A. Rapsilber, J. A. Reina, M. Giamberini

Title: Liquid Crystalline Polymeric Wires for selective proton transport, part 1: wires preparation

Journal:

In preparation

Authors: K. A. Bogdanowicz, J. A. Reina, P. Sístat, M. Giamberini

Title: Liquid Crystalline Polymeric Wires for selective proton transport, part 2: ion transport in solid state

Journal:

In preparation

Appendixes

Appendix C. Congress and Contributions

Congresses

Authors: K. A. Bogdanowicz, J. A. Reina, P. Sístat, M. Giamberini
Title: Selectivity of ion transport in a hybrid membrane
Congress: 1st French-Spanish Joint Congress for Young Researchers in Polymers (JIP-JEPO 2015)
Format (poster or oral): Oral
Dates: 14-18 September 2015 **Place:** Donostia, Spain

Authors: K. A. Bogdanowicz, M. Giamberini, J. A. Reina, P. Sístat
Title: Fresh view on proton conductive membranes: novel ceramic/polymer hybrid
Congress: European Polymer Federation Congress 2015
Format (poster or oral): Oral
Dates: 21-26 June 2015 **Place:** Dresden, Germany

Authors: R. Teruel-Juanes, K.A. Bogdanowicz, J.D. Badia, V. Sáenz de Juano-Arbona, J.A. Reina, M. Giamberini, A. Ribes-Greus
Title: Estudio del espectro de relajaciones dieléctricas y la conductividad en cristales líquidos poliméricos columnares
Congress: 9^o Congreso Nacional de Ingeniería Termodinámica
Format (poster or oral): poster
Dates: 3-5 June 2015 **Place:** Cartagena, Spain

Authors: K.A. Bogdanowicz, B. Tylkowski, M. Giamberini
Title: New photosensitive microcapsules based on liquid-crystalline polyester
Congress: Third International Symposium: New Frontiers in Polymer Science
Format (poster or oral): Poster
Dates: 21-23 May 2013 **Place:** Sitges, Spain

Authors: K. Bogdanowicz, M. Wałęsa-Chorab, M. Kubicki, V. Patroniak
Title: Nowe kompleksy metali przejściowych z $(N_3O)_2$ -donorowym ligandem estrowym [The new complexes of transition metals and $(N_3O)_2$ -donor ester ligand]
Congress: 54th PTChem and SIPTChem Meeting
Format (poster or oral): poster
Dates: 18-22 September 2011 **Place:** Lublin, Poland

Appendixes

Chapter in a book

Authors: B. Tylkowski, N. A.G. Bandeira, K. A. Bogdanowicz, M. Giamberini

Chapter title: Smart microcapsules based on photo-isomerizable moieties

Book title: Microencapsulation. Innovative Applications

Editorial: M. Giamberini, S. Fernandez Prieto, B. Tylkowski

Publisher: Walter de Gruyter GmbH

Year: 2015

ISBN 978-3-11-033187-5

Stay Abroad

Organization: Institut Européen des Membranes

Department: Interface, Physicochimie, Polymères (IP2)

City: Montpellier

Country: France

Length: 3 month **Year:** 2014

Krzysztof Artur Bogdanowicz is a polymer researcher with an interest in “smart application”. He obtained his BSc degree in Chemistry from Adam Mickiewicz University in Poland with specialization in chemical analysis and synthesis. He conducted his BSc project in the field of supramolecular chemistry, centred on complexes of metals with organic ligands. He subsequently pursued a MSc in collaboration with Meteor group from Universitat Rovira i Virgili. His MSc dissertation was focused on photoactive polymeric systems.